

Fakulteit Ingenieurswese, Bou-omgewing & IT
Faculty of Engineering, Built Environment & IT

School of Engineering

Department of Materials Science and Metallurgical Engineering

NIN 890: Dissertation

Dissertation subject:

**Corrosion characterisation of solid and lattice AlSi10Mg
manufactured by laser powder bed fusion**

By
C. Taute 11200597

Submitted in partial fulfilment of the requirements for the degree MEng Metallurgical Engineering in the Faculty of Engineering.

Supervisors: Dr Hein Möller, Prof. Anton du Plessis
Date of Submission: 30 July 2021



**UNIVERSITEIT VAN PRETORIA
UNIVERSITY OF PRETORIA
YUNIBESITHI YA PRETORIA**

Denkleiers • Leading Minds • Dikgopolo tša Dihlalefi

ACKNOWLEDGEMENTS

First and foremost, a huge thank you to my parents, Barend and Estelle Taute. Without their love and support I would never have made it this far.

The Collaborative Program for Additive Manufacturing (CPAM), funded by the South African Department of Science and Innovation, is acknowledged for their financial support. The Light Metals Development Network (LMDN) is acknowledged for their additional funding.

Sincere thanks to my supervisors, Dr Hein Möller and Prof. Anton du Plessis, for their guidance and advice throughout this project.

My heartfelt appreciation to the University of Pretoria staff, namely Dr Robert Cromarty, Mr Sibusiso Mahlalela, Mr Dirk Odendaal, Mr Mfesane Tshazi, Mr Carel Coetzee, Prof. Johan de Villiers, Mrs Wiebke Grote, Mrs Erna van Wilpe, Mr Coenraad Snyman and Mrs Charity Maepa, for all their assistance during the project with experiments and advice. And to Mrs Gabi Ngema for her assistance with the admin.

I also thank the Stellenbosch University Research group 3DInnovation staff (Ms Carlyn Wells and Ms Muofhe Tshibalanganda) for their contribution to the success of this project and RMIT University, Melbourne, Australia (Prof. Martin Leary and staff) for providing all of the samples.

Special thanks to Mr Dewald Noeth and Ms Colleen Syrett at Wirsam Scientific for the use of their Olympus DSX 510 microscope, and to Alan Scrooby of Scrooby's Laboratory Services for all the corrosion tests.

Declaration on plagiarism

UNIVERSITY OF PRETORIA

Faculty of Engineering, the Built Environment and Information Technology Department of Materials Science and Metallurgical Engineering

The University places great emphasis upon integrity and ethical conduct in the preparation of all written work submitted for academic evaluation.

While academic staff teach you about systems of referring and how to avoid plagiarism, you too have a responsibility in this regard. If you are at any stage uncertain as to what is required, you should speak to your lecturer before any written work is submitted.

You are guilty of plagiarism if you copy something from a book, article or website without acknowledging the source and pass it off as your own. In effect you are stealing something that belongs to someone else. This is not only the case when you copy work word-by-word (verbatim), but also when you submit someone else's work in a slightly altered form (paraphrase) or use a line of argument without acknowledging it. You are not allowed to use another student's past written work. You are also not allowed to let anybody copy your work with the intention of passing it off as his/her work.

Students who commit plagiarism will lose all credits obtained in the plagiarised work. The matter may also be referred to the Disciplinary Committee (Students) for a ruling. Plagiarism is regarded as a serious contravention of the University's rules and can lead to expulsion from the University.

The declaration which follows must be appended to all written work submitted for Dissertation NIN 890. No written work will be accepted unless the declaration has been completed and attached.

I (full names) Carlien Taute

Student number 11200597

Topic of work NIN 890: Dissertation

Declaration

1. I understand what plagiarism is and am aware of the University's policy in this regard.
2. I declare that this report is my own original work. Where other people's work has been used (from a printed source, internet or any other source), this has been properly acknowledged and referenced in accordance with departmental requirements.
3. I have not used another student's past written work to hand in as my own.
4. I have not allowed, and will not allow, anyone to copy my work with the intention of passing it off as his or her own work.

Signature 

ETHICS STATEMENT

The author declares that she has observed the ethical standards required in terms of the University of Pretoria's Code of ethics for researchers and the Policy guidelines for responsible research.

SYNOPSIS

Additive manufacturing can be used to produce complex, custom geometries, consolidating different parts into one. This reduces the required number of assemblies and allows distributed manufacturing with short lead times. Defects, such as porosity and surface roughness, associated with parts manufactured by laser powder bed fusion, can severely limit industrial application. The effect these defects have on corrosion and hence long term structural integrity must also be taken into consideration. This project aimed to characterise porosity in both solid and lattice cube samples produced by laser powder bed fusion, with the differences in porosity induced by changes in the process parameters, and subsequently, characterising the effect porosity has on corrosion. The alloy used in this investigation is AlSi10Mg, which is widely used in the aerospace and automotive industries. Samples were studied before and after corrosion using X-Ray computed tomography (CT scanning), metallographic examination and scanning electron microscopy (SEM), as well as compression testing for the lattice cubes. It was found that higher laser power leads to more porosity and lower surface roughness. CT scanning was a very effective method to study corrosion using aligned CT images of before-after states. Porosity did not have an effect on the corrosion during the early corrosion stages (168 hours). The manufacturing process parameters induced differences in porosity and surface conditions, but did not strongly affect corrosion. It is probable that crack initiation sites such as internal porosity and defects are filled with corrosion product, delaying the onset of cracking and failure, and the corrosion product that fill the voids adding to the full strength of the lattice will also slightly increase the compressive strength of the samples.

Keywords: metal additive manufacturing, laser powder bed fusion, corrosion, AlSi10Mg, porosity, X-Ray tomography

Table of Contents

CHAPTER I: INTRODUCTION	14
CHAPTER II: BACKGROUND	15
1. Additive Manufacturing (AM)	15
1.1 Laser Powder Bed Fusion (L-PBF).....	15
1.2 L-PBF parameters	15
2. The porosity of L-PBF parts	17
3. The alloy AlSi10Mg	19
3.1 Microstructure.....	19
3.2 Characterisation of L-PBF parts	21
3.3 Alloy properties.....	24
3.4 Influence of Alloying Elements and heat treatment	27
4. Micro- and NanoCT scanning.....	29
5 Density methods and measurements.....	31
5.1 Archimedes method.....	31
5.2 Gas pycnometry	32
5.3 CT scanning	33
6. Corrosion testing.....	33
6.1 Salt spray testing	33
7. Surface roughness	34
8. Al-alloy corrosion.....	36
8.1 Surface roughness effect on corrosion	39
8.2 Porosity effect on corrosion	40
8.3 Corrosion product.....	40
8.4 Review studies on Al corrosion	44
9. Lattice structures.....	45
9.1 Types of lattices	46
9.2 Design considerations	47
CHAPTER III: MATERIALS & METHODS.....	51
1. Materials	51
2. Dimensions and Mass.....	55

3.	Density measurements	55
3.1	Archimedes	56
3.2	Gas pycnometry	56
3.3	CT-based method.....	57
4.	Surface roughness	57
5.	Metallographical examination.....	58
6.	Porosity	61
6.1	NanoCT scan porosity measurement	61
7.	Compression testing	61
8.	Salt spray	62
8.1	Neutral salt spray (NSS).....	62
8.2	Acetic acid salt spray (AASS).....	63
9.	After corrosion exposure	63
9.1	CT scanning	63
9.2	Corrosion product analysis	63
9.3	Compression testing.....	63
CHAPTER IV: RESULTS & DISCUSSION		64
1.	Dimensions and mass.....	64
1.1	Solid cubes.....	64
1.2	Lattice cubes	65
2.	Density measurements	66
2.1	Solid cubes.....	66
2.2	Lattice cubes	68
3.	Surface roughness (Solid cubes)	70
4.	Metallographic examination	72
5.	Porosity measurements	76
5.1	NanoCT scan porosity measurement	76
5.1.1	Solid cubes	76
5.1.2	Lattice cubes.....	80
6.	Compression testing (Lattice structures)	83
7.	Salt spray	84

7.1	Neutral salt spray (NSS).....	84
7.2	Acetic acid salt spray (AASS).....	85
8.	After corrosion exposure	86
8.1	CT scanning	86
8.1.1	Solid cubes	86
8.1.2	Lattice cubes.....	93
8.2	Corrosion product analysis	95
8.3	Compression testing.....	97
	CHAPTER V: CONCLUSIONS.....	99
1.	Recommendations	99
	BIBLIOGRAPHY.....	100
	APPENDIX	109

List of Figures

Figure 1: Process controlling parameters [4]	16
Figure 2: Illustration of the four main process parameters in L-PBF [11]	16
Figure 3: Examples of possible defects (left) spherical pores, (centre) unmelted powder and (right) keyhole pore [13]	17
Figure 4: A typical trend of part porosity with changes in scan speed and energy density (at constant power) [16].....	18
Figure 5: Microstructure of (a) the as-built L-PBF AlSi10Mg with (b) high magnification SEM image revealing Si segregated on the boundaries of α -Al [19]	20
Figure 6: (a) Isometric view of L-PBF cube showing 3 views, microstructure of as-built (b) XY-plane and (c) XZ-plane (Adapted from [20])	21
Figure 7: Microstructure with three distinguishing zones outlined. (Adapted from [23])	22
Figure 8: Microstructural evolution of L-PBF AlSi10Mg with (a-c) as-built condition, (d-f) solution heat treatment and (g-i) solution treatment and artificial aging [23].....	23
Figure 9: Microstructural evolution schematic during solution treating and artificial ageing [23].....	24
Figure 10: SEM images of (a) AlSi10Mg and (b) Ti-6Al-4V powder [46] with 50 μm scale bar and (c) AlSi10Mg [47] and (d) Ti-6Al-4V powder [48] with 100 μm scale bar	28
Figure 11: CT scan analysis showing cube porosity for different samples with (a) high porosity and (b) contour porosity [52]	30
Figure 12: CT scan analysis showing cube porosity for different samples with (a) subsurface porosity and (b) almost no porosity [52].....	31
Figure 13: Gas pycnometry principle [56]	32
Figure 14: Cross sections after 72 h in acetic acid salt spray [66]	34
Figure 15: CT scan analysis showing surface roughness measurements for four different cubes, with the CT-derived areal roughness S_a values superimposed on the corresponding images [52]	35
Figure 16: Schematic of the S_a measurement principle (left) [75] and (right) [72].....	36
Figure 17: Pitting of metal in NaCl solution (Adapted from [79])	37
Figure 18: Types of corrosion (Adapted from [82])	38
Figure 19: Anodic and cathodic reactions on single metal (Adapted from [87])	39
Figure 20: Cross-sectional views of pitting attack with (a) unpolished and (b) polished specimens after immersion test for L-PBF AlSi10Mg corroded in a 3.5% NaCl immersion for 30 days [86]	40
Figure 21: E-pH diagram for pure Al at 25 °C in aqueous solution [90]	42

Figure 22: E-pH diagram with corrosion mode based on experimental data for AA5086 in 0.5M NaCl environment [90]	43
Figure 23: Different types of unit cells for lattice designs using (a) strut -based design and (b) minimal surface design [95].....	46
Figure 24: Corresponding repeated lattice structures for (a) strut-based design and (b) minimal surface design [95].....	47
Figure 25: (a) Bend <i>B</i> or Stretch <i>S</i> dominated classification and (b) examples [95] .	48
Figure 26: Effective stress-strain plots from compression of a square honeycomb, indicating effective modulus, failure stress, densification strain and energy density [95]	49
Figure 27: Particle size distribution chart [98]	51
Figure 28: AlSi10Mg solid cube samples, with E1 as the lowest laser power and E5 as the highest laser power [99].....	52
Figure 29: AlSi10Mg lattice cube samples, with E1 to E5 from left to right [99]	53
Figure 30: Plans for the solid cube samples for Neutral Salt Spray (NSS) and Acetic Acid Salt Spray (AASS)	54
Figure 31: Plans for the lattice cube samples for Neutral Salt Spray (NSS) and Acetic Acid Salt Spray (AASS)	55
Figure 32: Archimedes setup sketch (Scale from [100])	56
Figure 33: Gas pycnometer and calibration standards [99].....	57
Figure 34: Olympus DSX 510 with close-up of sample under eyepiece [99]	58
Figure 35: Cross-sectioning of the solid cube [99]	58
Figure 36: (a) Zeiss AXIO Imager light optical microscope and (b) Nikon Eclipse ME600 light optical microscope [99]	59
Figure 37: (a) Zeiss 540 Ultra Plus FEGSEM and (b) JEOL JSM IT300LV [99]	60
Figure 38: Vickers Macrohardness tester [102]	60
Figure 39: Salt spray fog chamber with samples placed [99].....	62
Figure 40: Z-direction measurement variations, indicated by coloured lines	64
Figure 41: Graphs for (top) dimensions and (bottom) mass versus laser power (Solid cubes).....	65
Figure 42: Graphs for (top) dimensions and (bottom) mass versus laser power (Lattice cubes).....	66
Figure 43: Density calculated with three different methods, as a function of laser power, with error bars.....	67
Figure 44: Air bubbles on solid cube surface when submerged, encircled	68
Figure 45: Density calculated with the three different methods, as a function of laser power.....	69
Figure 46: Air bubbles on lattice cube surface when submerged, encircled	69

Figure 47: Close-up sections of the top surface of each representative sample for each of the five laser power settings, with S_a values as inserts.....	70
Figure 48: Plot of top surface roughness, S_a , as a function of laser power, with error bars.....	71
Figure 49: Colour scale maps of samples from each of the laser powers with (a) 3D view and (b) side view, of the top surface.....	71
Figure 50: Plot of side surface roughness, S_a , as a function of laser power, with error bars.....	72
Figure 51: Sectioning and mounted samples to show the three exposed planes that were examined	73
Figure 52: Microstructures of all five laser power samples	74
Figure 53: Vickers Hardness versus laser power, with error bars	75
Figure 54: Representative CT cross-sectional images for each of the five different laser power settings showing porosity (black dots) and also indicating the presence of some dense inclusions (white dots encircled in red). Arrow indicates build direction	76
Figure 55: Optical micrograph of (a) lack-of-fusion pores at low laser power (E1) and (b) spherical pores at high laser power (E5) (Encircled), solid cubes	77
Figure 56: Porosity analyses, for a 4x4x4 mm ³ region of interest, of representative samples for each of the five laser power settings, from (top) low power to (bottom) high power, with actual porosity value of ROI as insert, and overall average of whole cube (10x10x10mm ³) in brackets, solid samples.....	79
Figure 57: NanoCT slice images of the lattice structure for each laser power, with zoomed in slices below each overview image	80
Figure 58: Optical micrographs of spherical pores at (a) low laser power (E1) and (b) high laser power (E4) (Encircled).....	81
Figure 59: Porosity analyses of the lattice samples for each laser power.....	82
Figure 60: Compression test in action	83
Figure 61: Compressive strength vs laser power, before corrosion exposure, lattice structures.....	83
Figure 62: Compressive stress-strain curve for the five samples before corrosion exposure, lattice structures.....	84
Figure 63: NSS after (a) 72 hours and (b) 168 hours.....	85
Figure 64: AASS for (top) after 120 hours and (bottom) after 168 hours	86
Figure 65: Sample from the lowest laser power (E1), with corrosion overlap in blue, and corrosion product in red, with 3D image inset after 168 hours AASS	87
Figure 66: A 2D cross section from the E1 sample at “Corrosion indicator 1” site after 168 hours AASS	87
Figure 67: A 2D cross section from the E1 sample at “Corrosion indicator 2” site after 168 hours AASS	88

Figure 68: Comparison cross-section for E1 with (a) before and (b) after AASS corrosion (outlined) (AASS for 168 hours).....	88
Figure 69: Corrosion slice image of sample from second lowest laser power (E2), with 3D image inset (AASS for 168 hours).....	89
Figure 70: Comparison cross-section for E2 with (a) before and (b) after AASS corrosion (outlined) (AASS for 168 hours).....	89
Figure 71: Corrosion slice image of sample from middle laser power (E3), with 3D image inset (AASS for 168 hours).....	90
Figure 72: Comparison cross-section for E3 with (a) before and (b) after AASS corrosion (outlined) (AASS for 168 hours).....	90
Figure 73: Corrosion slice image of sample from second highest laser power (E4) (AASS for 168 hours).....	91
Figure 74: Comparison cross-section for E4 with (a) before and (b) after AASS corrosion (outlined) (AASS for 168 hours).....	91
Figure 75: Another comparison cross-section for E4 with (a) before and (b) after AASS corrosion (outlined) (AASS for 168 hours).....	92
Figure 76: Corrosion slice image of sample from highest laser power (E5) (AASS for 168 hours).....	92
Figure 77: Comparison cross-section for E5 with (a) before and (b) after AASS corrosion (outlined) (AASS for 168 hours).....	93
Figure 78: Another comparison cross-section for E5 with (a) before and (b) after AASS corrosion (outlined) (AASS for 168 hours).....	93
Figure 79: NanoCT slice image comparison before and after corrosion exposure for E1 (AASS for 168 hours).....	94
Figure 80: NanoCT slice image comparison before and after corrosion exposure for E5 (AASS for 168 hours).....	94
Figure 81: Corrosion product that formed on a top surface after 168 hours in AASS test.....	95
Figure 82: Corrosion product that formed on a side surface after 168 hours in AASS test.....	95
Figure 83: Dried corrosion product that formed on a side surface after 168 hours in AASS test.....	96
Figure 84: Raw XRD data.....	97
Figure 85: Finalised XRD data.....	97
Figure 86: Compressive yield strength versus laser power, before and after corrosion, with data labels, lattice structures.....	98

List of Tables

Table 1: Ranges for typical L-PBF processing and design parameters [1].....	17
Table 2: Chemical composition range of AlSi10Mg in AM and Casting.....	19

Table 3:	Mechanical properties of L-PBF AlSi10Mg as-built and in T6 condition [19]	24
Table 4:	Mechanical properties of L-PBF AlSi10Mg after stress-relieving heat treatment [29–31]	25
Table 5:	Mechanical properties comparison between die-cast A360 and L-PBF AlSi10Mg for as-produced state	25
Table 6:	Mechanical properties comparison between cast A360 and L-PBF AlSi10Mg for T6 condition	26
Table 7:	Mechanical properties comparison between AlSi10Mg produced by L-PBF and by casting for as made and T6 [37]	26
Table 8:	Thermal properties of L-PBF AlSi10Mg [32,33]	27
Table 9:	Corrosion tests and detection techniques (Adapted from [94])	45
Table 10:	Composition of the AlSi10Mg powder before L-PBF [98]	51
Table 11:	Parameters used in this L-PBF process	51
Table 12:	Compression test criteria	61
Table 13:	Salt spray parameters	62
Table 14:	NSS experimental plan	63
Table 15:	Density of samples of each laser power set, according to three measurement methods (Solid cubes)	67
Table 16:	Density of samples of each laser power set, according to three measurement methods (Lattice cubes)	68
Table 17:	Porosity percentage of each power set and plotted as a function of laser power (graph inset), solid cubes	77
Table 18:	Porosity versus laser power, graph insert with error bars (lattices)	80

CHAPTER I: INTRODUCTION

Aluminium alloys have a large range of applications where lightweighting is desirable. Traditionally, aluminium alloys, such as AlSi10Mg, are manufactured using casting processes that yield parts with well-known and extensively characterised properties. Today, an alternative method is available, namely additive manufacturing (AM). This process can produce similar and even more complex parts compared to casting, but the properties of these parts are not yet as widely characterised.

By using additive manufacturing, complex geometries like lattice structures can be produced and parts can be consolidated which in turn reduces the required number of assemblies [1]. AM terminology follows the ISO/ASTM 52900:2015 (E) standard, where powder bed fusion is described as a process that uses thermal energy to selectively fuse powder bed regions [2]. This process can use an electron beam or a focused laser beam. This project used laser powder bed fusion (L-PBF). L-PBF uses a laser to melt a metallic powder according to a design specified on a digital model. This is done in consecutive layers, until the component is completed [1].

The L-PBF process has sharp thermal cycles (high temperature gradients) caused by rapid and repeated melting and solidification. This, along with solid-state transformations as well as directional heat transfer, create a few challenges during production [3]. Among these challenges are residual stresses, which causes distortion and poses a cracking risk, an increased surface roughness compared to cast alloys, difficulty in obtaining fully dense parts, and a need for post processing [4]. The high temperature gradients can also make the as-built parts susceptible to solidification defects such as inhomogeneities in the microstructure, porosity and inclusions, as well as micro-cracks that form during solidification [5].

The alloy used in this project is AlSi10Mg, which is mainly used in the automotive and aerospace industries, as well as in electronics cooling [6–8]. The effects of defects on corrosion properties is still being investigated and the question remains regarding to what extent defects, such as porosity, will affect corrosion progression. In order to answer this question, this project analysed the corrosion of AlSi10Mg L-PBF solid and lattice structures, both with different porosity contents and surface conditions induced by varying one of the manufacturing process parameters. The non-destructive characterisation of the solid cubes was described in the article in the APPENDIX. This article is in its final proof stage and has been accepted for publication.

HYPOTHESIS

AM of solid and lattice AlSi10Mg cubes, using L-PBF, will display different corrosion effects for different microstructures, porosity contents and surface roughness conditions, which are obtained by varying one of the L-PBF process parameters. The process-induced porosity will play a crucial role in the corrosion progress that will be specifically relevant to complex designs with thin walls, such as lattice structures. Higher corrosion resistance is expected for finer microstructures, smaller amounts of porosity and smoother surfaces. Analyses of these corrosion effects will enable optimisation of the process parameters for desired outcomes in AM, L-PBF.

In order to explore this hypothesis, this dissertation provides background theory in Chapter II, the materials and methods used in Chapter III, results and discussion of results in Chapter IV and conclusions in Chapter V.

CHAPTER II: BACKGROUND

1. Additive Manufacturing (AM)

Additive manufacturing (AM) techniques can be divided into seven process categories, of which one is PBF, which was used in this project. [2]. With PBF, the heat source is most often either an electron beam (EB) or a laser (L). PBF can produce a near net-shaped part after printing, without needing additional steps such as casting, machining or sintering. However, it will still require post-processing such as heat treatment, baseplate and support removal, leftover powder removal and surface treatment such as polishing, depending on the application [1].

AM techniques vary in their maximum possible component size, production times, ability to produce complex geometries and product quality in terms of dimensional accuracy and defects. With PBF, the time for production can be quite high because of limits related to feed rate of the powder, low layer thickness and scanning speed. This makes it more suitable for smaller parts. The smaller powder particles compared to other processes allow for a better surface finish and more intricate geometries. Improved dimensional accuracy is achieved with electron beam and laser due to controlled melting and solidification, as compared to DED (directed energy deposition), especially with the DED wire feedstock-electric arc process where intricate shapes are not possible. The main factors affecting the product surface quality include type of alloy, shape, morphology and size of the powder, focal spot size of the heat source and parameters of the chosen process [1].

1.1 Laser Powder Bed Fusion (L-PBF)

Laser powder bed fusion (L-PBF) is a fast growing manufacturing technique, with significant quality improvements in recent years, which uses a laser to melt a metallic powder according to a design specified on a 3D design program. This is done in layers, until the component is completed [1]. The process starts with the designing of a part in a 3D-CAD program. This model is sliced into layers and transferred to the L-PBF machine. Then, the metal alloy powder is placed on a substrate as a thin layer. The laser then melts the powder in layers, according to the model information it received. This is done in an inert atmosphere, leaving behind a merged solid layer of the part being produced. The laser repeats this for each layer, until the part is completed [1,9].

1.2 L-PBF parameters

Figure 1 shows the parameters that control the L-PBF process. The most important parameters are laser power, scanning speed, layer thickness and hatch spacing [4].

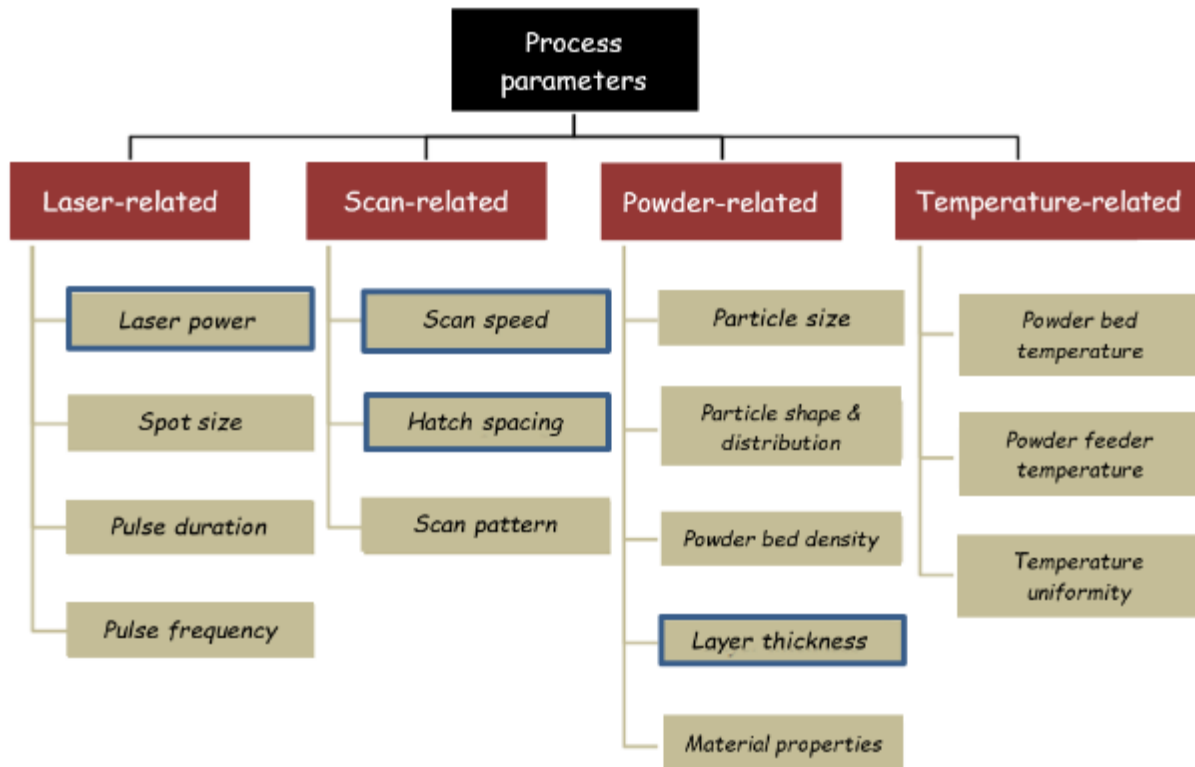


Figure 1: Process controlling parameters [4]

Hatch spacing refers to the distance between two laser beams in sequence [10]. Hatch spacing and the three other main parameters are illustrated in Figure 2.

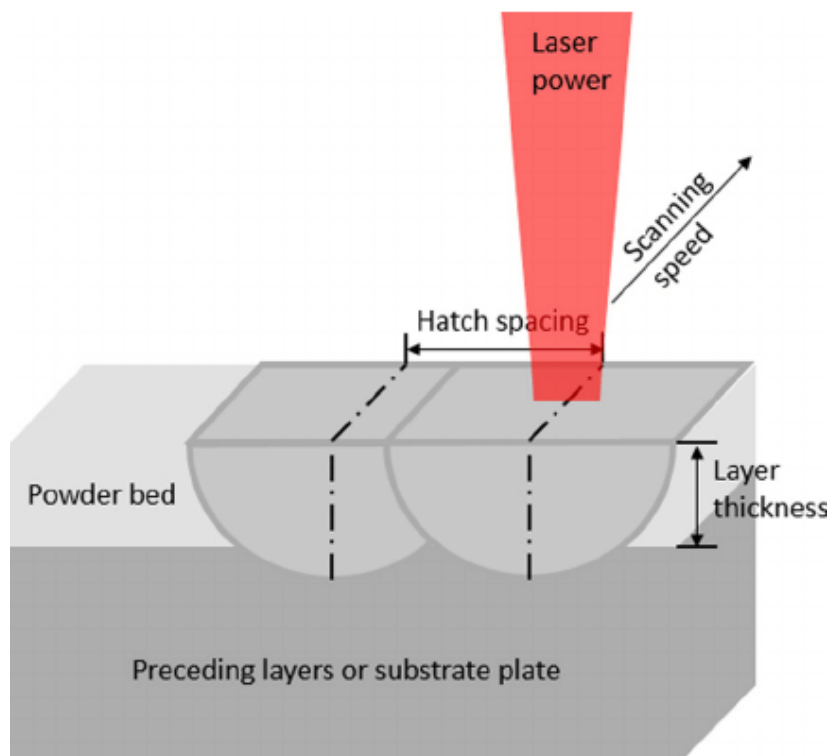


Figure 2: Illustration of the four main process parameters in L-PBF [11]

The parameters that affect L-PBF can be split into four categories, namely laser, powder, temperature and scan-related [4]. Different combinations of these variables lead to changes in quality of the printed parts. These changes are observed in the mechanical properties, microstructures and surface finish of the parts. A relatively recent study has shown that shielding gas flow can also influence the quality of the printed parts [12]. It provides an inert atmosphere to avoid nitration or oxidation by reducing the pick-up of reactive gases in the liquid metal. The shielding gas is also used to remove by-products of the process, such as spatter particles [12]. This means the gas flow needs to be homogeneous over the build platform, to ensure sufficient removal.

The processing and design parameter ranges for L-PBF is shown in Table Figure 1. It should be noted that this table only gives a general overview across a range of L-PBF machines and for different materials.

Table 1: Ranges for typical L-PBF processing and design parameters [1]

Parameter	Range
Power (W)	50 – 1 000
Scan speed (mm/s)	10 – 1 000
Maximum build size (mm x mm x mm)	500 x 280 x 320
Dimensional accuracy (mm)	0.04 – 0.2
Surface roughness R_a (μm)	7 - 20

2. The porosity of L-PBF parts

There are three main types of porosity in L-PBF parts, namely spherical pores (usually entrapped gas), lack of fusion defects and keyhole pores [13]. The unmelted powder, or lack of fusion defects (LOFDs) come from insufficient overlap during the melting process, or insufficient power for melting. This either creates an area of poor bonding or in extreme cases also unmelted powder in the cavities remaining [14]. With keyhole pores the mechanism is different. Here a depression well is formed with vapour which becomes unstable and this can create a keyhole pore. Examples of each of the three porosity defects are shown in Figure 3.

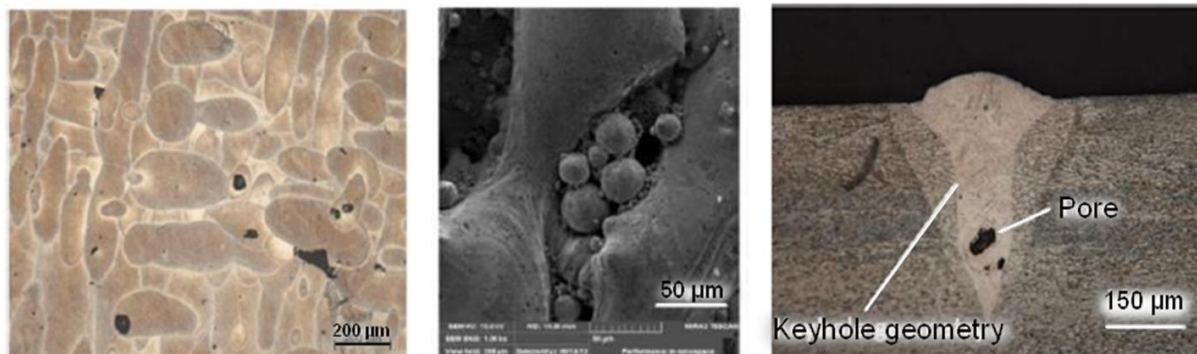


Figure 3: Examples of possible defects (left) spherical pores, (centre) unmelted powder and (right) keyhole pore [13]

Porosity in L-PBF parts is usually influenced by scanning speed, laser power, the thickness of the layers and energy density, amongst many other parameters. Energy density is a simple relation used to evaluate the process parameters but needs to be used carefully [15]. Equation 1 defines energy density as a function of beam power (P), scan speed (V), layer thickness (L) and hatch spacing (H) [16]:

$$\text{Energy density} = \frac{P}{VHL} \quad \text{Equation 1}$$

If power, layer thickness and hatch spacing are kept constant, this equation shows that the scan speed and energy density are inversely proportional. However, this relationship does not take spot size of the laser into account, or many other unique properties of different laser beams, powder sizes, ambient conditions and material specific properties. This means that the concept of energy density must be used only as a rough indicator and should be used with care - even with the same energy density significantly different melting conditions can occur.

From the schematic illustration in Figure 4 it can be seen that high scanning speeds, and therefore low energy density, lead to lack-of-fusion pores forming and on the other hand, low scanning speeds with high energy density create keyhole pores. It can also be seen that porosity never fully reaches 0%, even at intermediate levels. Depending on the material, the optimal energy density will change.

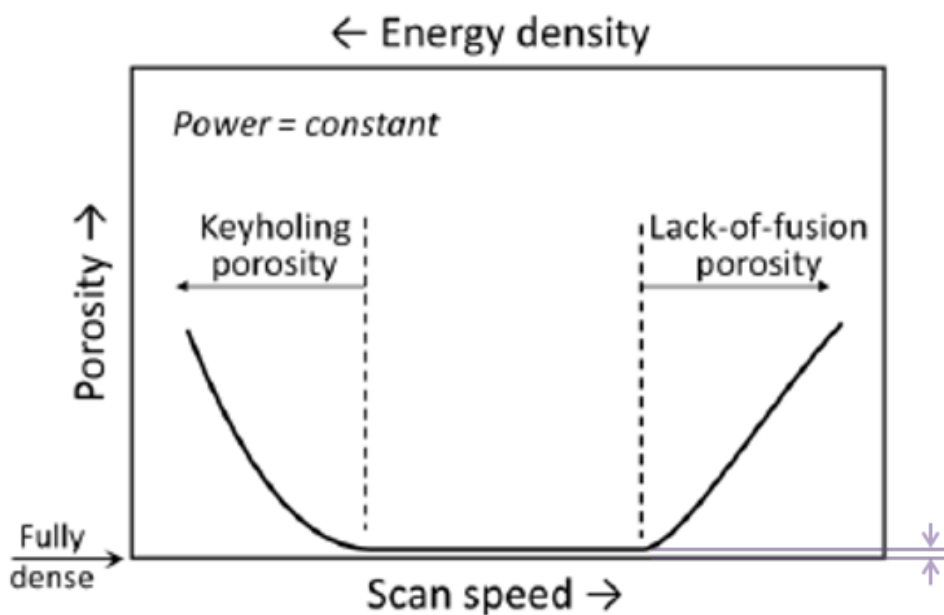


Figure 4: A typical trend of part porosity with changes in scan speed and energy density (at constant power) [16]

Finding an optimal combination of process parameters has been shown to minimise porosity down to 0.01%, so 99.99% dense [17]. The onset and transition in pore types were shown to differ between keyhole mode and lack-of-fusion pores, with the lack-of-fusion transition being much sharper than the keyhole mode with changing power [17].

3. The alloy AlSi10Mg

AlSi10Mg is an aluminium alloy containing approximately 10% Si and 0.35% Mg. It is typically used in the automotive and aerospace industries due to its high strength to weight ratio, and has good thermal conductivity so is also used for cooling/heat dissipation of components in electronics [6–8]. The typical chemical composition is shown in Table 2 for the additive manufactured (AM) and cast AlSi10Mg alloy.

Table 2: Chemical composition range of AlSi10Mg in AM and Casting

	Si	Mg	Ti	Zn	Cu	Ni	Al
AM [6]	9.00 – 11.00	0.25 – 0.45	0.00 – 0.15	0.00 – 0.10	0.00 – 0.05	0.00 – 0.05	Bal.
Cast A360 [8,18]	9.00 – 10.00	0.40 – 0.60	0.00	0.00 – 0.50	0.00 – 0.60	0.00 – 0.50	Bal.

3.1 Microstructure

Figure 5 shows the typical microstructure of the L-PBF as-built AlSi10Mg alloy in Figure 5(a), with Figure 5(b) showing a high magnification image taken with SEM to illustrate the eutectic silicon (Si) that segregates on the α -Al grain boundaries.

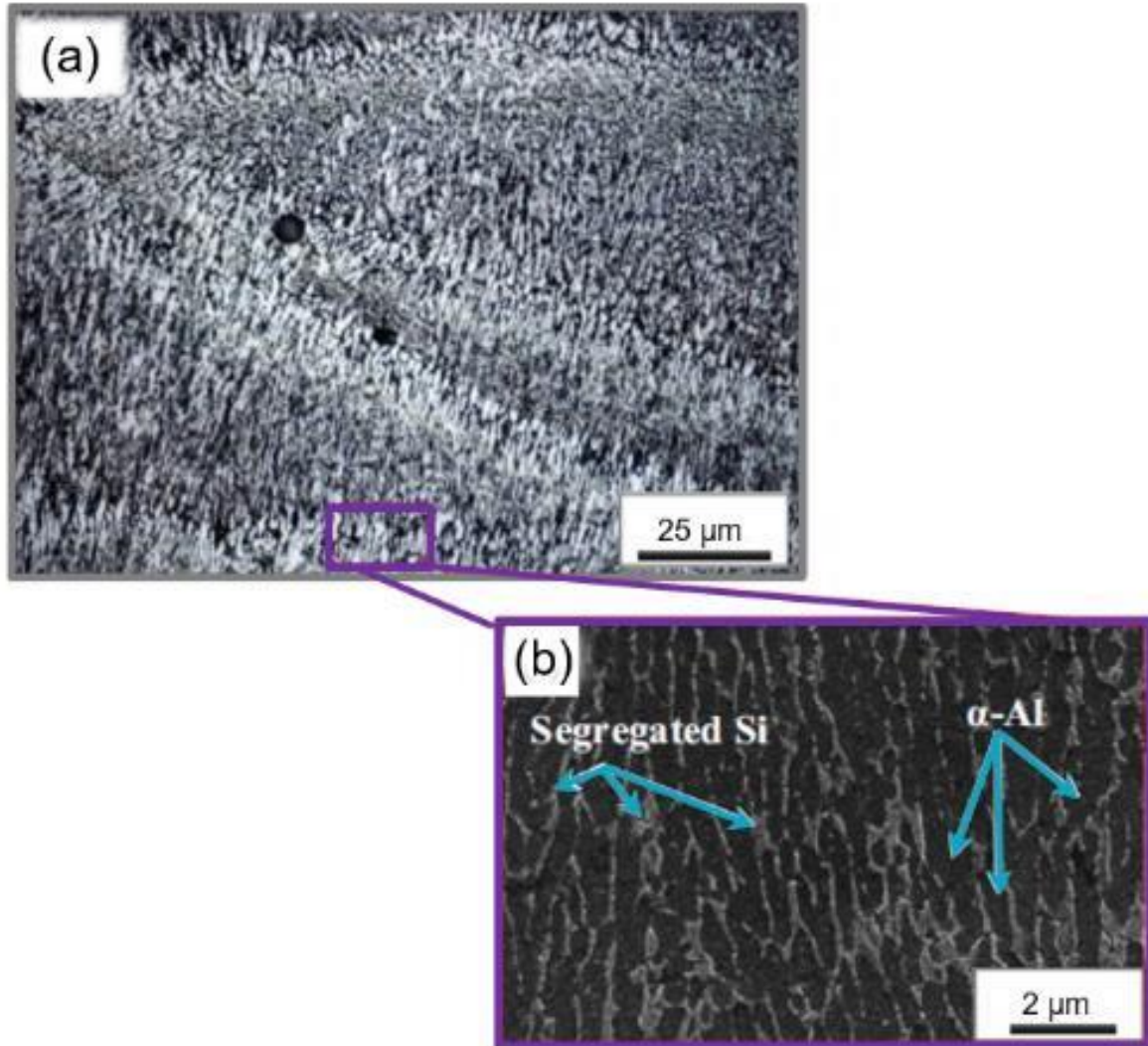


Figure 5: Microstructure of (a) the as-built L-PBF AlSi10Mg with (b) high magnification SEM image revealing Si segregated on the boundaries of α -Al [19]

The eutectic, acicular Si is present as inter-dendritic arms along the α -Al grain boundaries, with the α -Al grains present in columnar form [5,19]. Figure 6 shows an isometric view of an AM cube in Figure 6(a), with the typical microstructure for two of the planes in Figure 6(b) and Figure 6(c). This microstructural anisotropy can cause anisotropy of mechanical and other properties in the manufactured part.

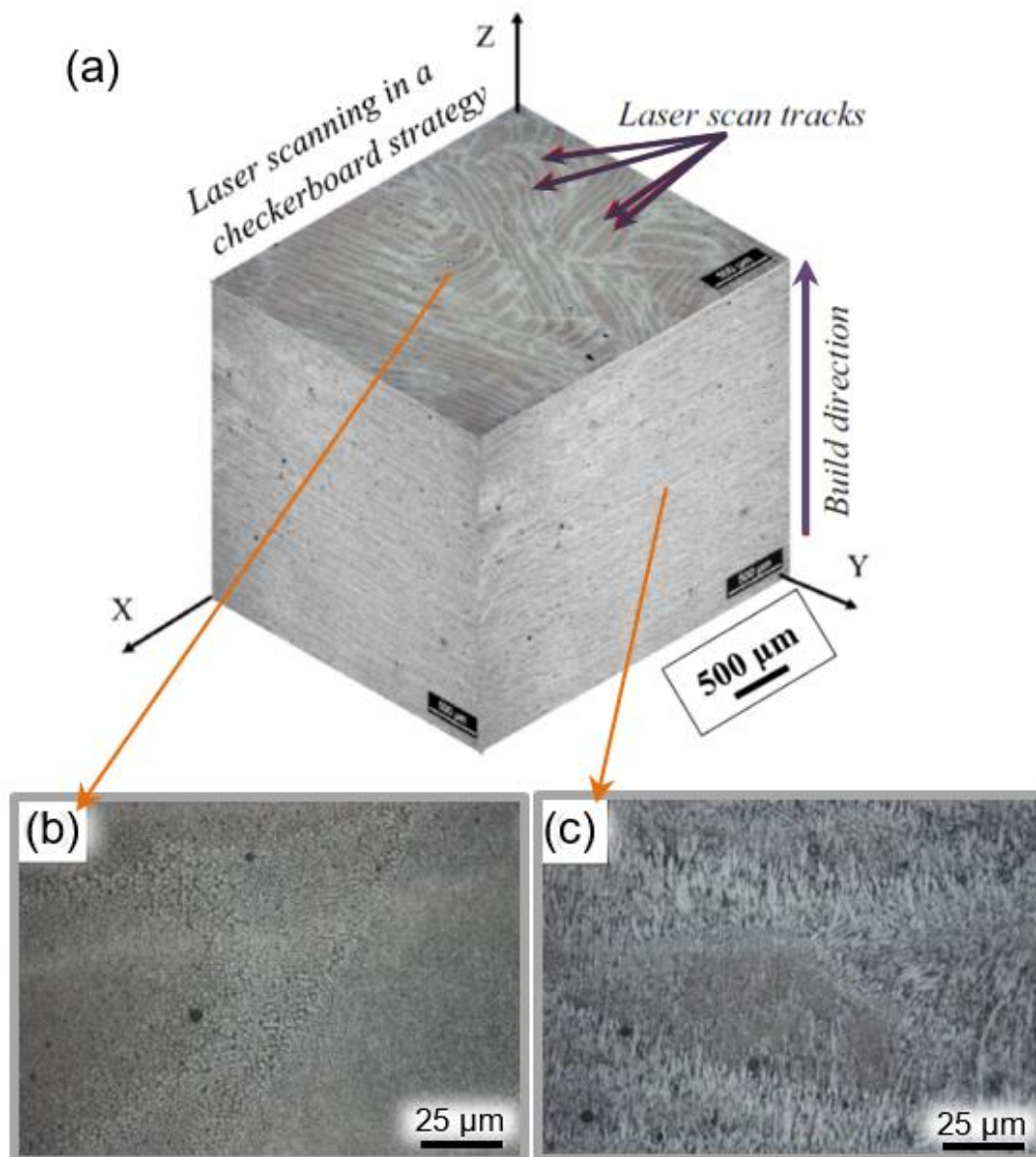


Figure 6: (a) Isometric view of L-PBF cube showing 3 views, microstructure of as-built (b) XY-plane and (c) XZ-plane (Adapted from [20])

The amount of Si that remains in the liquid is reduced through fast cooling by extending Si solubility in the Al, which means the α -Al solidifies preferentially in the cellular structure, thereby leaving residual Si to accumulate at the grain boundaries [20].

3.2 Characterisation of L-PBF parts

The microstructure is initially defined by the rapid cooling rate of the L-PBF process, which leads to an ultra-fine-grained structure [21]. For an Al-Si system, the aluminium matrix is cellular and supersaturated with a surrounding silicon particles network [22].

Conventional Al-alloy castings form large needle- or rod-like silicon (Si) particles in the aluminium (Al) matrix, however with L-PBF; the microstructure is typically eutectic with very small silicon particles. The aluminium matrix is initially cellular-dendritic. The fine and fibrous silicon dispersion improves the mechanical properties of the as-built alloy.

There are three distinguishing zones in the melt track of cellular nature, namely the C zone (coarse cellular), the F zone (fine cellular) and the T zone (transitional) [23].

This is shown in a close-up in Figure 7 and as the basis image in Figure 8(a). There is a transition zone between the coarse cellular zone and the fine cellular zone, indicated with yellow dashed lines.

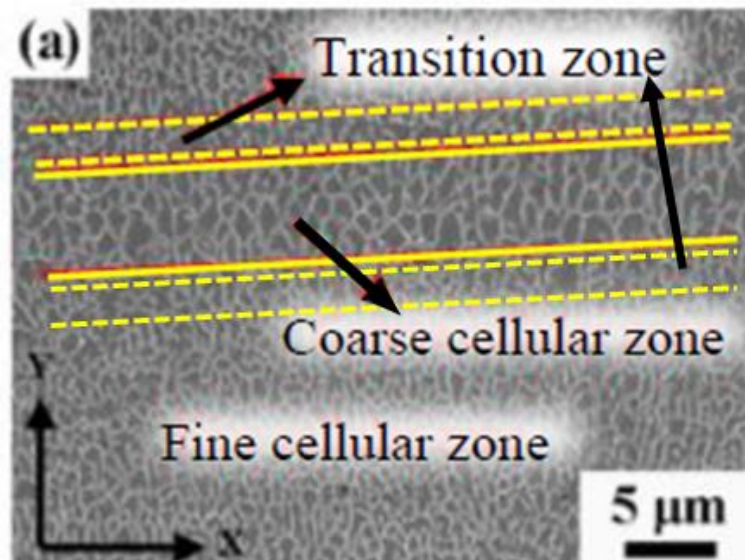


Figure 7: Microstructure with three distinguishing zones outlined. (Adapted from [23])

In the T zone in Figure 8(b) it can be seen that the network of eutectic Al-Si is partly broken by silicon coarsening into idiomorphic particles. This is attributed to the diffusion rate increase of silicon. Figure 8(c) shows the melt pool interior with F zone.

Figure 8(d-f) shows the effect that solution heat treatment has on the microstructure. The microstructure coarsens more as temperature is increased from 450 °C to 550 °C, each for two (2) hours [23]. For the lower solution treatment temperature, the silicon particles are still small and dispersed uniformly in the matrix, but as the temperature increases, the silicon particles start coarsening. Artificial ageing further coarsens the microstructure, as shown in Figure 8(g-i). This coarsening shows that the supersaturated silicon in the as-built aluminium matrix is precipitated out with heat treatment. This decrease in number of particles can be due to particle coalescence or Ostwald ripening. Ostwald ripening is when small particles dissolve and are then deposited onto larger particles [23].

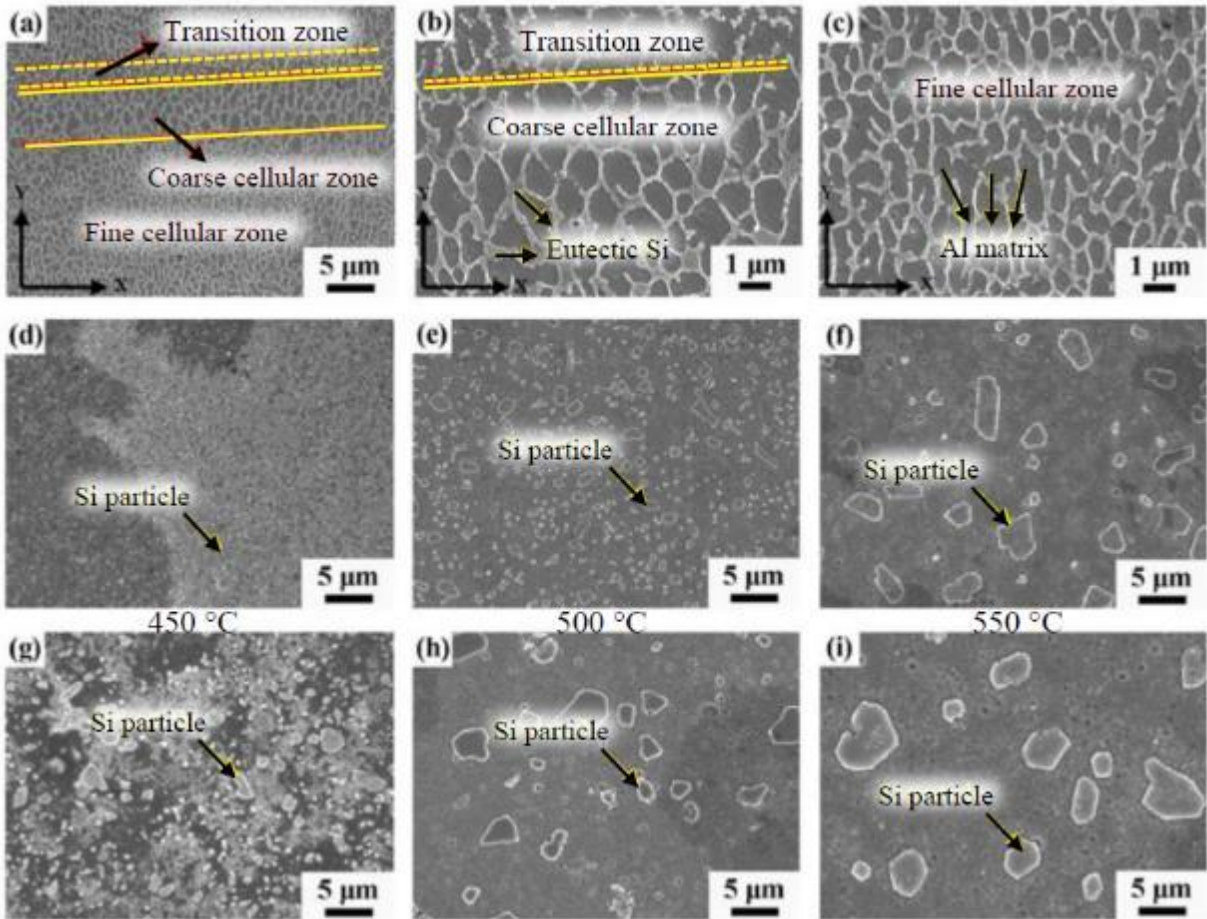


Figure 8: Microstructural evolution of L-PBF AlSi10Mg with (a-c) as-built condition, (d-f) solution heat treatment and (g-i) solution treatment and artificial aging [23]

Schematically, the eutectic silicon in the supersaturated Al-matrix is rejected so that they can form small particles, thereby blurring the cellular boundaries, as shown in Figure 9 from Phase A to Phase B. The silicon particles tend to precipitate along the cellular boundaries, coarsen and then distribute evenly over the matrix surface, as shown in Figure 9 with Phase C [23].

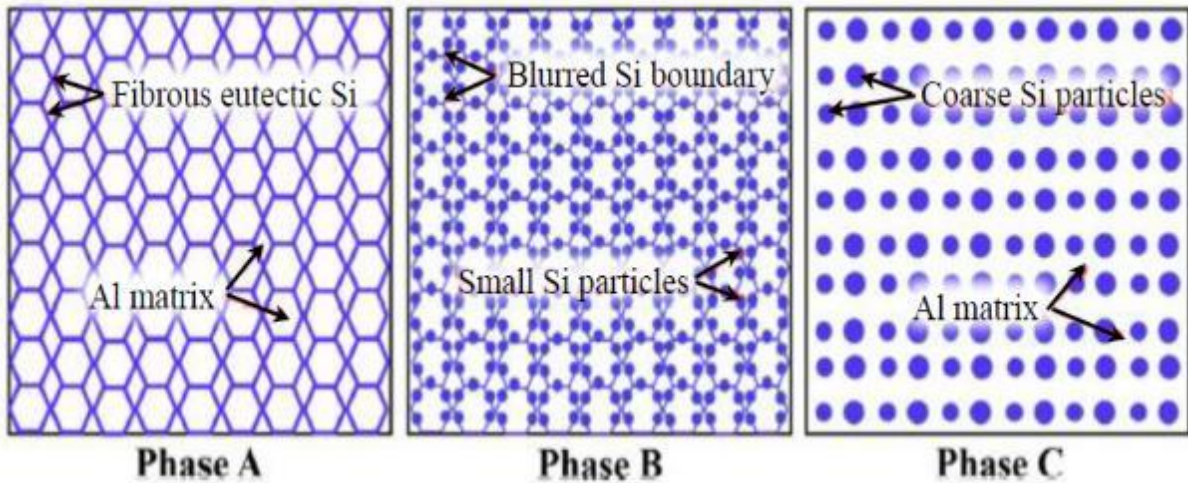


Figure 9: Microstructural evolution schematic during solution treating and artificial ageing [23]

The higher strength of the as-built Al-alloy is attributed to its fine microstructure which is a result of the rapid melting and solidification it experiences during printing [20,21]. As the microstructure coarsens, the strength is adversely affected. This is demonstrated in the Hall-Petch equation, shown in Equation 2 [24]:

$$\sigma_0 = \sigma_f + \frac{K_y}{\sqrt{D_{GS}}} \quad \text{Equation 2}$$

Where σ_0 is the yield strength, σ_f is the friction strength opposing dislocation motion, K_y is a strengthening coefficient which is unique for each material, and D_{GS} is the grain size [24]. The equation shows that the strength of a material has an inverse relationship to its grain size, meaning as the grain size becomes smaller, the strength increases [25].

3.3 Alloy properties

Table 3 shows the typical mechanical properties for AM-AISi10Mg in the as-built condition as well as after a T6 heat treatment. A T6 heat treatment refers to solution heat treating (five hours at 530 °C, water quench [26,27]) and artificially ageing (11-12 hours at 160 °C [26,27]) to peak hardness [28].

Table 3: Mechanical properties of L-PBF AISi10Mg as-built and in T6 condition [19]

Mechanical Properties	As-built	T6 condition
Ultimate Tensile Strength (MPa)	333±15	292±4
Yield Strength (MPa)	268±2	239±2
Elongation (%) [19]	1.4±0.3	3.9±0.5
Elongation (%) [22]	4	10
Hardness (HV)	125±1	100-105

Table 4 shows the mechanical properties obtained after a typical stress relief treatment, which is two (2) hours at 300 °C, followed by air cooling [3,6,26,27,29,30]. The heat treatment is done in a vacuum- or argon-atmosphere oven.

Table 4: Mechanical properties of L-PBF AISi10Mg after stress-relieving heat treatment [29–31]

Mechanical Properties	As-built	Stress-relieved
Tensile Strength (MPa)	302-443	257-319
Yield Strength (MPa)	177-277	151-207
Elongation (%)	3.9-8.0	7.0-19
Elongation (%) [32]	6-9	11-12
Hardness (HV)	125-127	107±5

The values as seen in Table 3 and Table 4 are a combination of values obtained from three different sources. These sources most likely used different process parameters for L-PBF, which can lead to the large variation in values seen. It can be seen from Table 3 and Table 4 that the elongation values found for the as-built samples vary. This is due to each source using different process parameters, L-PBF machines and powders. They are not recommended values, but values obtained in specific studies [19,22], and from powder suppliers [29,33]. In Table 5 the mechanical properties of the as-cast die-cast A360 is compared to the as-built L-PBF AISi10Mg. As there is no anisotropy in die-cast A360 compared to anisotropy in L-PBF AISi10Mg, this will create a difference in mechanical property values obtained for both.

Table 5: Mechanical properties comparison between die-cast A360 and L-PBF AISi10Mg for as-produced state

Mechanical Properties	As-built AISi10Mg	A360-F
Tensile Strength (MPa) [8,18,19,29,34]	333, 425-478	300-350
Yield Strength (MPa) [8,18,19,21,29,34]	252-290	160-185
Elongation (%) [8,18,19,22]	1.4-4.0	3-5
Elongation (%) [21,29,32,34]	4-6, 6-9	3-5
Vickers hardness (HV) [21,26,30,34–36]	120-127, 116-136	95-105

There is good correlation for yield strength. The strength (both tensile and yield) and the hardness are much higher for L-PBF than for the die-cast alloy. In Table 6 the properties are compared in the T6 condition.

Table 6: Mechanical properties comparison between cast A360 and L-PBF AlSi10Mg for T6 condition

Mechanical Properties	AlSi10Mg-T6 [19]	A360-T6 [21,34,36]
Tensile Strength (MPa)	292	330-365
Yield Strength (MPa)	239	285-330
Elongation (%)	3.9	1.6
Elongation (%)	10 [22]	3.5
Vickers hardness (HV)	100-105	130-133

From Table 6 it is clear that the die-cast A360 exhibits improved hardness after a T6 treatment, but the L-PBF AlSi10Mg has decreased values compared to as-built. For L-PBF, the T6 treatment improves elongation at the cost of reduced strength and hardness. Table 7 shows the mechanical properties comparison between AlSi10Mg made by L-PBF and by casting.

Table 7: Mechanical properties comparison between AlSi10Mg produced by L-PBF and by casting for as made and T6 [37]

Mechanical Properties	L-PBF	L-PBF-T6	Cast	Cast-T6
Tensile Strength (MPa)	160	192	193	309
Yield Strength (MPa)	159	171	99	242
Elongation (%)	1.59	1.77	6.52	6.89
Vickers hardness (HV)	107±2	109±3	67±3	108±6

From the tables it can be seen that the as-built L-PBF AlSi10Mg has hardness values comparable to the die-cast Al in the T6 condition. This is attributed to the refined microstructure obtained during L-PBF, compared to the cast microstructure [38]. The difference in T6 responses between the L-PBF and the cast alloy is based on the different strengthening mechanisms that govern. The finer microstructure of the L-PBF alloy results in strengthening by the Hall-Petch effect, which states that the smaller the grain size, the stronger the alloy [25]. On the other hand, the T6 heat treatment strengthens mainly by precipitation hardening. However, coarsening of the L-PBF microstructure occurs during the solution heat treatment resulting in a lower strength in the T6 condition than in the as-built condition.

A study done by Mertens et. al. [38] compared the mechanical properties of the as-built AlSi10Mg with stress-relieved and T6 conditions. For hardness, the as-built had the highest value, followed by stress-relieved, and lowest for T6. The same trend was seen for the ultimate tensile strength (UTS). An inverse relationship was seen for the elongation, as T6 had the highest elongation, and as-built the lowest.

The yield strength, however, had a different response. The T6 condition resulted in the highest yield strength, and stress-relieved the lowest. Microstructural examination of the stress-relieved sample did not show significant differences compared to as-built, so the improvement in ductility is attributed to relief of residual/ internal stresses.

However, the T6 microstructure showed an altered microstructure, where the fine lamellar structure has become completely globular [38].

These are some indicative examples. The study by Aboulkhair et. al. [19] used 200 W laser power and 25 μm layer thickness with a Renishaw AM250 L-PBF machine to print their samples. The tensile samples were ‘dog-bone’-shaped according to the ASTM E8/E8M-15a standard [39]. The results obtained by SLM Solutions [29] was with one of their own machines, with 400 W laser power and 30 μm layer thickness. The tensile samples were tested according to the ISO 6892-1 standard [40].

Table 8 gives the thermal properties for the AlSi10Mg manufactured parts before post-processing.

Table 8: Thermal properties of L-PBF AlSi10Mg [32,33]

Thermal Properties	Metric
Thermal conductivity (W/m-°C)	110 - 120
Specific heat capacity (J/kg-°C)	910 \pm 50

3.4 Influence of Alloying Elements and heat treatment

This Al-alloy has a low density with a high thermal conductivity, along with a very high electrical conductivity and high specific strength. It also has high corrosion resistance [6]. Several papers refer to these properties as a desirable combination for the aerospace and automotive industries where light weight combined with the ability to conduct heat away from the source quickly is required [15,37,41].

AlSi10Mg is one of the most widely researched alloys for aluminium laser powder bed fusion (L-PBF), with a relatively high silicon (Si) content [22]. A lower Si content than with the Al12Si alloys can be beneficial to limit the amount of free, excess Si particles which can provide a path of less resistance for cracks to grow. Fatigue cracks have been found to propagate along the Si particle – AlSi matrix interface [42]. For samples in a tensile test it was seen that the fracture path mainly proceeds through the free Si particles [42]. The addition of magnesium (Mg) to the Al-Si alloy can help improve heat treated strength as opposed to the alloys without Mg, as it forms strengthening Mg₂Si precipitates, thereby also reducing the amount of free Si [22]. Heat treatment is required for AM parts, despite achieving adequate strengths in the as manufactured state, because it also reduces anisotropy (differences in properties as a function of direction) by changing the microstructure [43]. Heat treatment is also often used to reduce residual stress, which can cause anisotropic properties due to local variations in the stress build-up [43]. However, microstructure also plays a role in anisotropy, as mentioned in the description for Figure 6. Heat treatment can also improve the microstructure. It is also important to have a good combination of strength and ductility. It is evident in Table 3 that the as manufactured sample has good strength but is also very brittle. The T6 heat treatment and stress relief treatment both increase the ductility [19,22,29,32].

To understand why the Si and Mg additions are beneficial, it is important to understand the properties of elemental Al powder. Aluminium powder on its own exhibits reduced flowability (powder’s ability to flow in a preferred way [44]) compared to when it is alloyed, making deposition of the powder layer for laser melting difficult [22].

This is mostly due to the inherent low density of aluminium and the powder's irregular shape. The irregular shape is a result of oxide islands forming during atomisation, creating pinning points and interfering with the surface tensions trying to form spheroids [22]. Gas atomisation is a process where molten metal is subjected to a jet of air, helium, nitrogen or argon at high velocity and subsequently dispersed. Nitrogen or argon is used to reduce the oxygen content and prevent oxidation during atomisation and powder production [45].

Figure 10 shows the powder morphology for AlSi10Mg, in comparison with a Ti-6Al-4V powder. It can be seen that the Ti-alloy powders are more spherical than the Al-alloy grains [22,46]. Both the AlSi10Mg and Ti-6Al-4V powders from Figure 10(a) and Figure 10(b) respectively were gas atomised [46]. The AlSi10Mg and Ti-6Al-4V powders from Figure 10(c) and Figure 10(d) respectively were obtained from Electro Optical System (EOS) GmbH, Germany [47,48].

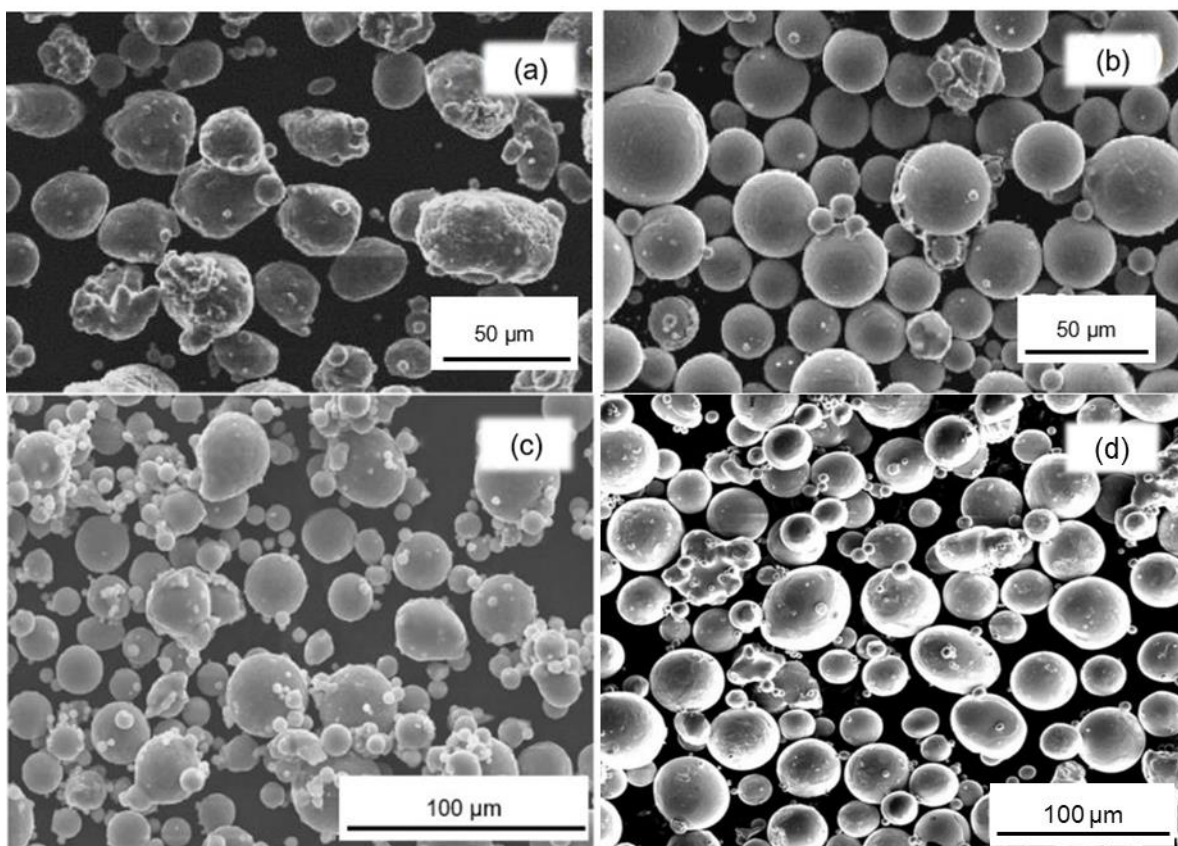


Figure 10: SEM images of (a) AlSi10Mg and (b) Ti-6Al-4V powder [46] with 50 µm scale bar and (c) AlSi10Mg [47] and (d) Ti-6Al-4V powder [48] with 100 µm scale bar

Another characteristic of aluminium is its high reflectivity, meaning a higher than usual laser energy for melting is needed. The amount of absorption will differ from the already melted solid to the fresh powder, creating temperature gradients during overlapping scans. This in turn can lead to balling (spherical particles that cluster on the surface of the manufactured component [49]) via convective heat flow. The addition of silicon to the alloy increases the absorptivity, allowing the alloy to be melted more easily [22].

Along with its high reflectivity, aluminium also has high thermal conductivity. This means that not only does a large amount of energy from the laser get reflected, but the heat is also conducted away from the melt pool quite rapidly [22].

The silicon addition is beneficial in this regard as well, as the Al-Si alloy system has a smaller range of temperatures wherein it solidifies, thereby experiencing more isothermal solidification. This decreases the risk of distortion and cracking [22].

With the alloy in powder form, the size distribution as well as shape becomes important, since a more spherical shape will improve flowability. However, too fine particles can reduce flowability and if the particles are too large, then the required laser energy for melting the entire particle is increased. If there is already porosity present inside the powder (as is typical for gas atomisation), this can introduce porosity into the printed part [50]. The typical particle size of the powder for LPBF of AlSi10Mg ranges from 20 to 63 μm [29].

4. Micro- and NanoCT scanning

MicroCT scanning (Computed Tomography) is used for determining not only that there is structural integrity, but also for dimensional accuracy in the build of AM parts. It is also a non-destructive test (NDT). The process uses X-rays to form a 'shadow' image, as they project past and through the sample. This can pick up the presence of inclusions, cracks or pores [51].

The porosity is quantified and identified and the distribution throughout the sample is verified. Micro- and NanoCT scanners are available, with the MicroCT scanner having a larger size capacity than the NanoCT machine. Unlike normal radiography, the CT scan records these images from various angles while the sample is rotated, thereby creating a full 3D image. This is followed by an algorithm that uses back-projection to calculate the density of the material at each point [51].

The result is a 3D image with higher contrast, location and pore information, such as the distance from pore to surface, amongst others [51]. MicroCT scanning allows for an image with a clear view of where the porosity and corrosion are present in the specimens.

This is illustrated in Figure 11 and Figure 12. Figure 11 shows the porosity analysis of two different cubes where Figure 11(a) shows a large amount of porosity along with irregular shaped pores and Figure 11(b) shows mostly contour porosity.

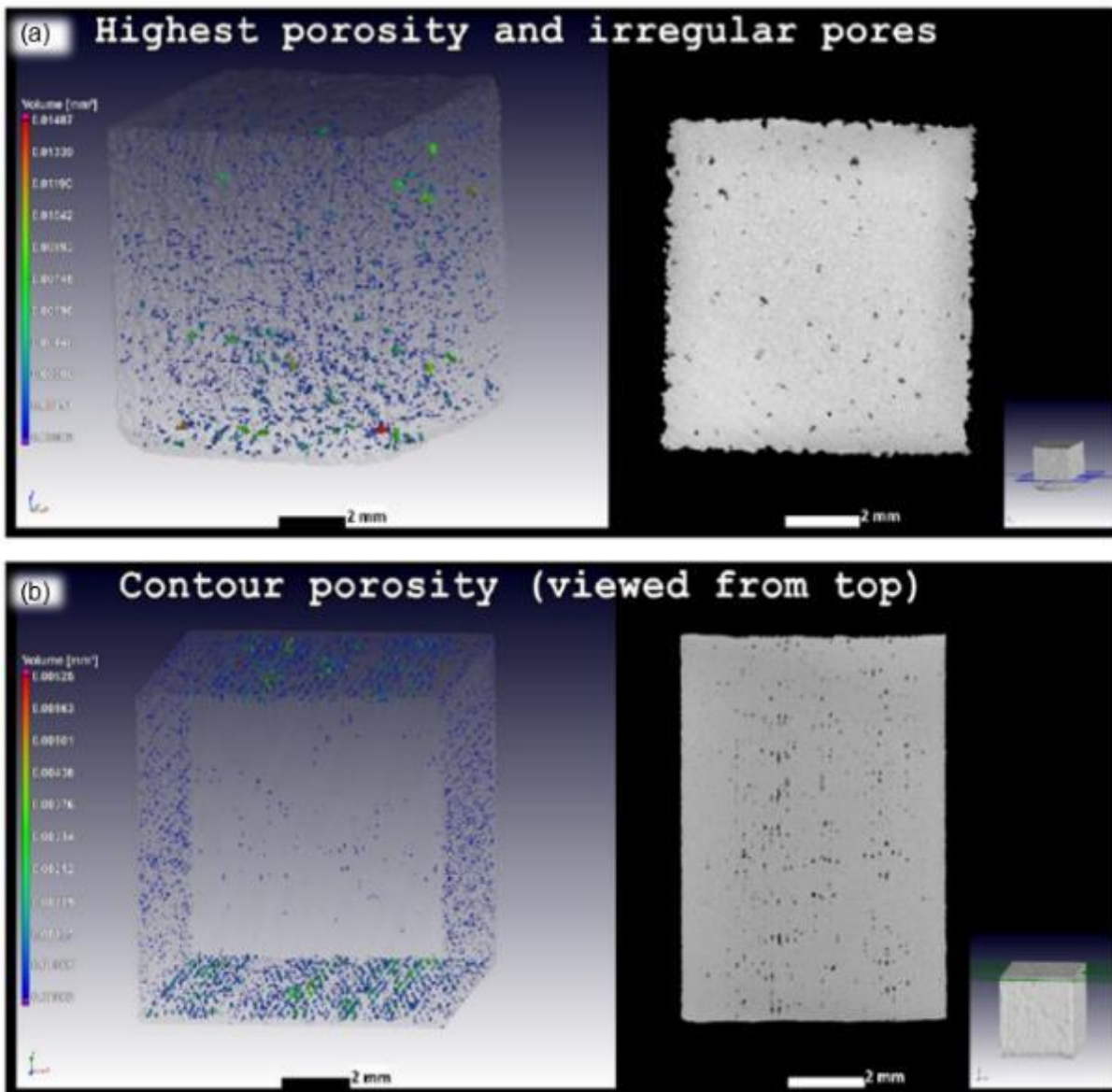


Figure 11: CT scan analysis showing cube porosity for different samples with (a) high porosity and (b) contour porosity [52]

Figure 12 shows two other cubes, with Figure 12(a) displaying subsurface porosity near the top surface and Figure 12(b) has almost no porosity.

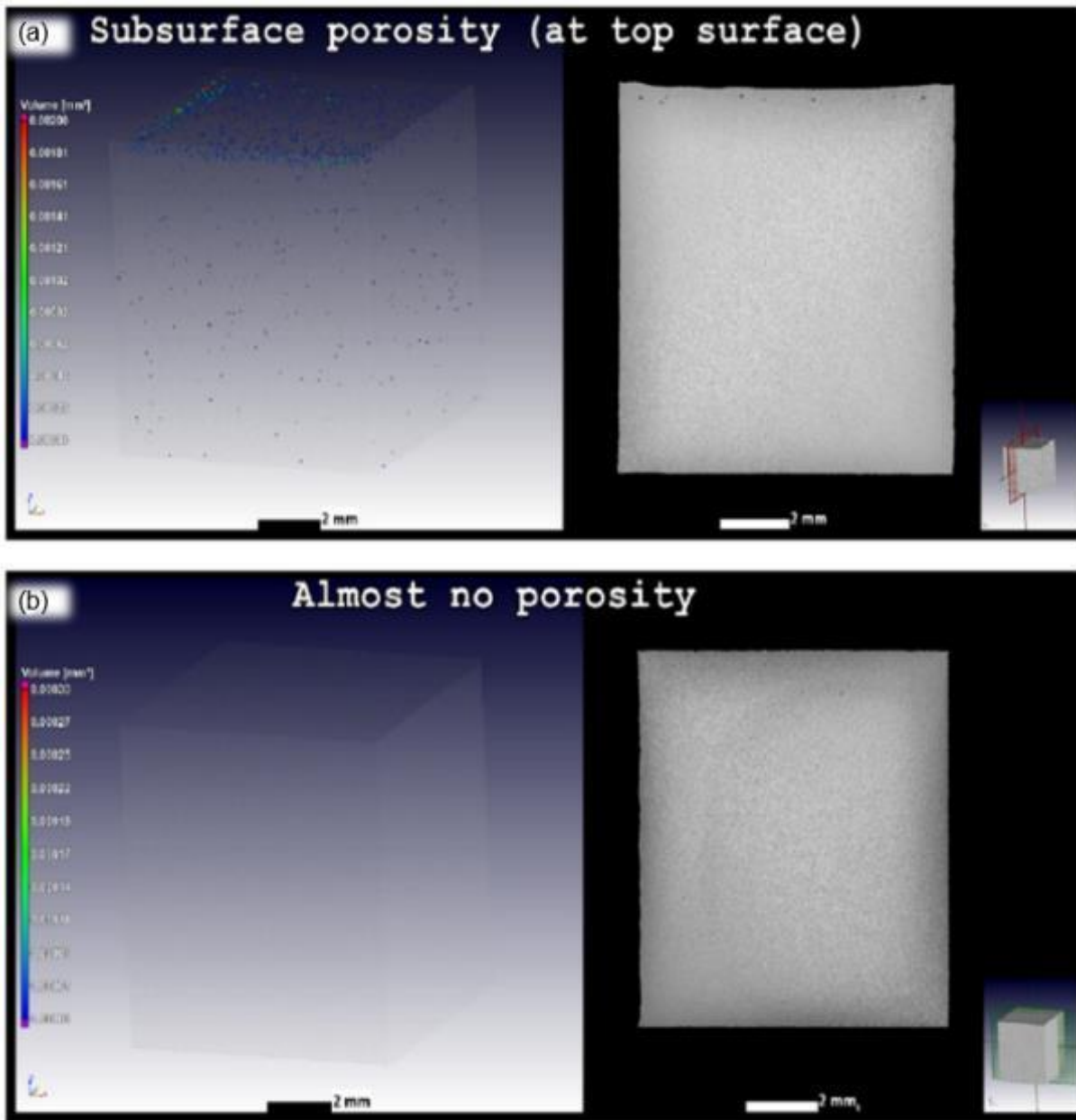


Figure 12: CT scan analysis showing cube porosity for different samples with (a) subsurface porosity and (b) almost no porosity [52]

5 Density methods and measurements

Non-destructive testing (NDT) is useful to determine sample integrity or density without having to destroy the sample. NDT methods that are used often are the Archimedes method, gas pycnometry and X-ray Computed Tomography (CT) scanning.

5.1 Archimedes method

The Archimedes method has the advantage of being relatively simple, cheap and fast. It calculates density based on the part's mass measured in air and measured in liquid (such as water or acetone). It is useful to have a scale that is accurate to at least four decimals. A draft shield will also help to improve accuracy of results as measurements are sensitive to external environmental influences around the sample [53].

The density of the part is calculated according to Equation 3 [54]:

$$\rho = \frac{m_a}{(m_a - m_L)} \times \rho_L \quad \text{Equation 3}$$

Where ρ is the density of the part, ρ_L is the temperature dependent liquid density, m_a is the part mass in air, and m_L is the part mass in the liquid. Acetone is recommended only in its pure form, as it is hygroscopic (absorbs moisture from air), otherwise de-ionised or distilled water is preferred to minimise air bubbles, which will affect the mass measurements [55]. The disadvantage of this method is that it can only determine bulk density relative to the fluid used for measurement, as well as assuming a literature value for 100% dense material. This assumed value can change depending on chemical content, presence of inclusions and microstructure. Porosity present in the part is then determined by comparing the Archimedes density to the reference density for the material. This also means localised pores cannot be individually evaluated [54].

5.2 Gas pycnometry

Gas pycnometry is a process that measures part volume by displacement of an inert gas, usually helium (He). Part density is calculated by measuring the mass and volume of the parts separately. As with the Archimedes method, pycnometry is relatively simple, but the disadvantages of this method are higher equipment costs and volume detection is limited only to parts that are relatively small. This method measures skeletal density, which means that the gas penetrates all open (surface connected) pores and hence excludes them from the measurement. This means porosity is then again determined by comparing the calculated density to the reference density [54]. The principle of gas pycnometry is depicted graphically in Figure 13.

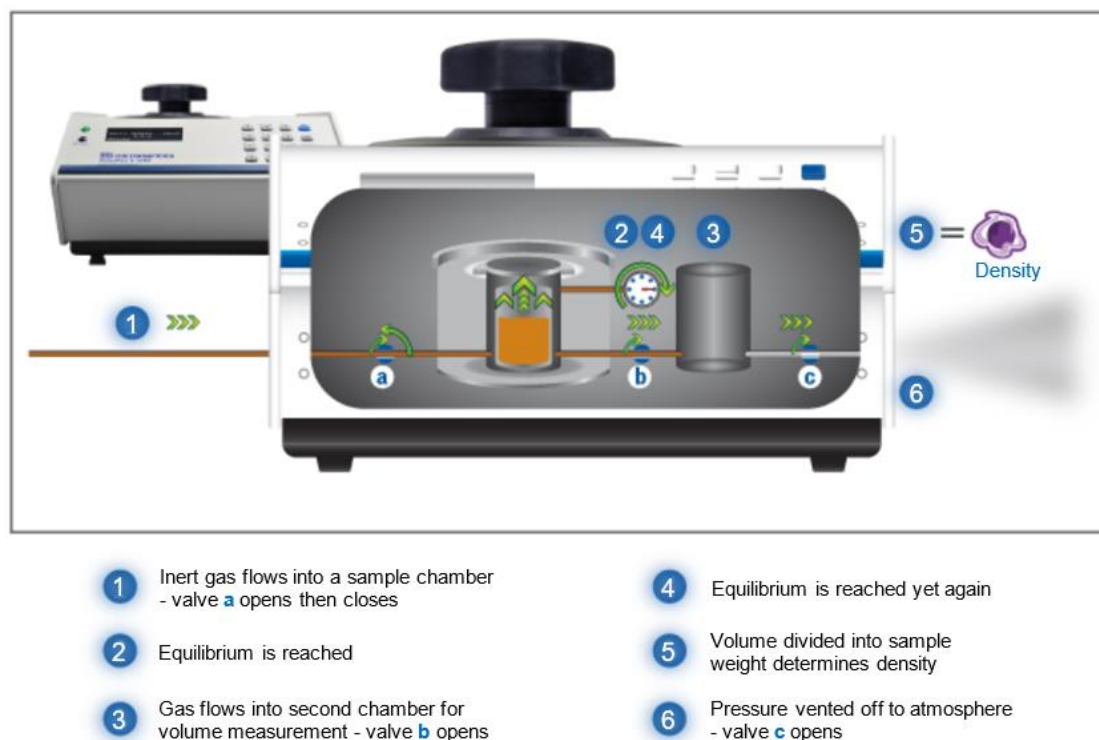


Figure 13: Gas pycnometry principle [56]

5.3 CT scanning

Wits et. al. [54] compared NDT methods and found that CT scans can not only measure pore areas that are smaller than the detectable size for microscopic methods; but also predict higher accuracy densities than Archimedes. It also allows further analysis of the porosity present in the parts, such as measuring sphericity, calculating pore distribution and evaluating defect volume both on the surface and inside the sample [54,57].

6. Corrosion testing

6.1 Salt spray testing

Salt spray testing is an accelerated corrosion test, designed to simulate saline atmospheric environments. It involves placing prepared samples in trays supported on racks, or suspending the samples from the racks in the salt spray fog chamber. The samples are placed at an angle of 15 to 30° from the vertical, to minimise the possibility of droplets stagnating on a horizontal surface (condensation pooling). The chamber is closed, and the test time and chamber temperature are set. The salt solution is atomised and delivered at a constant rate to form a free-falling mist which can settle uniformly over the samples [58,59].

The applicable standard for salt spray testing apparatus is ASTM B117-18 [60]. The salt solution consists of 5 parts by mass sodium chloride (NaCl) dissolved in 95 parts of water. The NaCl should contain less than 0.3% by mass total impurities. The pH should range between 6.5 and 7.2 [60].

Both the ASTM standard as well as the ISO standard (ISO 9227:2012) [61] state that the amount and type of specimen depends on the metal being tested [60,61]. The parameters should be agreed upon between the interested parties [61]. In the military industry a test time of 168 hours is used [62]. The ISO 9227:2012 standard specifies a temperature of 35 °C ±2 °C for a neutral salt spray, as well as recommending exposure times starting from two (2) hours to six (6), 24, 48, 96, 168, 240, 480, 720 and up to 1 000 hours [61].

Acetic acid salt spray testing can be done if neutral salt spray testing does not yield significant results. It is a recommended test for aluminium alloys with organic coatings. The temperature and salt concentration remain the same as for the neutral salt spray, but the pH is lowered to between 3.1 and 3.3 using glacial acetic acid [61].

Previous studies with L-PBF AlSi10Mg using salt spray testing have been done. One study by Lancea et. al. [63], used exposure times from 100 hours in 50 hour increments up to 250 hours. Salt solutions of both 5% NaCl as well as 10% NaCl were used. They concluded that this type of accelerated corrosion test was an efficient way to determine the corrosion behaviour [63]. The study by Zaharia et. al. [64] used ISO 9227 [61] with 5% NaCl and an accelerated test with 10% NaCl for a honeycomb lattice structure. A total exposure time of 240 hours was used, with a time step at 96 hours. They found that the corrosion rate increased with an increase in exposure time [64]. Another study by Zakay & Aghion [65] used a salt solution of 5% (NH₄)₂SO₄ + 0.5% NaCl for 40 days at 40 °C. They tested samples in the as-built condition as well as heat-treated at 200 °C, 300 °C and 400 °C [65].

The results showed that the samples heat treated at both 200 °C and 300 °C had the lowest corrosion rate, followed by the untreated samples. The samples heat treated at 400 °C had the highest corrosion rate [65].

A study was carried out by Forn et. al. [66] on corrosion behaviour of a copper (Cu) and silicon (Si) containing Al-alloy produced by semi-solid rheocasting, using acetic acid salt spray testing. Samples in the as-cast, T5 (artificially aged) and T6 (solution treated and artificially aged) conditions were tested. The cross-sectional surfaces of the samples are shown in Figure 14. The T6 sample shows the smallest pitting depth of the three samples.

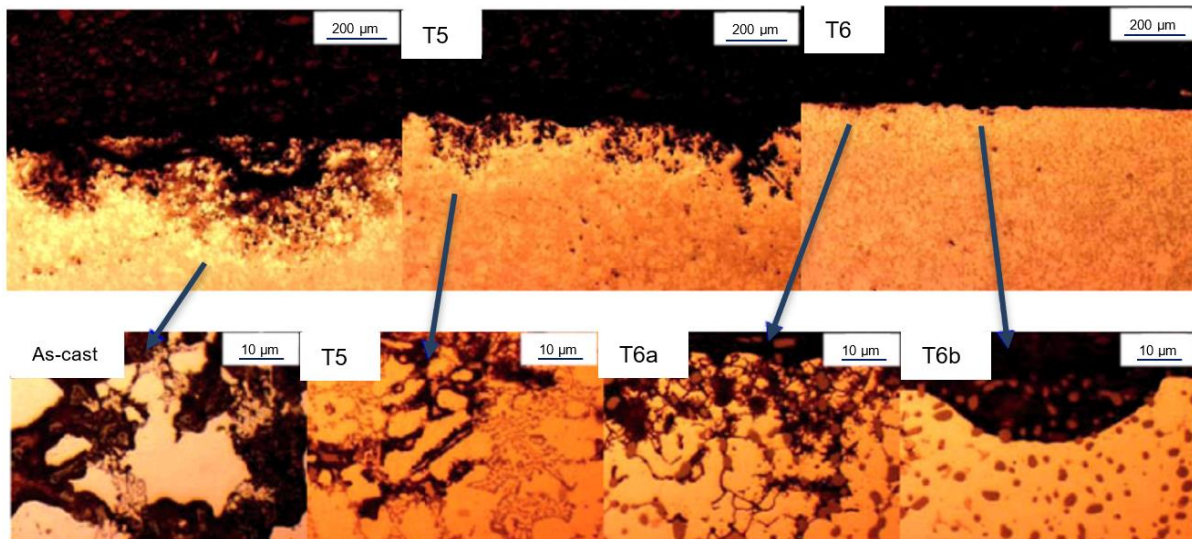


Figure 14: Cross sections after 72 h in acetic acid salt spray [66]

Forn et. al. [66] identified the intermetallics present in the samples through SEM analysis. The as-cast and T5 samples contained AlFeSi, AlFeMgSi, AlCu, Si and AlCuFeMn particles. The T6 sample only contained Si and AlCuFeMn particles. Corrosion occurred preferentially through eutectic Si regions and around the intermetallics. This was linked to their cathodic behaviour compared to the α -Al. The T6 corrosion process occurred through two mechanisms. Firstly, advancing of corrosion around the intermetallics (Figure 14 T6a) and secondly by semi-circular pitting of the matrix. When the Si particles are spread further apart it hinders the advance of the corrosion around them [66].

7. Surface roughness

Usually Al parts manufactured using L-PBF can have a surface roughness ranging from 7 μm up to 20 μm [1,67]. Surface roughness depends on aspects such as part geometry, surface orientation, powder size, laser power, layer thickness and scan speed [68]. Spatter, partially melted powder and balling can lead to extensive bad surface conditions [69]. Of these three, spatter particles are the largest at roughly 200 μm in size. These particles are larger than the mean powder size as they spatter from the melt pool and land on the surface of the powder bed, melting back into the next layer (combining with other particles). However, when this spatter is too close to the contours, the melting is only partial, and remains on the surface [69].

The size of the partially melted powder particles are close to the size of the powder bed particles, i.e. 20 μm to 50 μm [69]. The balling effect is seen at higher scan speeds, decreasing surface quality. The elongated melt pool experiences a division effect which causes the balling [4]. It should be noted that extensive lack-of-fusion, lack of contour scanning and other interrelated parameters of the L-PBF process can also lead to higher surface roughness [68].

Surface roughness is usually measured with a machine that uses a calibrated stylus to measure the differences in surface texture along a line and giving the average value. The surface profile can also be acquired in CT scanning at a high resolution, allowing investigation of the surface profile such as in [52,70,71]. This is illustrated in Figure 15.

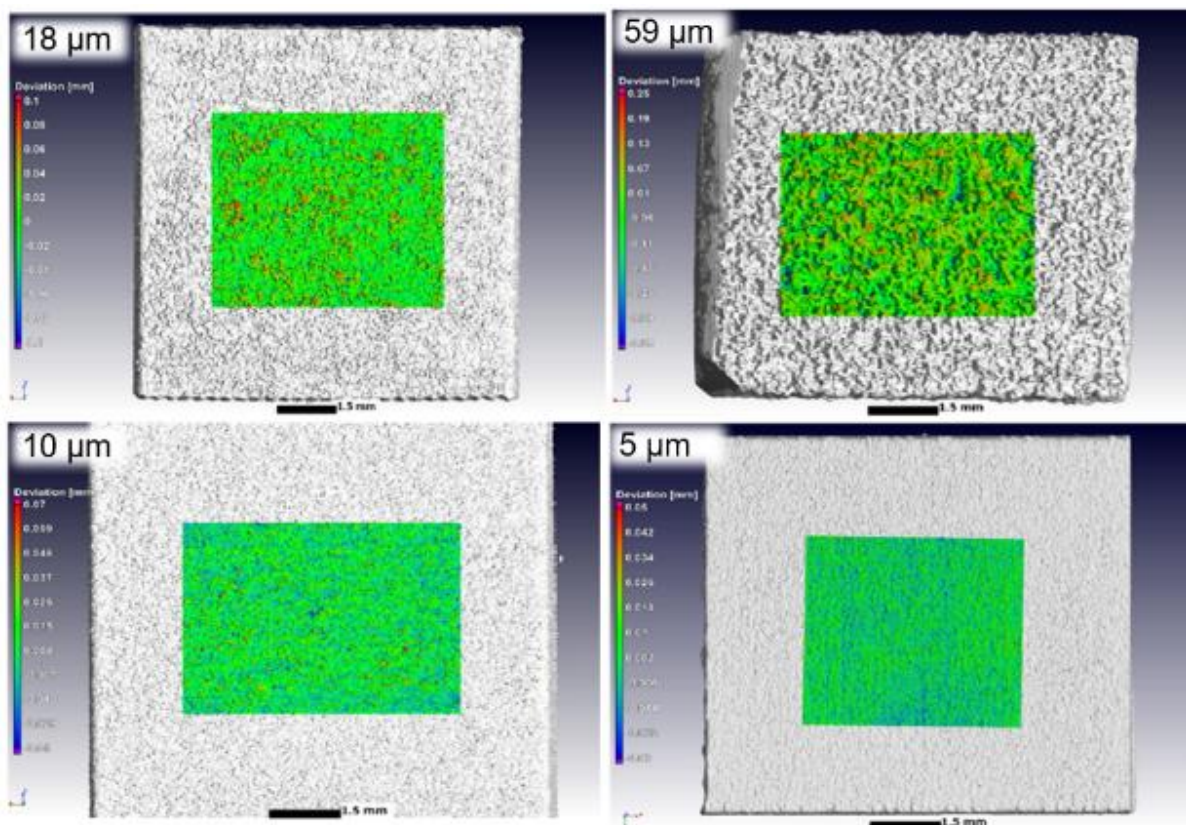


Figure 15: CT scan analysis showing surface roughness measurements for four different cubes, with the CT-derived areal roughness S_a values superimposed on the corresponding images [52]

Surface roughness can also be measured using an optical microscope with analytical software to plot a surface map of the sample and return surface roughness values, such as S_a (difference in each measurement point's height compared to the average of the surface [72]) and S_z (surface profile defined as the maximum height between the largest peak and largest pit in an area [73]), along with a colour scale three-dimensional (3D) map showing the dips and peaks of the surface. This method uses S_a rather than R_a , as the software takes the line roughness profile parameter R_a (average of individual measurements over a line's valleys and peaks [74]) and expands it three-dimensionally, i.e. it calculates over an area rather than just a line.

This is the same method as with the CT-based roughness method, using the optical microscope to obtain the surface points instead of X-ray tomography. This makes S_a the arithmetical mean height, the average of the $Z(x,y)$ ordinate within the area analysed [75]. The S_a principle is shown in Figure 16.

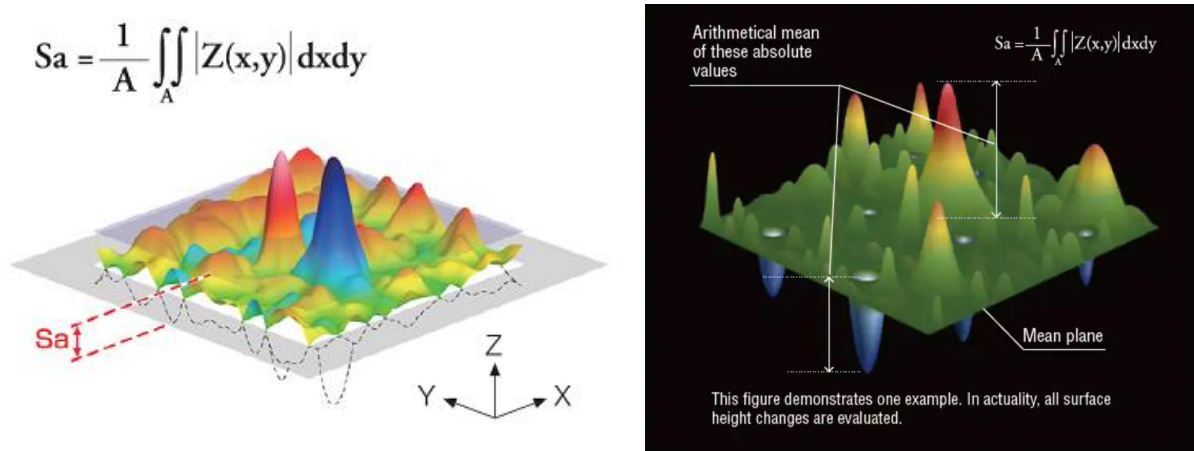


Figure 16: Schematic of the S_a measurement principle (left) [75] and (right) [72]

8. Al-alloy corrosion

Aluminium and its alloys are susceptible to various forms of corrosion, such as:

- 1) Pitting
- 2) Galvanic
- 3) Intergranular
- 4) Stress
- 5) Crevice
- 6) Uniform
- 7) Exfoliation

Pitting corrosion occurs if there are low levels of chloride anions present in the electrolyte and the “pitting potential” is exceeded [76]. Pitting takes place as a galvanic reaction between alloying elements, meaning purer alloys are more resistant [77]. The standard for evaluation of pitting corrosion is ASTM G46-94 [78].

The mechanism of pitting of metal in a NaCl solution is illustrated in Figure 17.

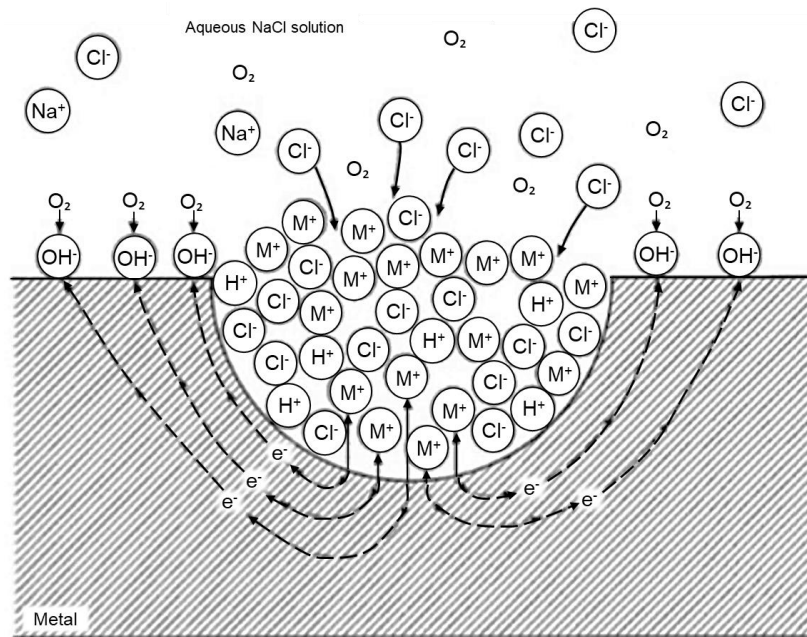


Figure 17: Pitting of metal in NaCl solution (Adapted from [79])

This mechanism can be broken down into four (4) parts. First, the metal is pitted in the NaCl solution (chloride anions) by the formation of metal ions at an anodic site, leading to local instability of the surface layer and environment. Second, there is rapid dissolution (metal oxidation) within the pit with oxygen reduction on the adjacent surface, making it a self-propagating process, and increasing the pH on the surface adjacent to the pit [79,80]. Thirdly, the metal ions' rapid dissolution creates excess positive charge in the pit, thereby relocating chloride ions into the pit. This leads to a higher metal chloride concentration in the pit along with hydrogen ions. With Al, the aluminium chloride film can stabilise the pit. Finally, the hydrogen and chloride ions increase metal/ alloy dissolution [79,80]. With Al, the aluminium chloride hydrolyses into aluminium hydroxide $\text{Al}(\text{OH})_3$, which decreases the pH again, increasing the corrosion rate [80]. When $\text{Al}(\text{OH})_3$ precipitates on the edges of the pit, it covers it and eventually slows down the corrosion progression by impeding ion exchange [80,81].

The presence of porosity in the metal can also negatively impact resistance to corrosion in these chloride environments [5] by acting as pre-existing pits for the solution to enter.

Galvanic corrosion occurs between aluminium electrolytically connected to another metal which is more cathodic [77].

Intergranular corrosion is described as a selective attack process on grain boundaries without necessarily attacking the actual grains [76]. These grain boundaries can be depleted or enriched with alloying elements [77].

Stress corrosion cracking (SCC) is one of the most serious types of corrosion, as it can cause sudden component failure if not identified promptly [76]. SCC mainly appears only as cracks, without visible corrosion product [77]. It requires a susceptible alloy, tensile stresses to open cracks and an aqueous environment [76].

Crevice corrosion needs a gap (crevice) to be present, such as an overlap of parts [76]. The crevice becomes devoid of oxygen, leading to dissolution of the aluminium and the formation of pits [77].

Uniform corrosion occurs in very high (alkaline) or low (acidic) pH solutions. In these environments, the aluminium oxide that forms is unstable, therefore less protective than usual [76].

Exfoliation corrosion is a risk during heavy deformation processes such as cold rolling, where the grains are flattened [76]. Exfoliation corrosion grows simultaneously through numerous grain boundaries that run parallel to the surface of the metal. The metal that remains behind between the corroded boundaries then separates like the pages of a book [77].

The different types of corrosion are shown schematically in Figure 18.

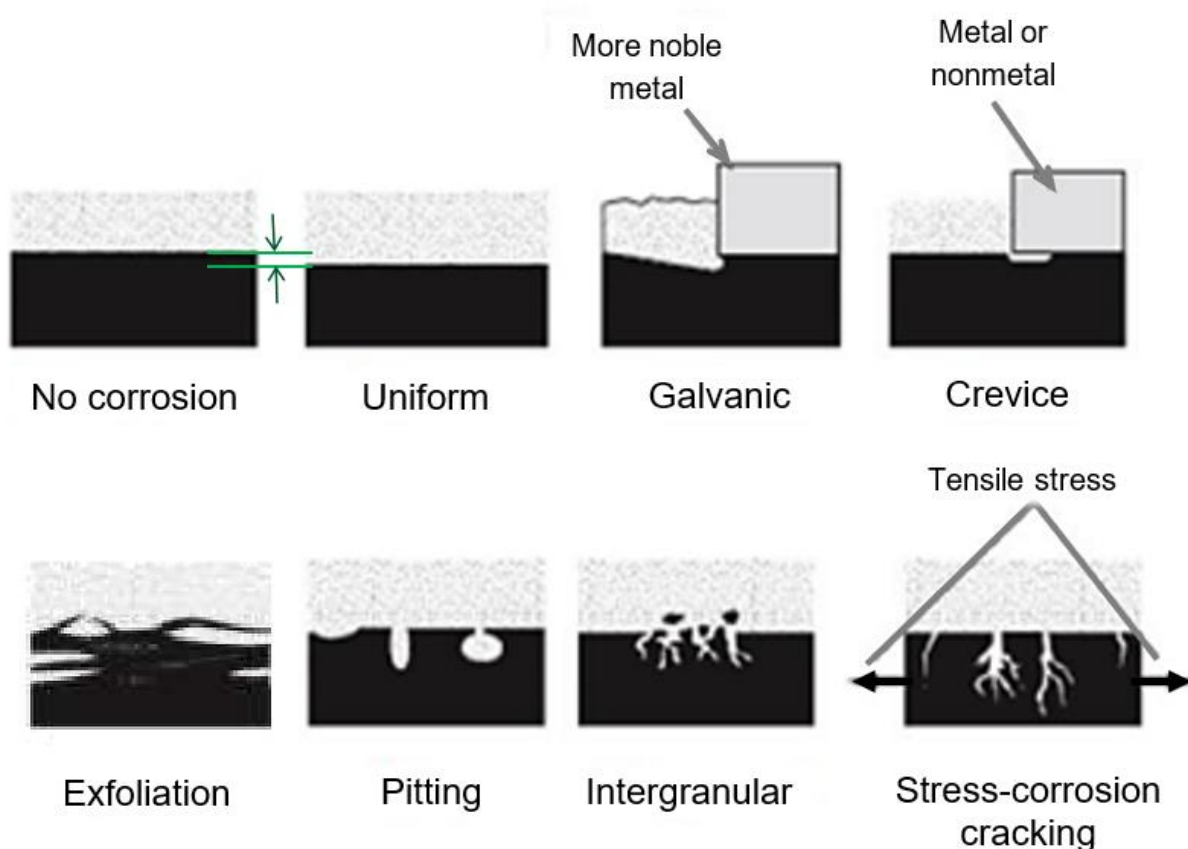


Figure 18: Types of corrosion (Adapted from [82])

Corrosion behaviour of AM Al-alloys has been described in previous studies [3,83]. Cabrini et. al. [3] investigated the behaviour of the heat-treated AlSi10Mg alloy by means of an intergranular corrosion test (only) according to the ISO 11846 standard [84].

Leon et. al. compared the AM Al-alloy with its cast counterpart, Al-A360, using an immersion test (ASTM G31-12a [85]) and a polarisation test. The pitting corrosion was evaluated using ASTM G46 [78]. The results showed that the AM alloy has slightly better corrosion resistance than the cast alloy due to its finer microstructure [83].

Despite its finer microstructure, the presence of intermetallics or second-phase particles can cause reduced corrosion resistance, as well as inferior mechanical properties [5].

8.1 Surface roughness effect on corrosion

A lower surface roughness can increase the corrosion resistance of L-PBF samples. This was evidenced in a study by Leon and Aghion [86] where polished and unpolished samples of AlSi10Mg were corroded in a 3.5% NaCl immersion for 30 days, and the corrosion rate and depth was measured.

The polished samples displayed a much higher resistance to the corrosion, as the rate and depth were both lower than for the unpolished samples. The unpolished sample, upon initial visual inspection, already revealed a lower resistance due to corrosion products and multiple pitting sites [86].

The cross-sectional views also displayed that the pits in the unpolished sample penetrated deeper and were more irregular in shape compared to the polished sample. The higher surface roughness, and therefore passive surface area around the pit, acted as a cathode, with the pit tip as the anode, and amplified the corrosion [86]. The NaCl solution acts as an electrolyte, and the internal pit arrangement in the unpolished samples allows for the possibility of electrolyte stagnation. This creates severe autocatalytic corrosion [86]. This concept is illustrated in Figure 19.



Figure 19: Anodic and cathodic reactions on single metal (Adapted from [87])

The cross-sectional views are shown in Figure 20.

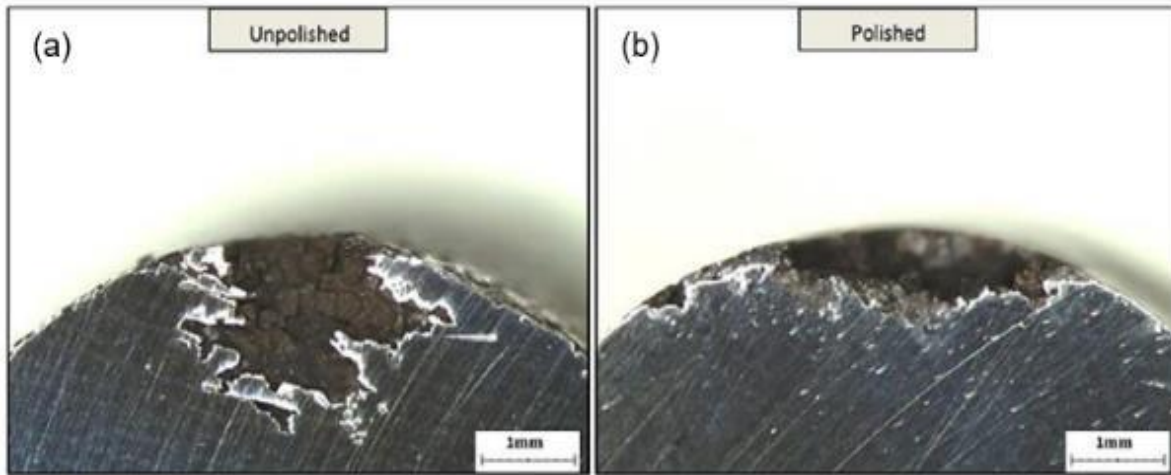


Figure 20: Cross-sectional views of pitting attack with (a) unpolished and (b) polished specimens after immersion test for L-PBF AlSi10Mg corroded in a 3.5% NaCl immersion for 30 days [86]

8.2 Porosity effect on corrosion

Porosity has been shown to influence corrosion of AM-AlSi10Mg [67,83,88,89]. As with a higher surface area, pores can act as preferential sites for the initiation of localised corrosion [67]. The study done by Leon et. al. [83] attributed the difference in corrosion behaviour to the porosity present in each sample, as well as the difference in microstructures. It was concluded that the AM alloy had a higher corrosion resistance due to less irregular pores being present than in the cast alloy. Despite the improved corrosion resistance, the authors felt that the porosity still had a negative impact on the AM alloy, as the corrosion progression followed the pores where the melt pool overlapped [83]. Another study has found that reducing porosity content from $1.56 \pm 0.84\%$ to $0.54 \pm 0.16\%$ noticeably decreased the amount of corrosion that took place [89].

8.3 Corrosion product

Metal corrosion is electrochemical in nature, where the anode is oxidised into a positive ion and released from the surface of the solid metal. For an aluminium alloy in an aqueous solution, the anode is the metal itself, the aqueous solution is the electrolyte and the cathodic reactions are reduction of hydrogen and oxygen. The reduction reactions are as follows [80]:



(where pH is ≥ 7)



(where pH is < 7)

The oxidised aluminium reaction is [80]:



These redox reactions lead to the formation of corrosion product, with the reaction as follows [80]:



This aluminium hydroxide forms as an insoluble, amorphous white gel [80].

For L-PBF AlSi10Mg in contact with an aqueous NaCl solution the redox reactions occur as follows for aluminium oxide formation [5]:



Oxygen that dissolves in the electrolyte (aqueous solution) can diffuse into the interface between the Al alloy and electrolyte can initiate another reduction reaction, leading to the formation of hydroxyl ions as in reaction [\(10\)](#).

This can contribute to the Al oxidation, allowing for the formation of either an aluminium oxide or hydroxide [5]:



These corrosion products ($Al(OH)_3$ and Al_2O_3) have a charge transfer that is higher than that of the Al substrate. This allows them to decrease the diffusion occurring in the anodic Al alloy region [5].

The stability of corrosion products is largely dependent on the pH scale of the environment it is in. Very high (alkaline) or low (acidic) pH environments lead to unstable film formations, such as with uniform corrosion. The corrosion/product stability is estimated using the Pourbaix diagram in Figure 21.

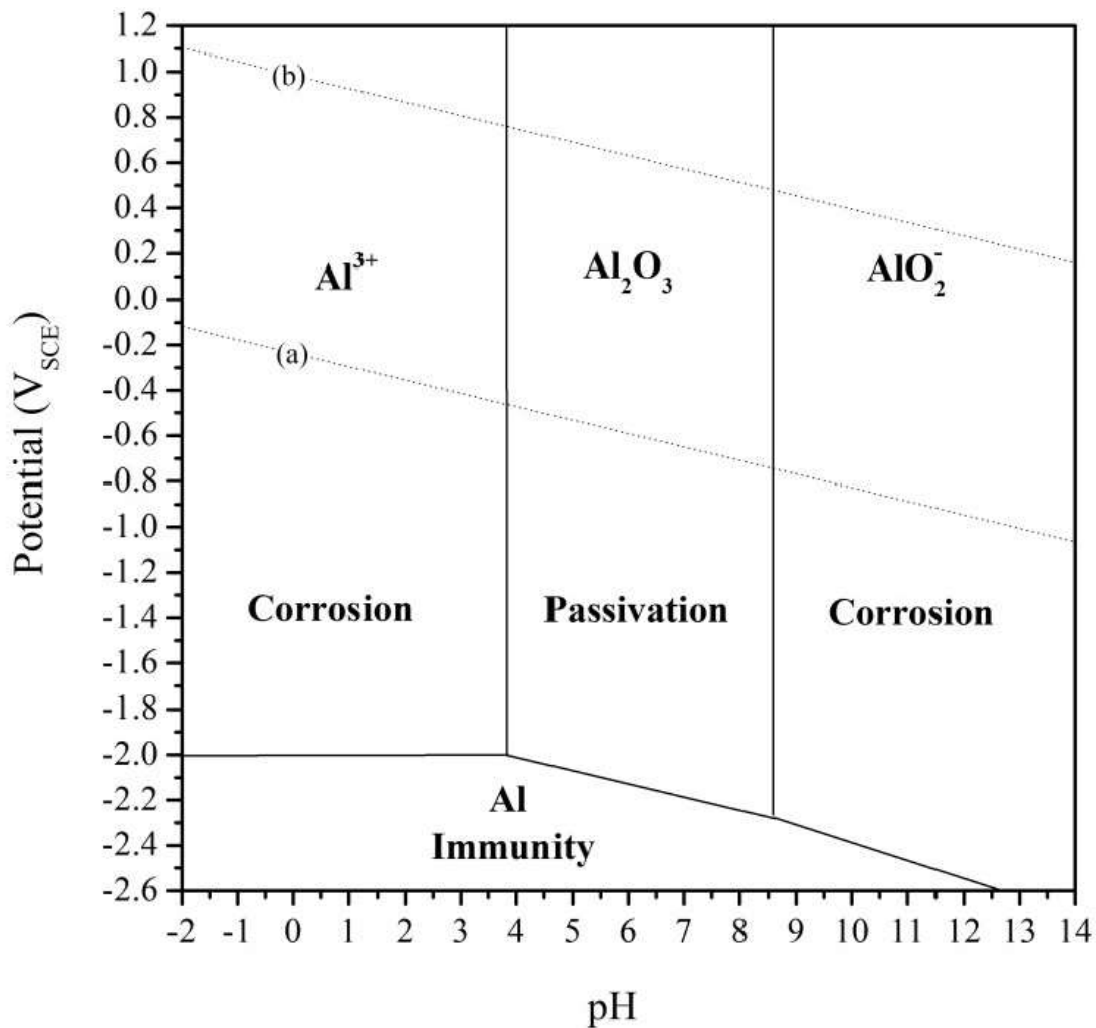


Figure 21: E-pH diagram for pure Al at 25 °C in aqueous solution [90]

It can be seen that in the pH range of approximately 4 to 9 there is less likely to be corrosion, but rather formation of a passive Al_2O_3 layer. However, as soon as alloying elements are added, or chloride anions are present, this estimation becomes more complex. A revised E-pH diagram is given in Figure 22. From this revised diagram it is clearly seen that localised corrosion is possible in the “passive” region.

Specifically pitting or uniform corrosion can occur in the pH range where passivation usually occurs, at both high and low potential (V_{SCE}) [90].

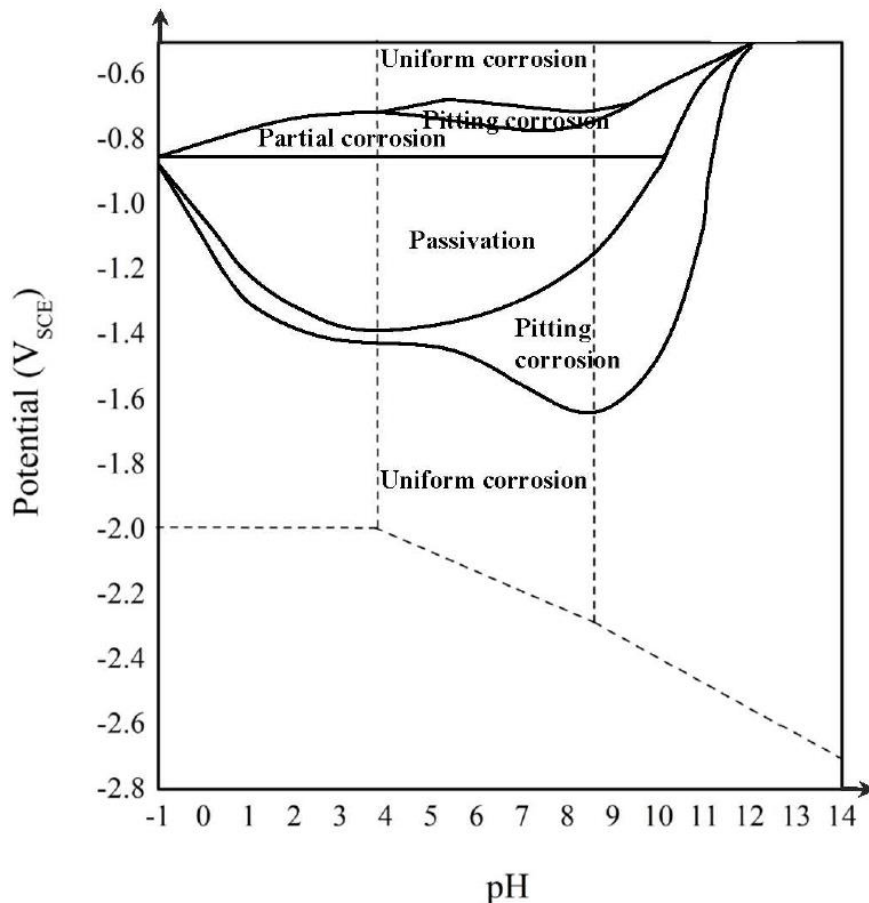


Figure 22: E-pH diagram with corrosion mode based on experimental data for AA5086 in 0.5M NaCl environment [90]

The corrosion product that forms during corrosion is therefore clearly also dependent on the elements present in the corrosive environment. The most common corrosion product that forms is the passive Al_2O_3 layer. However, this 'aluminium oxide' that forms is not always stable or passive [91]. One main advantage of aluminium hydroxides forming is that they are useful when coating or bonding the aluminium product, as the hydroxides can bond well with adhesives and lacquers. Too much hydroxide product, however, will lead to a destabilised surface layer which is also relatively hygroscopic [91].

Various oxide compounds have been detected as corrosion product for aluminium exposed to atmospheric elements. The first compound to form is usually aluminium oxide Al_2O_3 which is then covered by other oxide and hydroxide forms like Bayerite, $\text{Al}(\text{OH})_3 \cdot 3\text{H}_2\text{O}$, and including the hydrated variant tucanite, $\text{Al}(\text{OH})_3 \cdot \frac{1}{2}\text{H}_2\text{O}$, which has an amorphous structure [92]. Furthermore, the corrosion product that forms first contains a large amount of water, leading to the formation of the hydrated amorphous compounds. This aluminium oxide/ hydroxide is a white gel that can cover the corrosion pits. When the water has evaporated the compound looks more like a white powder [93].

Secondary reactions can also create various corrosion products that remain amorphous at room temperature, regardless of the corrosion type that initiated the formation. An important note is the high volume ratio of corrosion product to corroded metal, $\text{Al}(\text{OH})_3 \cdot n\text{H}_2\text{O}/\text{Al}$, to the order of 6.5 [93].

8.4 Review studies on Al corrosion

The corrosion behaviour of components produced by AM still requires in-depth study, in terms of environmental interaction, which can impact both the integrity as well as the performance of the components. Welding process development in recent years has indicated that AM metallic parts experience corrosion based on variations in microstructure and inherent differences caused by the additive manufacturing processes [94].

Therefore, it can be hypothesized that corrosion susceptibility will also be affected by any aspects that affect or induce microstructural changes and defects in the component material [94].

A review by Berlanga-Labari et. al. [94] has compiled the results from other reviews regarding Al AM corrosion. One result noted that features associated with some AM processes can create potential nucleation sites for corrosion, including grain direction, porosity, segregation of the solutes, dislocation networks, surface roughness, oxides and residual stresses. Another noted the molten pool boundary (MPB) effect, inherent to some AM processes, implying the presence of thermal stresses and segregation of the chemical elements, as well as non-equilibrium phases at the MPB, which affects corrosion behaviour. Additional processing, such as treating the surface, may be required to minimise corrosion risk. These treatments include anodising, coating and plasma electrolytic oxidation (PEO) [94].

Another conclusion was that annealing lowered the AM parts' corrosion resistance due to microstructural coarsening. The modification of Al-alloys with scandium (Sc) was shown to decrease corrosion susceptibility in an electrochemical environment in the AM part even more than in a cast alloy. This is due to the absence of active cathodic and anodic surfaces. The grain boundaries are also modified by laser melting to minimise or even eliminate dissolution of the aluminium-scandium precipitate (Al_3Sc), thereby improving corrosion resistance [94].

The silicon particles form a continuous network in the as-printed part, and are distributed uniformly in the Al-matrix, guaranteeing low corrosion current density during potentiodynamic testing. However, they are transformed into isolated particles during annealing or heat treatment, creating connectivity loss between particles of Si, which creates localised areas of lower corrosion resistance. Their density will also decrease as the annealing temperature is increased, causing a decrease in fretting wear resistance [94]. Melt pool boundaries (MPB) with a higher Si content can cause a thinner passive oxide layer to form locally, as high density MPBs negatively affect the passive layer's uniformity. This non-uniformity and Si-phase enrichment along MPBs will decrease the propensity for a thicker passive layer to form [5,89].

There was a general consensus that AM parts have higher corrosion resistance than the cast Al counterparts, with similar surface finishes, due to the finer microstructure. Laser melting further improves resistance through the formation of a thick, stable and dense passive oxide film. It was also noted that uniform pitting distribution was experienced in the early immersion stages of heat treated AM-AlSi10Mg alloys.

It was concluded that the passive layer was more protective during the initial immersion period, with localised attacks near the Si particles that coarsened during heat treatment. The heat treatment also caused a potential difference between the Al matrix and coarse Si galvanic couple [94].

Another result further explained that the charge transfer resistance of the samples was higher than the passive/corrosion layer resistance. This confirmed that initially the behaviour of the corrosion was controlled by uniform corrosion with metastable surface pitting. As the passive layer is more compact and stable, faster rates of cooling and solidification limit aluminium dendrite and Si precipitate coarsening, decreasing potential differences between them in that area and decreasing susceptibility to pitting or selective attacks. AlSi10Mg has experienced selective penetration, as a region of non-equilibrium, due to the Si particles that are isolated and then segregated in MPBs. The lower potential difference also decreases the susceptibility of intergranular corrosion, although the addition of Mg is also said to decrease intergranular corrosion [94].

Salt spray corrosion testing usually results in pitting corrosion, due to the presence of chlorides in solution. However, some corrosion product is also formed. One result used energy dispersive spectroscopy (EDS) analysis to identify the product as Al₂O₃ on the surface and Al₂O₃ with MgCl₂ inside the pits [94]. Table 9 shows a summary of different corrosion tests and their relationship to specific detection techniques.

Table 9: Corrosion tests and detection techniques (Adapted from [94])

Al-alloy & manufacturing process	Corrosion Test	Solution	Detection Technique	Corrosion Type
L-PBF-AISi10Mg	Immersion / Potentiodynamic	3.5% NaCl	OM, SEM-EDS	Pitting / Fatigue
L-PBF-AISi10Mg	Salt fog / Potentiodynamic	1 M NaCl	SEM-EDS, SEI, BEI	Pitting / Uniform
L-PBF-AISi10Mg	Immersion / Potentiodynamic	3.5% NaCl	OM, SEM-EDS	Pitting / Exfoliation
L-PBF-AISi10Mg	EIS / Potentiodynamic	--	SEM	Preferential and selective

Where:

OM = Optical microscopy

SEI = Secondary electron imaging

BEI = Back-scattered electron imaging

EIS = Electrochemical Impedance Spectroscopy

EDS = Energy Dispersive Spectroscopy

From Table 9 it is seen that potentiodynamic testing with different concentrations of sodium chloride solutions is often employed to check for susceptibility for corrosion. This is then usually identified using SEM and EDS techniques [94].

9. Lattice structures

Lattice structures are porous cellular designs with complex architectures allowing unique properties such as low mass and high surface areas, with applications in medical and aerospace industries [95].

L-PBF is uniquely suited to manufacture thin wall structures such as lattices, as it has the ability to produce consolidated complex geometries [1].

Commercially available software packages can be utilised to create a practical cellular material design for use in engineering applications [95]. An in-depth study was done on lattice design in [96] with focus on designs to improve the fatigue performance.

9.1 Types of lattices

Examples of different types of unit cells are illustrated in Figure 23, with Figure 23(a) showing four designs based on struts and Figure 23(b) four designs based on a minimal surfaces. They all share the same overall density, but have differences in pore size and minimum feature thickness due to the differences in design [95].


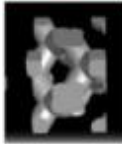


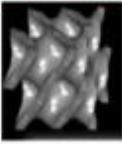



(a) Strut-based design				(b) Minimal surface design			
Rhombic dodecahedron	Diamond	G-struct	Octet	Diamond	Gyroid	I-WP	Primitive
							
R-sb	D-sb	G-sb	O-sb	D-ms	G-ms	I-ms	P-ms
Porosity, %							
63	61	63	62	62	63	65	62
Strut/Sheet thickness, μm							
332	491	651	288	157	188	152	250

Figure 23: Different types of unit cells for lattice designs using (a) strut - based design and (b) minimal surface design [95]

Figure 24 shows the corresponding lattice structures that are created by repeating the unit cell designs in each direction. Figure 24(a) illustrates the strut-based lattice designs and Figure 24(b) depicts the minimal surface based designs.

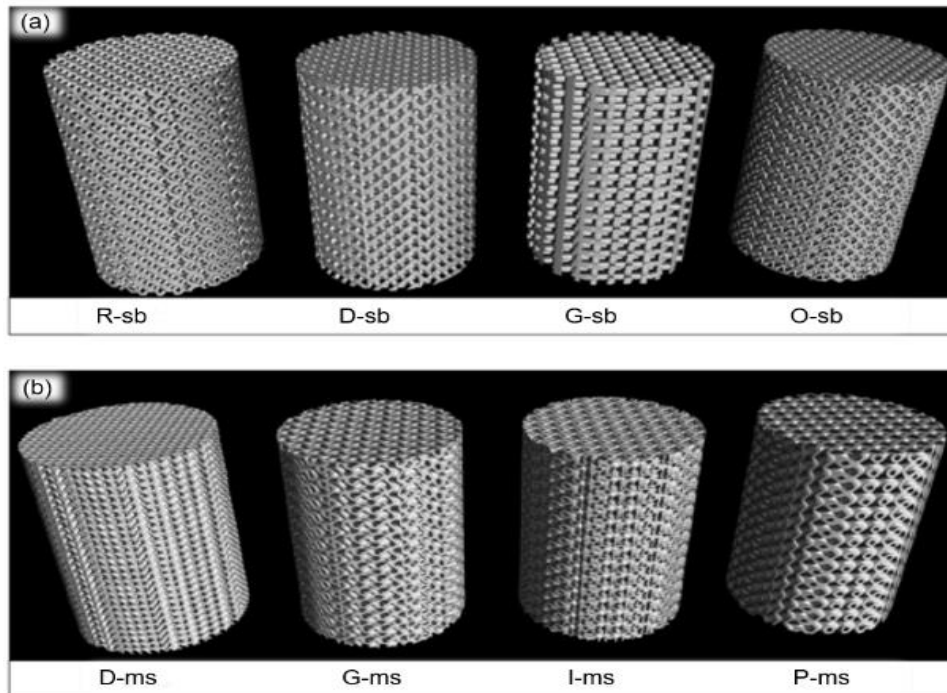


Figure 24: Corresponding repeated lattice structures for (a) strut-based design and (b) minimal surface design [95]

Each lattice design in Figure 24 has the same overall density, and include a minimum of ten unit cells in the X, Y and Z directions [95].

Minimal surface designs are based on sheets that are usually self-supporting, with the curvature at each surface point having a zero average. This allows the stresses to be more evenly distributed [95].

9.2 Design considerations

When designing a lattice structure, various aspects need to be considered. The first is the unit cell design. The unit cell is defined as being the smallest element which characterises the entire lattice. Three methods are used to design the unit cell, namely the primitive-based, implicit surface based and topology optimisation methods. The primitive based method uses primitive geometrics to construct the unit cell, the implicit surface uses mathematical equations to define the cell's surface and the topology optimisation obtains cell geometry through calculations that focus on optimising the topology [97].

Another aspect in lattice design consideration is the mechanical behaviour. The properties of the material itself combined with the lattice properties and amount of porosity will affect the yield strength and elastic modulus as well as the ductility. These material properties are also affected by the lattice density and design. When a properly designed lattice replaces a solid interior, the properties can be tailored to the application but never exceeds the basic properties of solid [97].

When the designs are strut-based, the Maxwell criterion can be used to classify whether the design is stretch- or bending-dominated. The equation for the Maxwell criterion M is shown in Equation 13 [95]:

$$M = b - 3j + 6$$

Equation 13

Where b is the number of struts and j is the number of joints.

When $M < 0$ the structure is bending-dominated,
 When $M \approx 0$ the structure is stretch-dominated and
 When $M > 0$ the structure is over-rigid

The criterion is applied to simple strut-based structures only [95]. If the struts are bending-dominated it means they will bend under lattice compression which will result in shear failure. Stretch-dominated struts will fail in a layer-by-layer manner as they are stiffer [95]. The struts are classified schematically in Figure 25(a) and examples are shown in Figure 25(b).

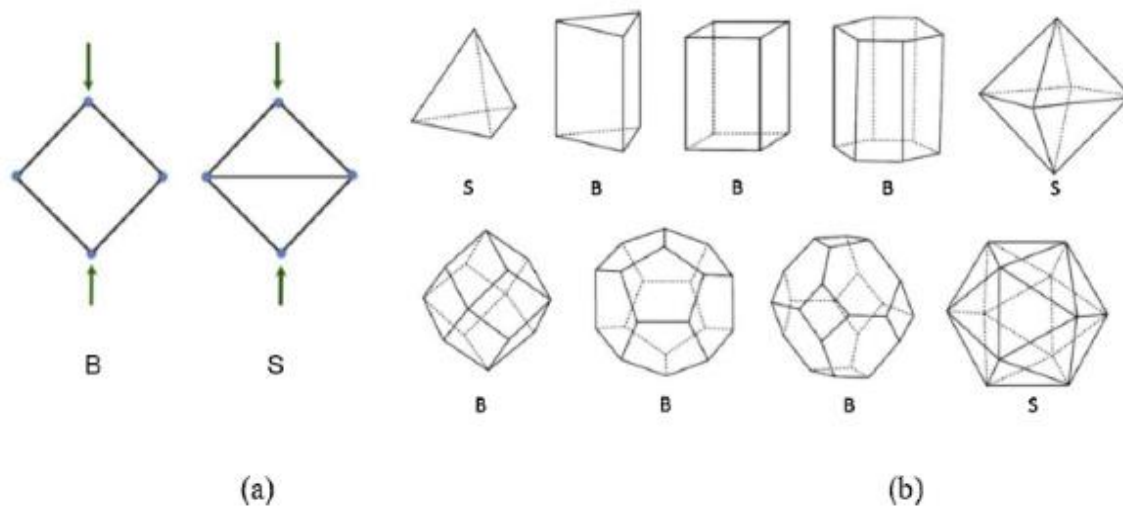


Figure 25: (a) Bend *B* or Stretch *S* dominated classification and (b) examples [95]

Lattice structures can experience a unique mechanical response. Initially, it follows the typical linear elastic response up to the point where it yields (either fails or buckles), followed by either a plateau or repeated yield and recovery cycles (for layer-by-layer-failure) and ending with the final densification [95]. This is illustrated in Figure 26.

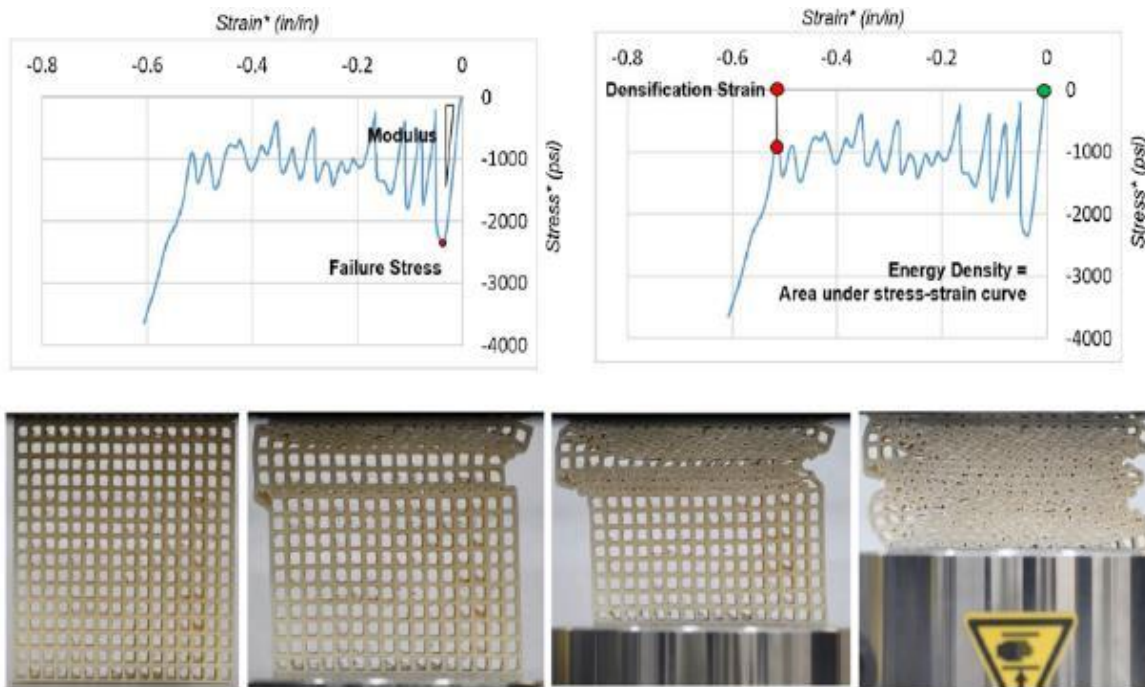


Figure 26: Effective stress-strain plots from compression of a square honeycomb, indicating effective modulus, failure stress, densification strain and energy density [95]

If the lattice structure has a sufficient number (typically more than six) of unit cells in the X, Y and Z directions, it can be treated as an open-cell foam instead of a solid structure [95].

The linear response area relates the structure density as well as the bulk elastic modulus to the effective elastic modulus of the lattice using Equation 14 [95]:

$$E = \alpha_2 \times E_{\text{solid}} \times \left[\frac{\rho}{\rho_{\text{solid}}} \right]^2 \quad \text{Equation 14}$$

Where E is the effective elastic modulus, α_2 is a constant, E_{solid} is the bulk elastic modulus, ρ is the density of the lattice structure and ρ_{solid} is the density of the solid. The constant α_2 is dependent on material properties as well as accuracy of manufacturing. It can vary from 0.1 to 4, but stays constant for each specific process and material [95].

This equation shows that density on its own can control the effective elastic modulus. This implies that as long as the overall filled space has a minimum of six unit cells in the X, Y and Z directions, a unit cell design with 50% density can utilise any size of unit cell for the lattice and the material stiffness will remain the same. The exponent “2” is used in ideal bending-dominated lattices, whereas an exponent “1” would be used for ideal stretch-dominated lattices [95].

Finally, the third aspect to consider is the manufacturing limits. Up to a certain horizontal strut length, strut-based designs can be printed without support [95]. On the other hand, sheet-based designs like the minimal surfaces can usually print without any supports needed. This means the manufacturing limits also constrain the possibilities in design [95].

The limits that play the largest role are minimum feature size and the employed contour and hatch scanning strategy. Minimum feature size, in turn, is also limited by the size of both the laser spot and powder, as well as the slicing accuracy of the 3D model [95].

CHAPTER III: MATERIALS & METHODS

1. Materials

AlSi10Mg samples were used in this project. They were manufactured at the Royal Melbourne Institute of Technology (RMIT) University in Melbourne, Australia. A SLM500 Quad laser system, manufactured by SLM Solutions (SLM refers to Selective Laser Melting, another term for L-PBF), was used to produce 25 solid cubes, with dimensions 10 x 10 x 10 mm³, as well as 25 lattice cubes, with dimensions of 16 x 16 x 16 mm³. The powder feedstock material composition is described by Maconachie et. al. in [98], and shown in Table 10.

Table 10: Composition of the AlSi10Mg powder before L-PBF [98]

Al	Si	Cu	Fe	Mg	Zn	Cr	Ni	Mn	Ti	V	N	O
Bal.	10.2	<0.01	0.19	0.34	0.01	0.01	0.01	<0.01	0.01	0.005	0.002	0.12

The particle size distribution of the powder is shown in the graph in Figure 27.

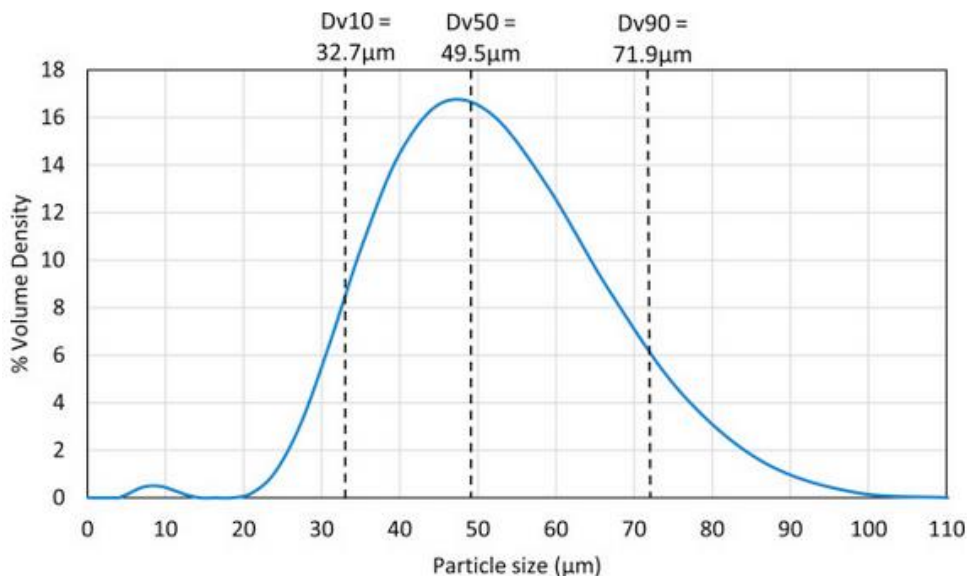


Figure 27: Particle size distribution chart [98]

Five (5) different laser power settings were used to artificially induce different porosity contents, with five samples produced at 210, 280, 350, 420 and 490 W each.

Table 11: Parameters used in this L-PBF process

Parameter	Value
Layer thickness (µm)	50
Laser velocity (mm/s)	921
Hatch spacing (µm)	190
Scan strategy	One contour scan followed by hatch tracks in zigzag pattern with 90 degree change per layer.

A photo of the solid cube samples is shown in Figure 28. Each sample has pins on the top surface to aid in identifying them. The pins on the left of the samples in the image refer to the laser power used to produce the samples. The pins on the right indicate the number of the sample in its respective laser power set. To ensure the correct sample is used, the identification is done by making sure that the gap (indicated by the small yellow boxes) on each sample is on the same side, i.e. both top or bottom. This helps to avoid confusion between E3X5 and E5X3 for example.

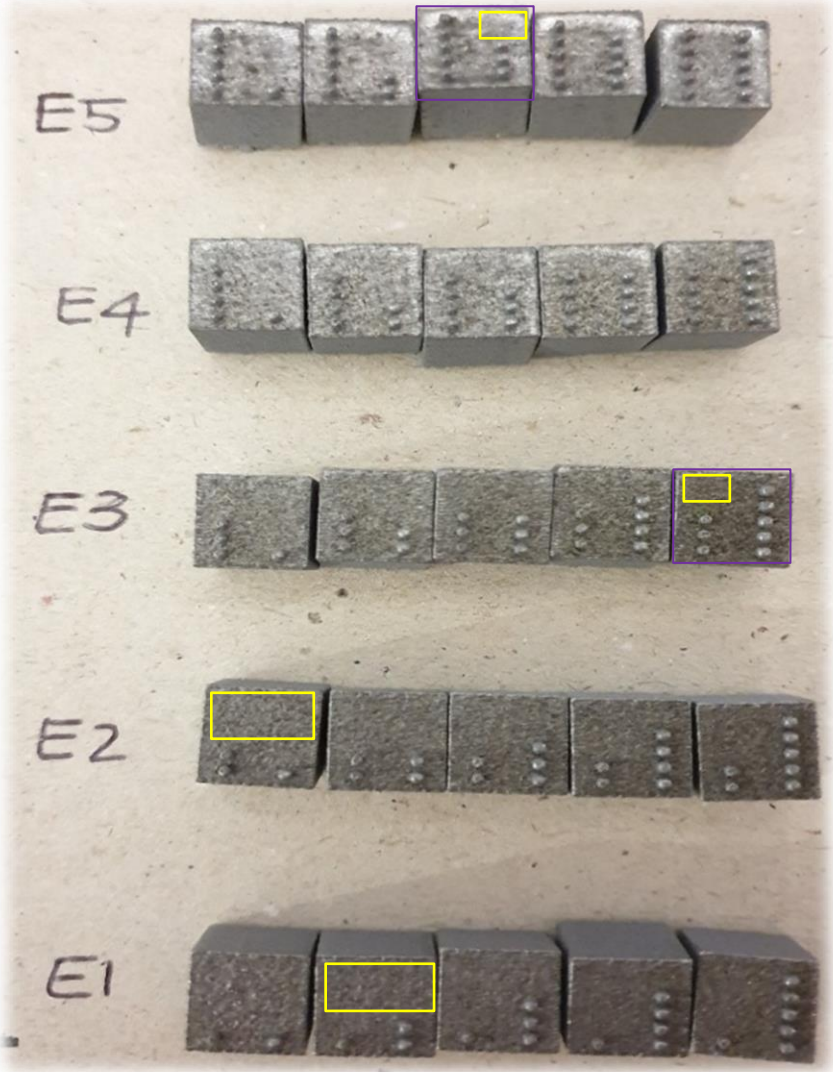


Figure 28: AISi10Mg solid cube samples, with E1 as the lowest laser power and E5 as the highest laser power [99]

One sample of each laser power for the lattice samples are shown in Figure 29. They were marked on the side using the same numbering convention as the identifier pins for the solid cubes, to help with identifying them.

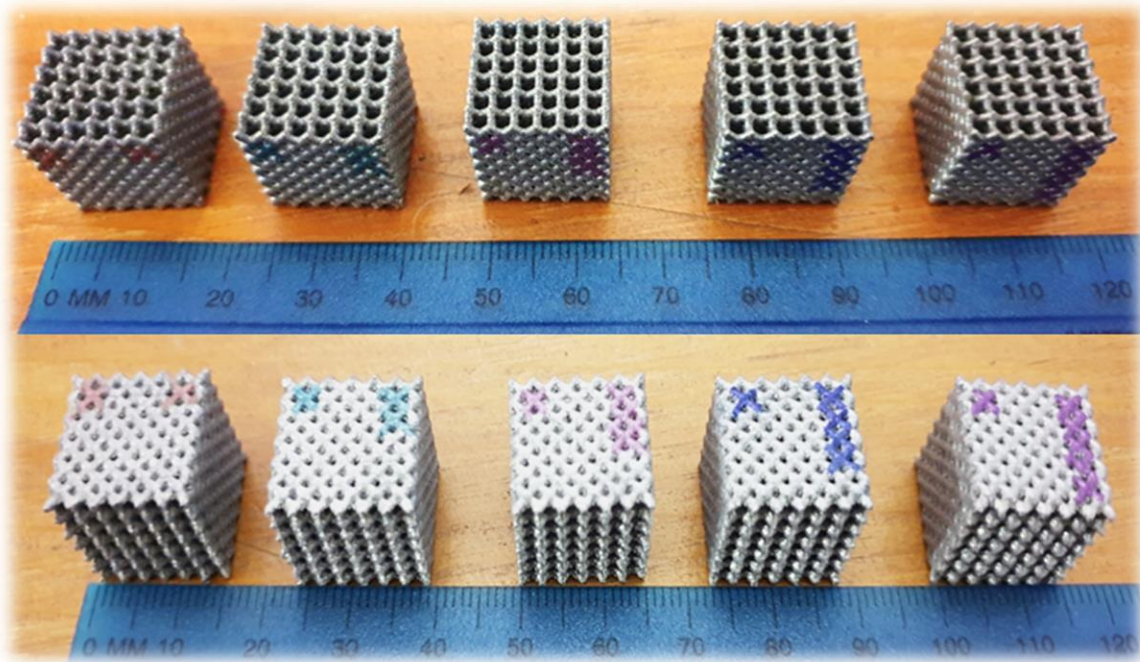


Figure 29: AISi10Mg lattice cube samples, with E1 to E5 from left to right [99]

The plans for all of the samples are shown in a grid in Figure 30 for the solid cubes, and Figure 31 for the lattice cubes, where E_n refers to the different laser powers and X_n refers to the number of the sample in each laser power set. For the solid cubes it is noted that one sample from each laser power set is kept separate for microstructural evaluation.

	X1	X2	X3	X4	X5
E1	Microstructural examination	NSS 24 hours AASS 168 hours	NSS 72 hours AASS 120 hours + microstructure	NSS 120 hours	NSS 168 hours
E2	Microstructural examination	NSS 24 hours AASS 168 hours	NSS 72 hours AASS 120 hours	NSS 120 hours	NSS 168 hours
E3	Microstructural examination	NSS 24 hours AASS 168 hours	NSS 72 hours AASS 120 hours	NSS 120 hours	NSS 168 hours
E4	Microstructural examination	NSS 24 hours AASS 168 hours	NSS 72 hours AASS 120 hours + microstructure	NSS 120 hours	NSS 168 hours
E5	Microstructural examination	NSS 24 hours AASS 168 hours	NSS 72 hours AASS 120 hours	NSS 120 hours	NSS 168 hours

Figure 30: Plans for the solid cube samples for Neutral Salt Spray (NSS) and Acetic Acid Salt Spray (AASS)

For the lattice cubes in Figure 31 it is noted that one sample from each laser power set is kept separate for compression testing before corrosion.

	X1	X2	X3	X4	X5
E1	Before corrosion compression	NSS 24 hours AASS 168 hours + compression	NSS 72 hours AASS 120 hours	NSS 120 hours	NSS 168 hours + compression
E2	Before corrosion compression	NSS 24 hours AASS 168 hours + compression	NSS 72 hours AASS 120 hours	NSS 120 hours	NSS 168 hours + compression
E3	Before corrosion compression	NSS 24 hours AASS 168 hours + compression	NSS 72 hours AASS 120 hours	NSS 120 hours	NSS 168 hours + compression
E4	Before corrosion compression	NSS 24 hours AASS 168 hours + compression	NSS 72 hours AASS 120 hours	NSS 120 hours	NSS 168 hours + compression
E5	Before corrosion compression	NSS 24 hours AASS 168 hours + compression	NSS 72 hours AASS 120 hours	NSS 120 hours	NSS 168 hours + compression

Figure 31: Plans for the lattice cube samples for Neutral Salt Spray (NSS) and Acetic Acid Salt Spray (AASS)

2. Dimensions and Mass

Initial testing involved determining the dimensional accuracy of the samples and measuring the mass. Dimensional accuracy was carried out using a Vernier Caliper.

The mass was measured using a New Classic ML Mettler Toledo scale, which is accurate up to four (4) decimal places. It also has a draft shield to improve accuracy [100].

The scale was used for both mass in air (m_a) and mass in water (m_L) measurements. An average of three to four individual measurements were used. These values were also used in the subsequent density calculations.

3. Density measurements

The three methods used to determine bulk sample density (average density) were Archimedes, gas pycnometry and a CT-based density method described in detail in [101].

3.1 Archimedes

Archimedes density was measured using the same scale described in Chapter III: Section 2. “Dimensions and [Mass](#)”, along with distilled water to minimise air bubbles. The setup illustration is shown in Figure 32.

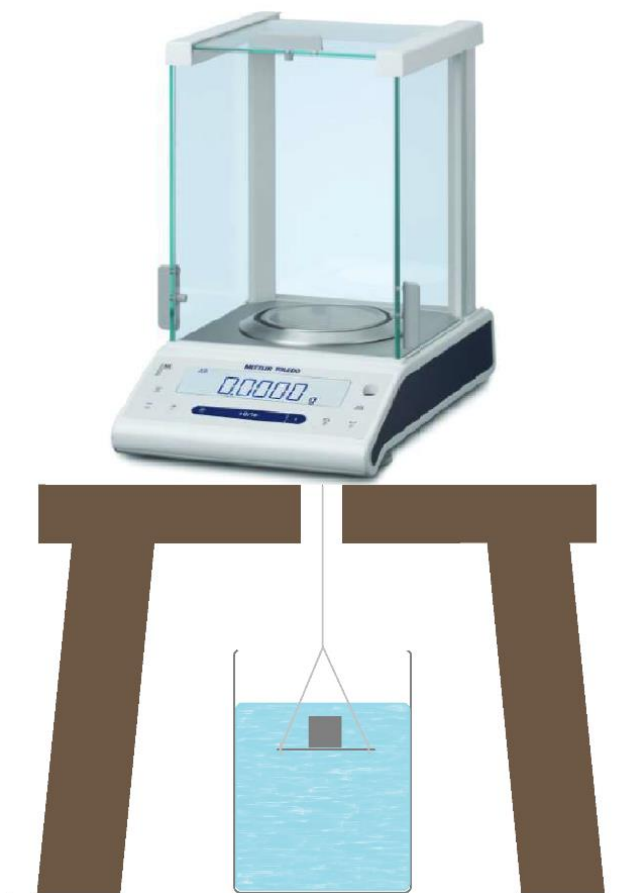


Figure 32: Archimedes setup sketch (Scale from [100])

The temperature of the water was also measured to ensure the correct water density (ρ_L) was used in the calculations. The density was calculated according to Equation [3](#). This was done for the solid and lattice cubes.

3.2 Gas pycnometry

The system used here was a Micromeritics AccuPyc II 1340 Gas Pycnometer with helium (He) gas at a calibrated pressure of approximately 19.5 psig, which is 134.45 kPa. The results give five volume measurements per sample, and the average of those were used to calculate density. The pycnometer is shown with calibration standards in Figure 33.



Figure 33: Gas pycnometer and calibration standards [99]

Both solid and lattice cubes were measured.

3.3 CT-based method

The density calculations of the CT-based method were based on mass in air of the samples, taken at the CT facility in Stellenbosch, and the CT-determined volume of each cube. The cubes were carefully segmented to include all pore spaces.

4. Surface roughness

The method used in this project to determine surface roughness was optical microscopy. It was carried out at Wirsam Scientific in Johannesburg using an Olympus DSX 510. The microscope uses the Olympus Stream software to create a surface topography map of each sample, and this data is used to calculate surface roughness values such as S_a and S_z . A three-dimensional (3D) colour scale map of the surface is also generated where the dips and peaks can clearly be seen. The microscope is shown in Figure 34, with a close up of a solid cube sample under the eyepiece.

Surface roughness was measured over a minimum of three $1\,960\ \mu\text{m} \times 1\,960\ \mu\text{m}$ separate areas on the top surface as well as the side surfaces, to obtain overall representative averages for the top and sides. The pitch (distance between each layer scanned) was $12.1\ \mu\text{m}$, whereas the height range scanned differed between samples due to different surface conditions.

The top surface is the final layer of the L-PBF process, as such it is likely to be the most affected by the process parameters. The bottom surface was excluded as it was not representative of the parameters, due to the samples being manufactured on supports which lead to an irregular surface. The side surfaces were also analysed to obtain a general idea of the side surface roughness, and how they differ from the top.

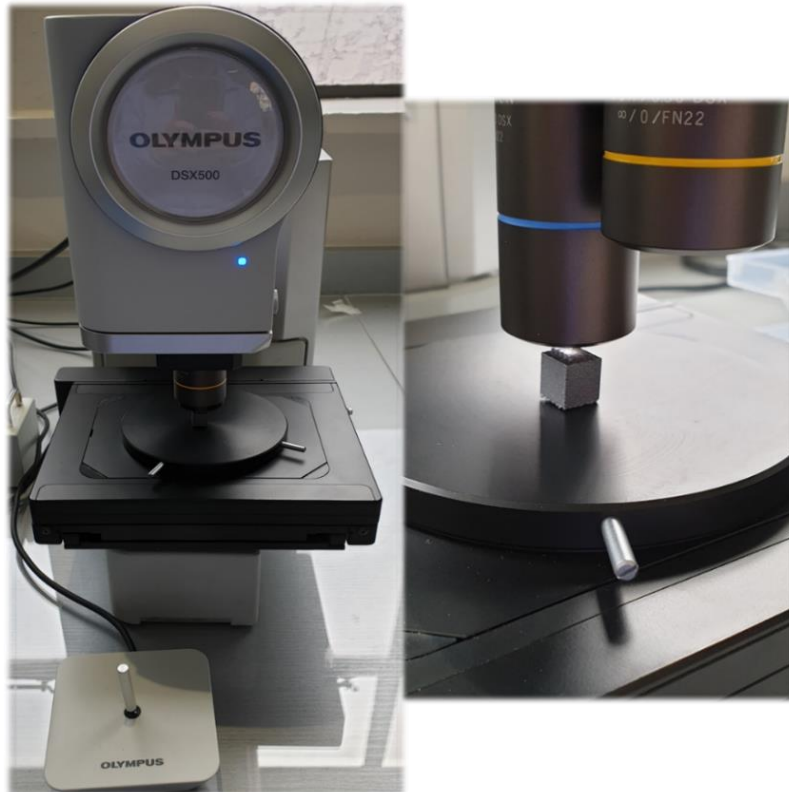


Figure 34: Olympus DSX 510 with close-up of sample under eyepiece [99]

This was only done for the solid cubes.

5. Metallographical examination

Selected samples were cross-sectioned for metallographical examination. One sample from each laser power set was cross-sectioned according to the illustration in Figure 35. This allowed for each of the YZ-, XZ- and XY-planes to be exposed for examination. This was only done for the solid cubes.

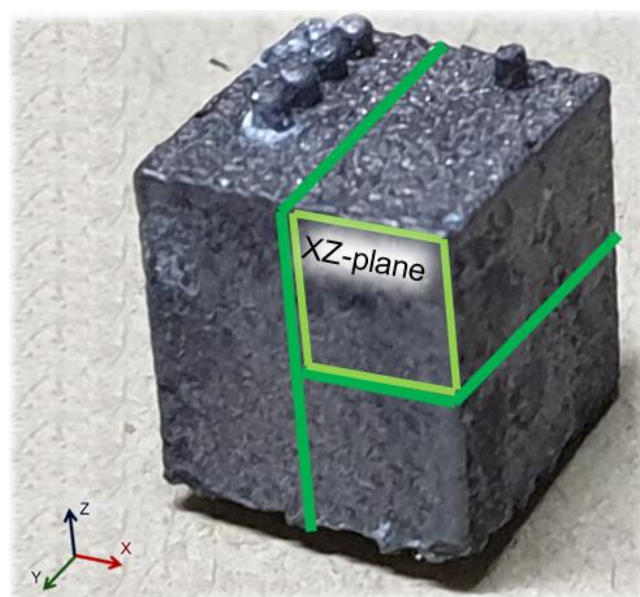


Figure 35: Cross-sectioning of the solid cube [99]

The cross-sectioning was done using an ATA Brilliant 220 cutting machine. The cutting was done with a diamond blade, as the samples are small, to minimise material loss during the cutting process. The cut samples were then mounted using an ATA Opal 410 Mounting press, with black bakelite hot mounting resin from Struers.

After mounting, each sample underwent grinding and polishing. The grinding started at 220-grit. This was followed by 400, 500, 800, 1200 and finished with 4000-grit. Polishing was done using first 3 μm and then 1 μm diamond paste and finished with colloidal silica.

The samples were then etched using a solution of 0.1% hydrofluoric acid (HF) with distilled water to enhance the microstructure. The material safety data sheet (MSDS) for hydrofluoric acid (HF) was consulted prior to etching, and in accordance the etching was carried out in a fume cabinet while wearing rubber gloves and using tongs to hold the sample in the etchant.

The cross-sectional surfaces were examined using optical microscopy, using both a Zeiss AXIO Imager and later a Nikon Eclipse ME600. The Zeiss AXIO Imager.A1m is shown in Figure 36(a) and the Nikon Eclipse ME600 in Figure 36(b).

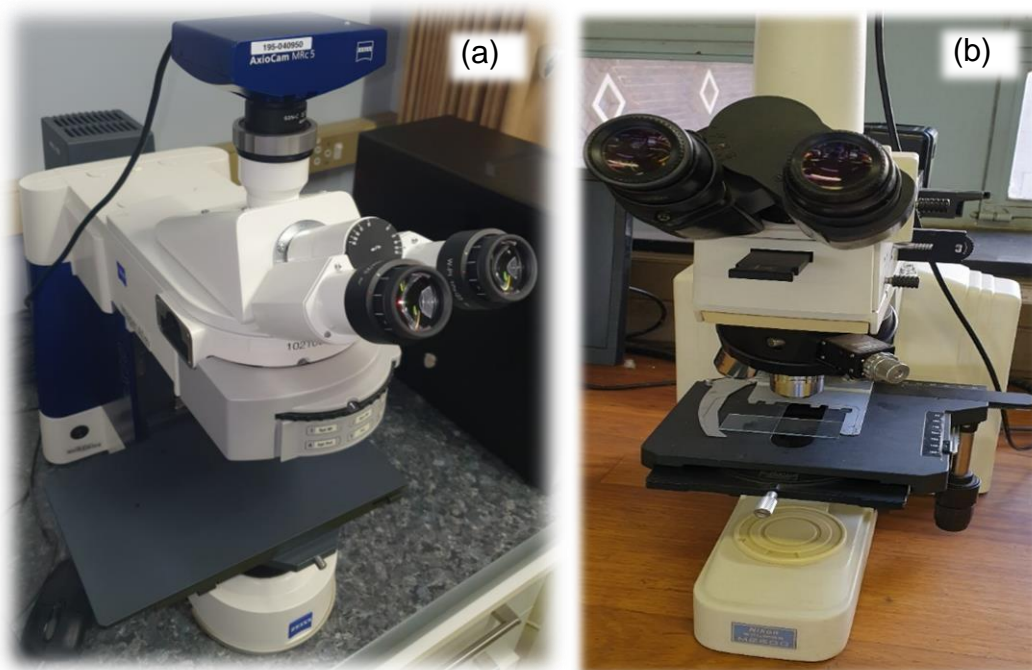


Figure 36: (a) Zeiss AXIO Imager light optical microscope and (b) Nikon Eclipse ME600 light optical microscope [99]

After optical microscopy, the samples were also examined using scanning electron microscopy (SEM). The ZEISS 540 Ultra Plus FEGSEM in Figure 37(a) was used for microstructural analysis. Also as part of the metallographical examination, the elemental composition was confirmed with SEM-EDS, using the JEOL JSM IT300LV. The JEOL SEM is shown in Figure 37(b).

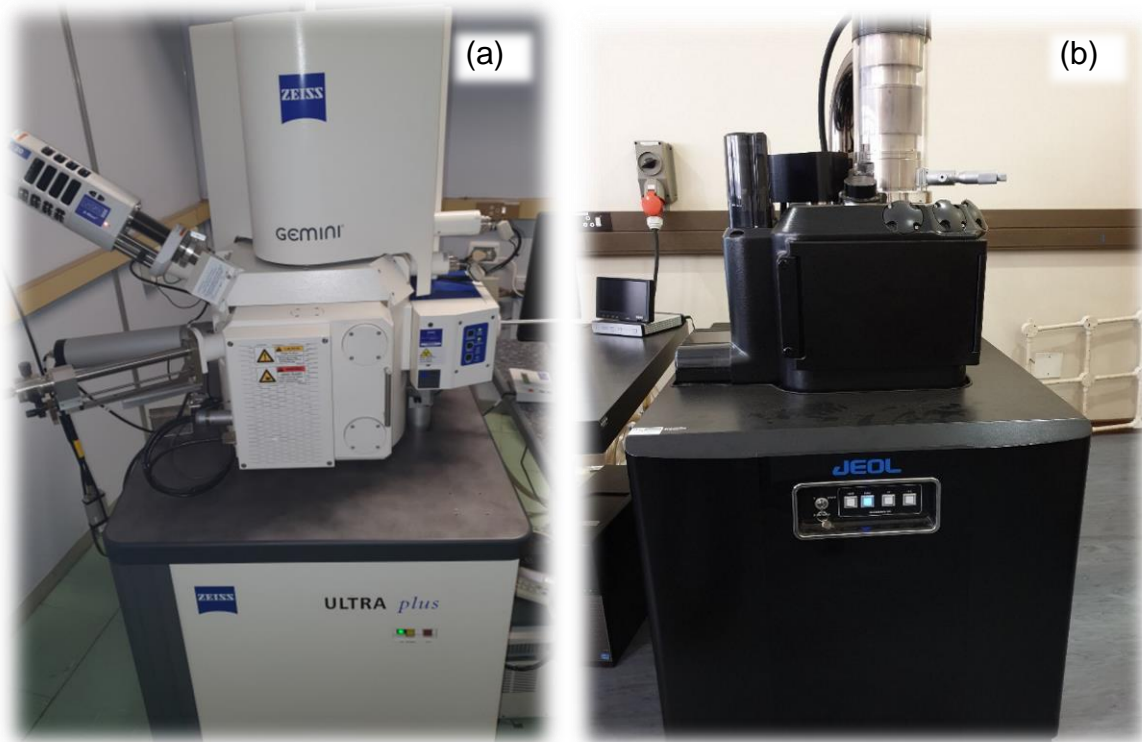


Figure 37: (a) Zeiss 540 Ultra Plus FEGSEM and (b) JEOL JSM IT300LV [99]

The final step was to conduct Vickers Hardness tests on the mounted samples, as differences in hardness correlate with differences in microstructure. The tester used is similar to the one in Figure 38.

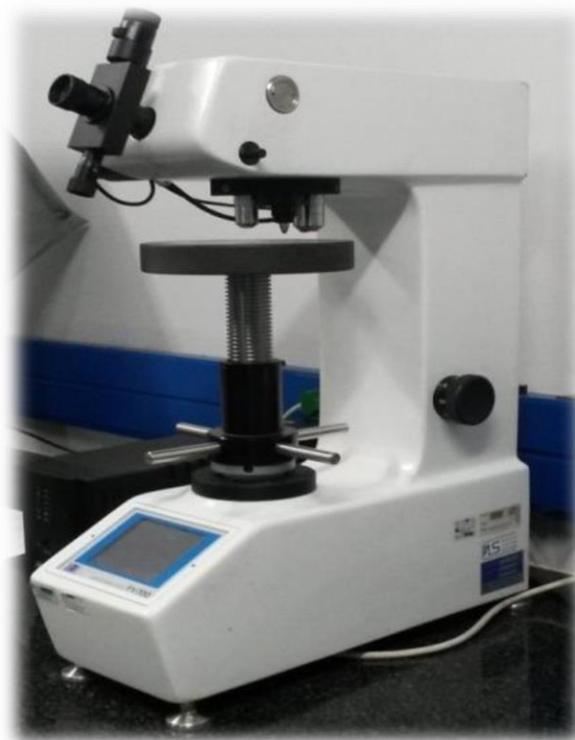


Figure 38: Vickers Macrohardness tester [102]

The loads used were dependent on the amount of porosity present, as higher loads were more likely to strike pores during the indentation. In order to obtain an accurate, representative value of the hardness of the solid samples, it is important to avoid pores.

Three loads were used, with 3 kgf (29.420 N) for the two lowest laser powers (E1 and E2), 1 kgf (9.807 N) for the middle laser power (E3) as well as second highest laser power (E4) and 0.5 kgf (4.903 N) for the two highest laser powers (E4 and E5).

6. Porosity

To investigate the porosity content, optical microscopy and SEM were used for planar views and NanoCT (X-Ray nano-tomography) scanning for the in-depth, three-dimensional view. The SEM from Figure 37(a) was used to obtain another view of the different pores.

6.1 NanoCT scan porosity measurement

Du Plessis et. al. reviewed and discussed the use of X-ray tomography in additive manufacturing in detail in [103]. The NanoCT scanning used a GE nanotom S system, set to 120 kV and 90 μ A for X-ray generation, and a voxel size of 10 μ m. The equipment used at the Stellenbosch CT facility is fully outlined in [104]. Visualisation and analysis of the scans was performed using Volume Graphics VGSTUDIO MAX software (Version 3.4) to determine the pore distribution and location.

The full porosity analysis procedure used is outlined by du Plessis et. al. in [105], with an image analysis workflow identical to one used in a previous study which looked at the effect of hot isostatic pressing (HIP) on porosity content for Ti6Al4V cubes [106]. This process involved a de-noising filter, followed by surface determination using an advanced function. This allows for sub-voxel precision, which means interpolation of the best threshold between the air and the metal. This was locally optimised to the grey values at each location.

7. Compression testing

Compression tests were performed on the lattice cubes. One lattice cube from each laser power set was used to test compressive strength. The machines used were an Instron Model 1342 with 25 kN capability and Instron Model 1342 with 50 kN capability. The actuator uses oil hydraulics to control movement. The test criteria are specified in Table 12.

Table 12: Compression test criteria

Control type	Speed	Extent of compression	Compress direction
Displacement	0.5 mm/min	To full densification	Build direction

Displacement control is referred to as a closed loop, with the crosshead displacement versus force being fixed. This works well for compression testing, where the movement of the crosshead is not affected by the movement of the sample as it starts breaking. Load control, as an open loop, is more suited for fatigue testing as the force is kept constant. Compression was done for before and after the corrosion tests.

8. Salt spray

The corrosion test used was salt spray, using an ALP Technology Salt Spray Tester, shown in Figure 39, with a controlled chamber temperature of $35\text{ °C} \pm 2\text{ °C}$, which is in accordance with both ASTM B117-18 [60] and ISO 9227:2017 [61] for a 5% NaCl solution. In accordance with MIL-DTL-5541F 2006 [62] and the suggestions listed in ASTM B117-18 and ISO 9227:2017, a total time of 168 hours was used. This was done for both the solid and lattice cubes.



Figure 39: Salt spray fog chamber with samples placed [99]

Two separate salt spray tests were performed. Firstly a neutral salt spray (NSS), with a pH between 6.5 and 7.2 and then an acetic acid salt spray (AASS), where the pH is lowered to 3.1 to 3.3. A summary of the test parameters is shown in Table 13.

Table 13: Salt spray parameters

Test	Chamber temperature	NaCl solution	pH range	Standard
NSS	$35\text{ °C} \pm 2\text{ °C}$	50 g/l ± 5 g/l	6.5 - 7.2	ISO 9227:2017 and ASTM B117-18
AASS	$35\text{ °C} \pm 2\text{ °C}$	50 g/l ± 5 g/l	3.1 - 3.3	ISO 9227:2017

The tests were performed at Scrooby's Laboratory Service, using analytical reagent (AR) quality sodium chloride (NaCl) with deionised water.

8.1 Neutral salt spray (NSS)

The initial salt spray testing (NSS) used four (4) samples from each laser power set for both solid and lattice cubes, and was carried out using four (4) time steps. This means one sample from each laser power set (five samples total each from lattice and solid cubes) was removed at 24 hours, 72 hours, 120 hours and 168 hours. This procedure is laid out in Table 14, with samples labelled as in Figure 30 and Figure 31. The time steps were used to track the corrosion progression.

Only four samples from each laser power set were used, as one sample from each set was used for microstructural examination (solid cubes) and for before corrosion compression testing (lattice cubes), as shown in Figure 30 and Figure 31 respectively.

Table 14: NSS experimental plan

Time step (h)	Sample from each laser power set	Total lattice samples	Total solid samples
24	X2	5	5
72	X3	5	5
120	X4	5	5
168	X5	5	5

8.2 Acetic acid salt spray (AASS)

The AASS test used two (2) sets of samples from the NSS test. The five solid and five lattice samples taken out after 24 hours, and the five solid and five lattice samples taken out after 72 hours. These 20 samples were placed in the acidic salt spray for another total of 168 hours. The samples from the NSS 72 hour time step were removed after 120 hours.

Afterwards the samples were checked in terms of weight and dimension loss. Corrosion product was also collected for analysis.

9. After corrosion exposure

9.1 CT scanning

The same equipment (GE nanotom S system) was used as before corrosion exposure, with the settings of 120 kV and 90 μ A and 10 μ m voxel size, and the Volume Graphics VGSTUDIO MAX software (Version 3.4) to determine the extent of the corrosion.

The same samples were NanoCT scanned to see how, if at all, the porosity influenced the rate of corrosion. This was coupled with possible visualisation of the progression of corrosion through the time step samples from the NSS test in Section 8.1, Table 14.

9.2 Corrosion product analysis

The corrosion product that was collected was analysed using the SEM from Figure 37(b) with SEM-EDS for elemental composition as well as XRD (at the University of Pretoria) for phase analysis.

9.3 Compression testing

Compression testing was done according to the criteria in Table 12. Two sets of after corrosion exposure lattice cube samples were used, to compare to the before corrosion testing done as in Section 7. One set consisted of the five lattice samples taken out after 168 hours in the NSS test, and the other five from the AASS test after 168 hours as indicated in Figure 31.

CHAPTER IV: RESULTS & DISCUSSION

1. Dimensions and mass

1.1 Solid cubes

The dimensional accuracy of the solid cubes had good correlation between the samples in each set, based on the dimensional deviation for each sample from 10 mm, as well as across the laser powers. The variation in the X- and Y-directions was 0.10 to 0.14 mm. The Z-direction, or height of the sample, had a variation across all samples in each laser power set and across all laser powers of 0.5 mm. This larger variation compared to X and Y is most likely due to differences in height where the samples were cut from the supports. The measured value varies depending on which points are used to measure the sample from top to bottom. This is shown by the lines in Figure 40.

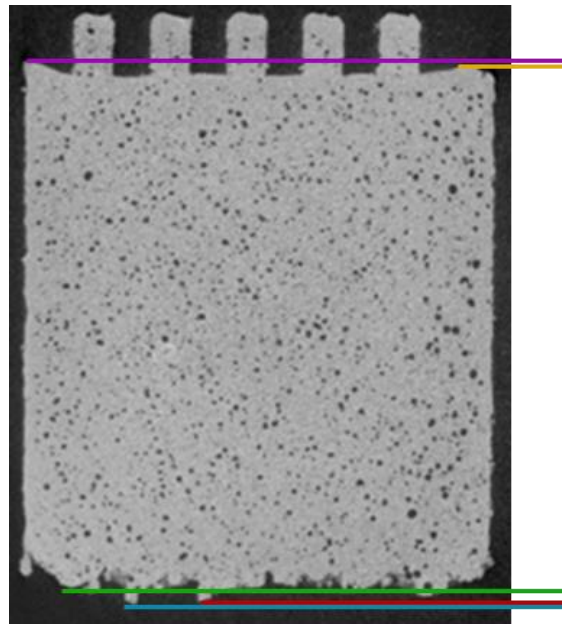


Figure 40: Z-direction measurement variations, indicated by coloured lines

The sample masses ranged from a 2.62 g average for the lowest laser power to 2.54 g average for the highest laser power. The three dimensions versus power are shown in Figure 41(top) and mass versus power are shown in Figure 41(bottom).

The error bars for all graphs in the results were calculated using the difference between the calculated average value and the minimum and maximum measured values to show the range of values obtained.

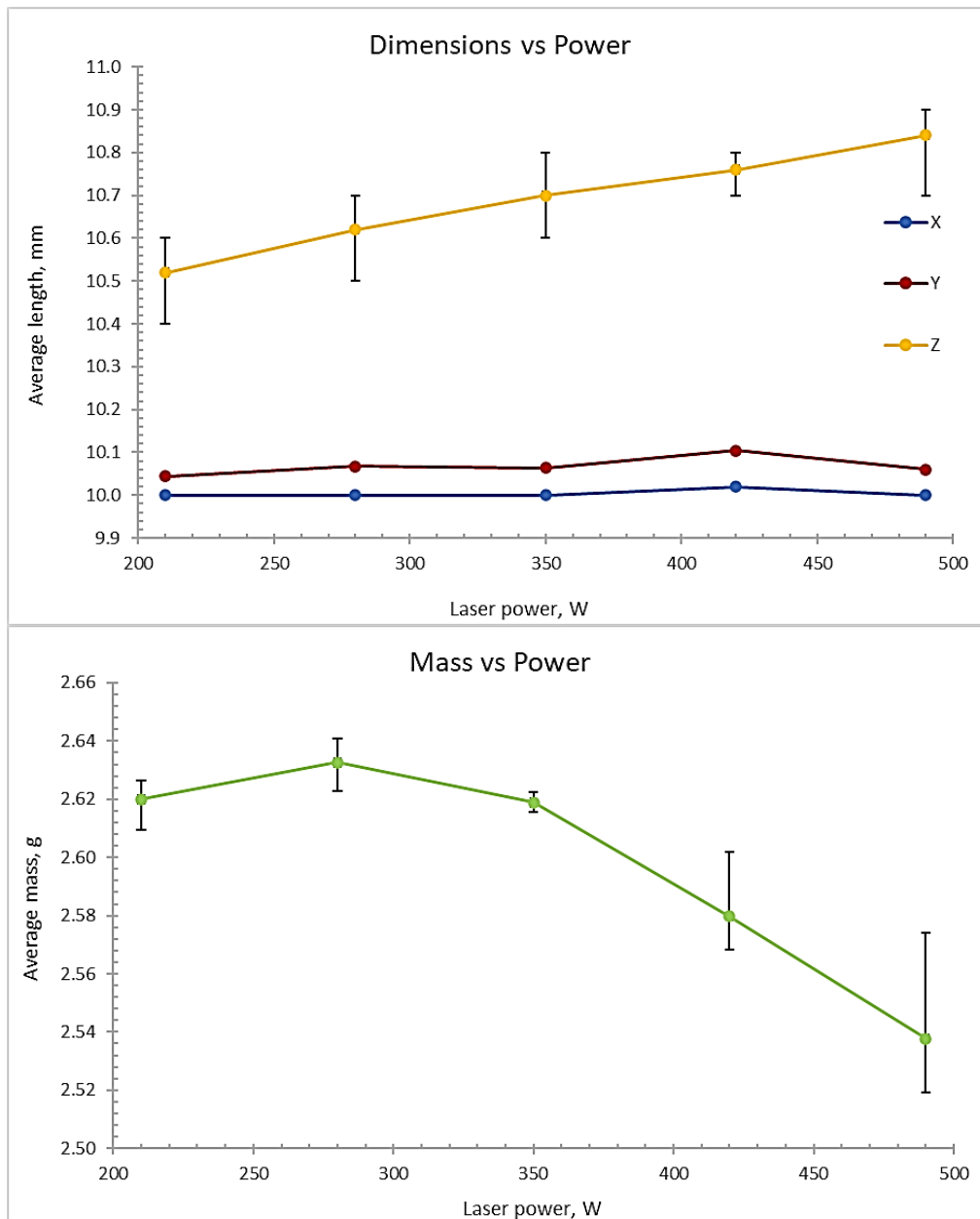


Figure 41: Graphs for (top) dimensions and (bottom) mass versus laser power (Solid cubes)

From the graph it is clear that the Z-direction varies the most. A clear trend is seen for the mass, with a decrease in mass as the laser power increases.

1.2 Lattice cubes

Dimensional accuracy for the lattice cubes showed once again that there was good correlation in the X- and Y-directions, with no variation. The Z-direction, or sample height again varied. This time it was due to the absence of a solid surface, and the irregular surface on the bottom surface that varied depending on where they were cut off from the supports. There was a 0.3 mm variation overall.

The lattice masses varied from an average of 4.75 g for the lowest laser power up to 4.85 g for the highest laser power. The dimensions and mass are displayed versus power in Figure 42(top) and Figure 42(bottom) respectively.

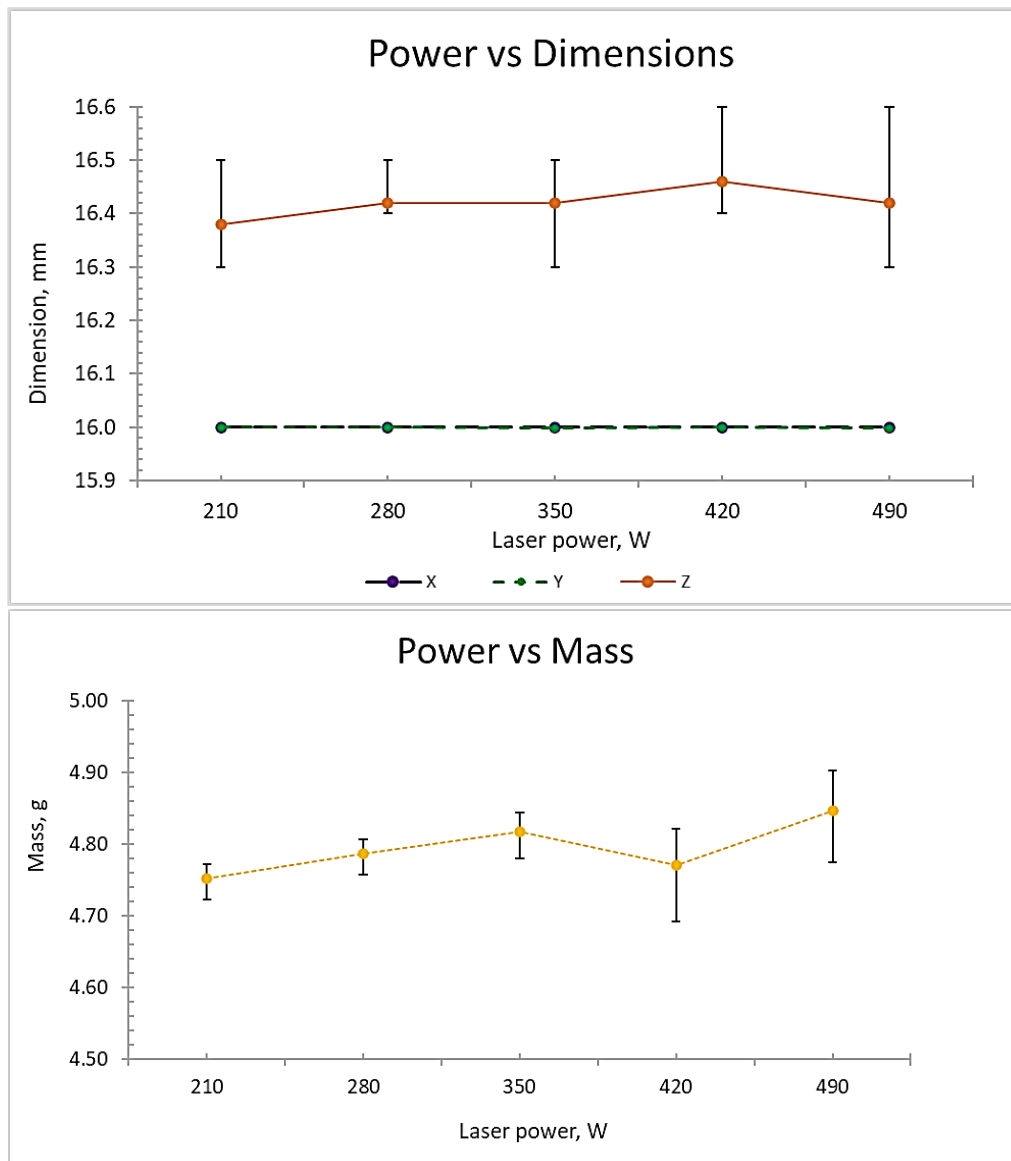


Figure 42: Graphs for (top) dimensions and (bottom) mass versus laser power (Lattice cubes)

The graph clearly shows that the Z-direction varies dramatically here as well, with the error bars showing the variation in each laser power set. The mass does not show a clear trend, with a slight dip in mass at E4 (second highest laser power).

2. Density measurements

2.1 Solid cubes

Three density methods were used to calculate the difference in density of the samples between the different laser power sets. This is shown in Table 15. An increase in laser power is shown to lower the measured bulk density of the samples and all three methods are consistent in this trend.

A refers to Archimedes density, *GP* is gas pycnometry density and *CT* is the CT scan density. AlSi10Mg has a theoretical density of approximately 2.68 g/cm³.

Table 15: Density of samples of each laser power set, according to three measurement methods (Solid cubes)

Laser Power (W)	Density (g/cm ³)		
	A	GP	CT
210 (E1)	2.550	2.610	2.613
280 (E2)	2.549	2.608	2.609
350 (E3)	2.512	2.574	2.576
420 (E4)	2.431	2.495	2.516
490 (E5)	2.365	2.419	2.444

An increase in laser power led to a decrease in bulk density measured, from roughly 2.6 g/cm³ down to 2.4 g/cm³. From Figure 43 it can be seen that the pycnometer and CT-based densities correlate well, whereas the Archimedes density is lower.

This lower value is attributed to air bubbles attached to the surface of the sample when submerged in water, which affects the measured mass of the sample in water.

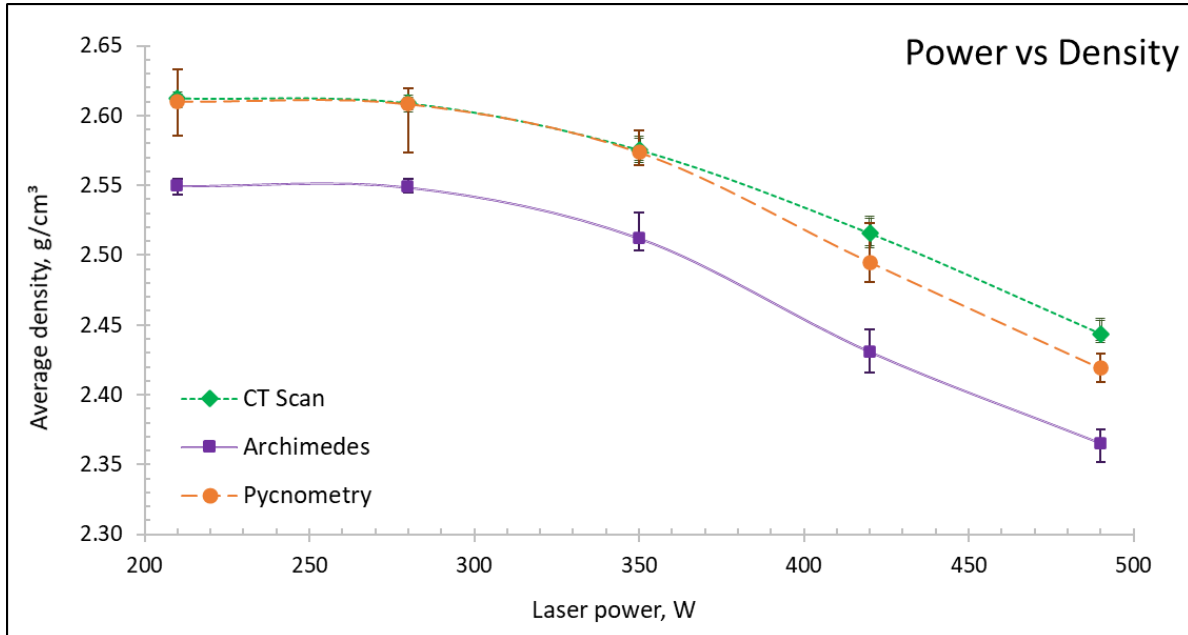


Figure 43: Density calculated with three different methods, as a function of laser power, with error bars.

The rough surface is conducive to air bubbles attaching and this was observed, as in Figure 44.

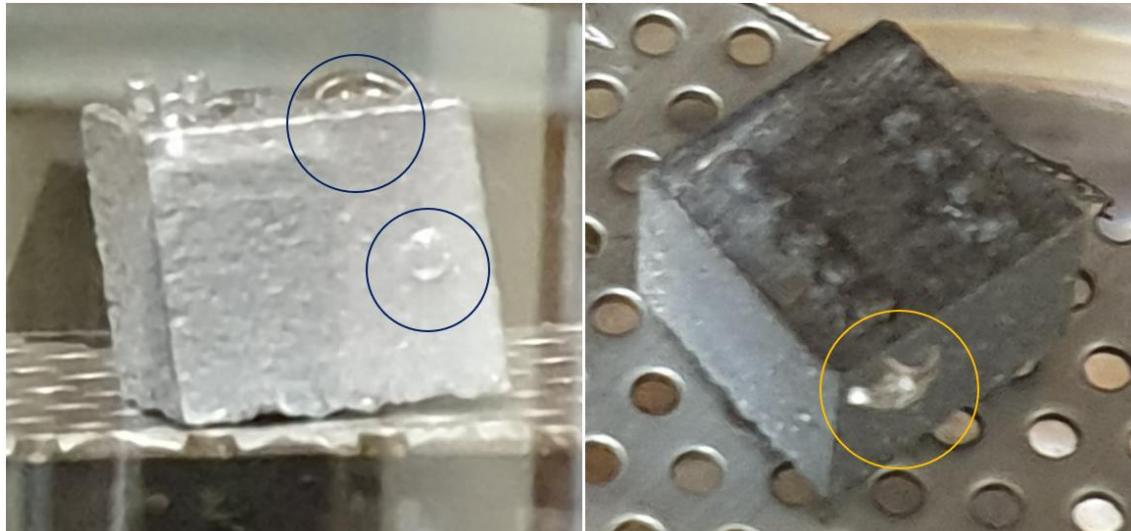


Figure 44: Air bubbles on solid cube surface when submerged, encircled

2.2 Lattice cubes

The three density methods were also used for the lattice cubes. The results are shown in Table 16. *A* refers to Archimedes density, *GP* is gas pycnometry density and *CT* is the CT scan density. AlSi10Mg has a theoretical density of approximately 2.68 g/cm³.

Table 16: Density of samples of each laser power set, according to three measurement methods (Lattice cubes)

Laser Power (W)	Density (g/cm ³)		
	A	GP	CT
210 (E1)	2.381	2.516	2.594
280 (E2)	2.351	2.522	2.599
350 (E3)	2.448	2.527	2.615
420 (E4)	2.361	2.528	2.647
490 (E5)	2.374	2.529	2.675

The three methods are compared visually in Figure 45. It can be seen that all three methods vary greatly from each other. The greatest variation was with the Archimedes method. This is again attributed to air bubbles that attach to the surface when the lattice is submerged. The slight difference in the trend between gas pycnometry and CT scan can be explained as follows:

The CT method measures volume based on surface data to the accuracy of about 15 μm, and mass for average density values. The higher density values compared to gas pycnometry could be because CT measures an average surface, so small variations in roughness are smoothed out. This means small surface 'voids' are included in the CT calculated volume. The gas pycnometer will penetrate all voids, even when they are as small as 1 μm.

Gas pycnometry will show smaller sample volume than CT, due to the surface roughness, and because lattices have a larger surface area. This leads to a larger deviation between gas pycnometry and CT results for the lattices compared to the solid cubes.

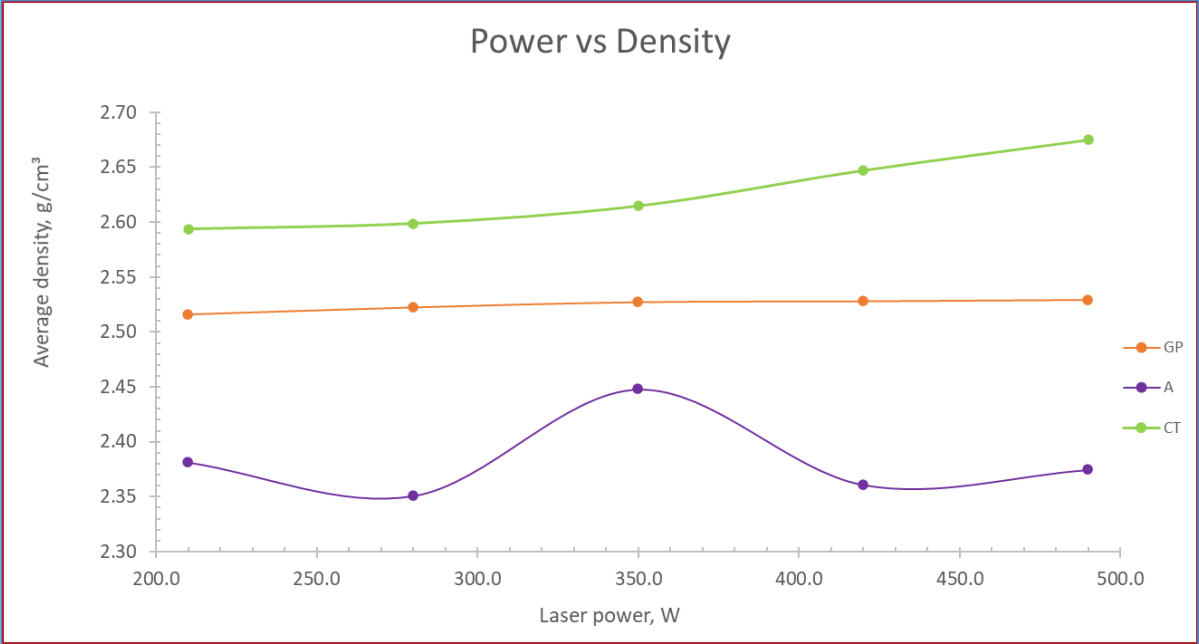


Figure 45: Density calculated with the three different methods, as a function of laser power

The lattice has an even higher surface area for bubbles to attach to, as shown in Figure 46. Along with a larger amount of air bubbles, the assumption of 100% material density will lead to inaccurate results.

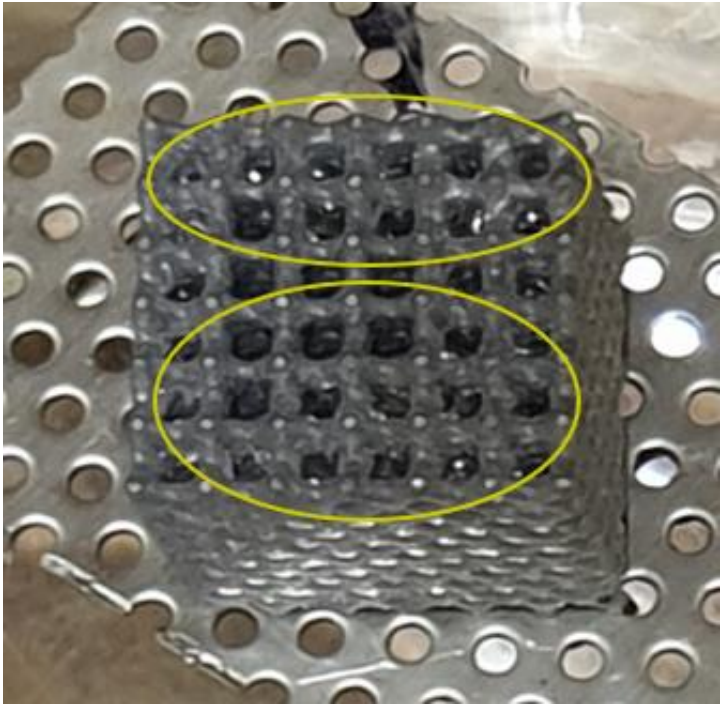


Figure 46: Air bubbles on lattice cube surface when submerged, encircled

3. Surface roughness (Solid cubes)

The solid cubes' surface roughness is shown as close-ups of the top surfaces of representative samples in Figure 47, for each laser power. These images were obtained using VGSTUDIO MAX. The average surface roughness (S_a) per laser power is shown as a text inset above each image. The roughness decreased from $23.7 \mu\text{m}$ at the lowest laser power to $10.5 \mu\text{m}$ at the highest laser power. The first two top surfaces are seen to have a much higher surface roughness than the last two, which corresponds to lower and higher laser power, respectively. The values themselves were obtained using optical microscopy with an Olympus DSX 510, which is not dependent on track orientation relative to scanning, as it uses S_a as described in Chapter II: Section 7, Figure 16. The single pin on these samples indicate they are the first sample in each laser power set.

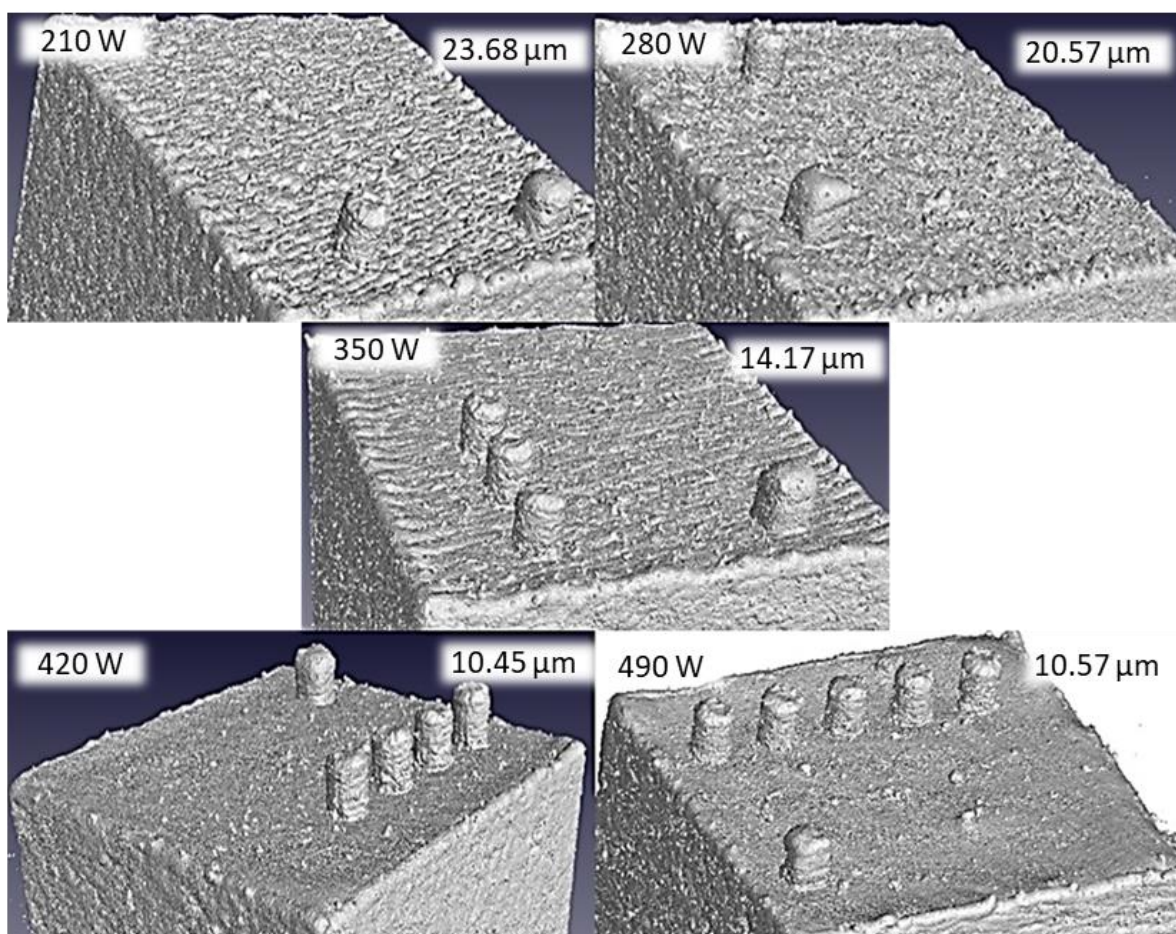


Figure 47: Close-up sections of the top surface of each representative sample for each of the five laser power settings, with S_a values as inserts.

Figure 48 shows how the surface roughness in general decreases with an increase in laser power. The reason for the decrease in surface roughness with laser power increase is most likely due to wider and more overlapping meltpools, which create a relatively smoother top surface. The error bars show that the surface roughness varied greatly in each laser power set.

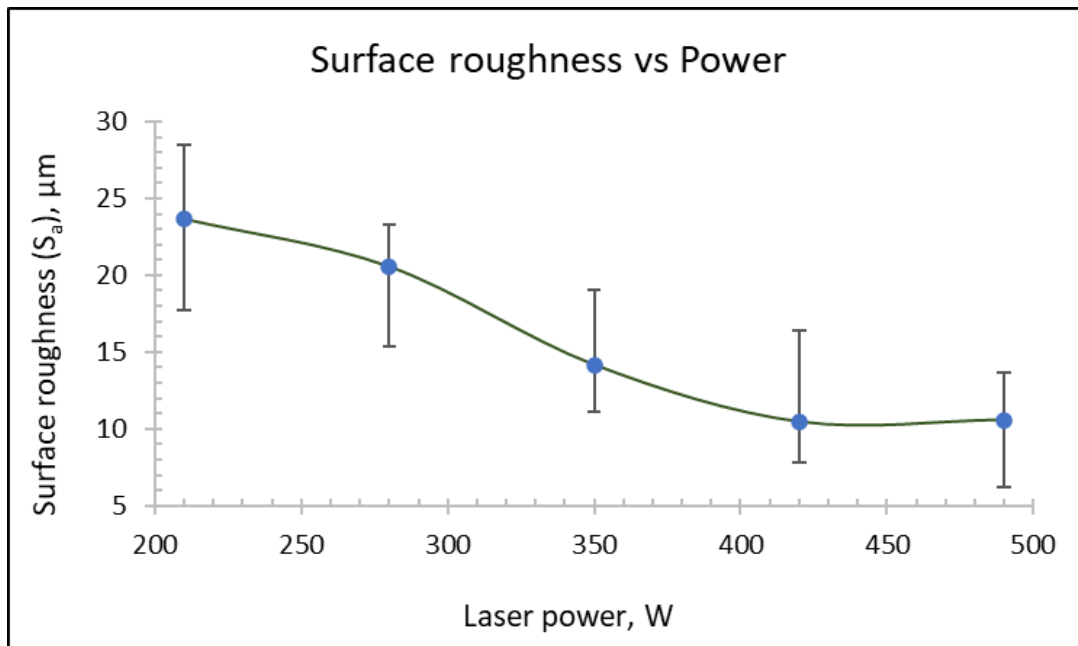


Figure 48: Plot of top surface roughness, S_a , as a function of laser power, with error bars.

The colour scale maps obtained through the Olympus Stream software of the DSX 510 are shown in Figure 49.

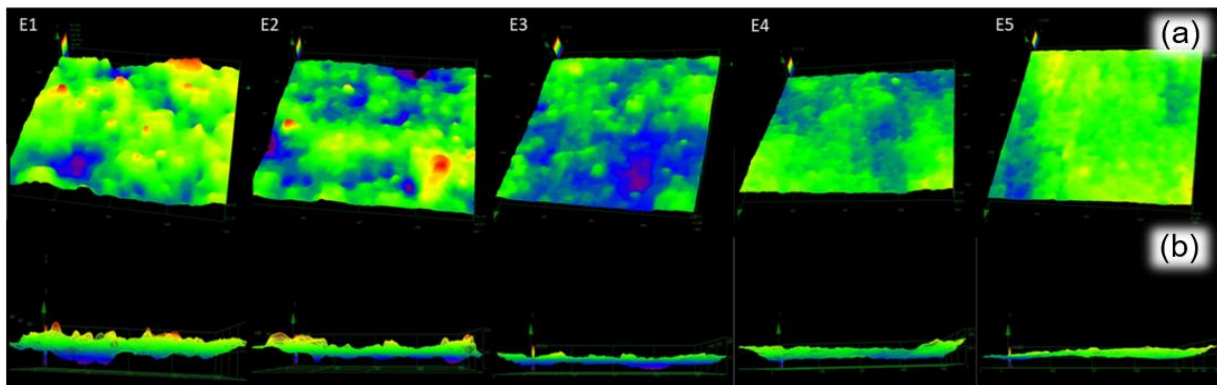


Figure 49: Colour scale maps of samples from each of the laser powers with (a) 3D view and (b) side view, of the top surface

Both the 3D as well as the side view maps also show a larger variation in the surface roughness for the lowest laser powers, and smoother surfaces (less height variation) at higher laser power.

The side surfaces of the samples showed a much smaller variation between laser power, averaging between nine (9) and 11 μm S_a across all laser powers. Whereas the top surface is influenced by the laser power where higher power creates a larger melt pool and more of an overlap, the vertical side surfaces are not influenced by this. Rather, at high laser power and with keyhole regime, the high temperatures can cause particles to attach to the sides, but it depends on surface orientation and requires further investigation to verify if this is what causes the larger error bar range for the highest laser power.

At low laser power and in lack-of-fusion regime, if there is extensive lack of fusion, it creates spaces between tracks and layers, which increases surface roughness. This effect is shown in Figure 50. The errors bars also show how, at the highest and lowest laser power, the surface roughness varies much more than for the middle laser powers. This shows that the middle power is more stable with continuous tracks and hence has cleaner side surfaces, while irregularity in track width starts at lower and higher power. However, the average values have a very small variation compared to the error bars. This is shown in Figure 50. There is a larger variation in S_a values of the highest and lowest laser power sets (E1 and E5) than for the middle laser powers, but the averages across all the laser powers have a very small variation, ranging between nine and 11 μm . This shows that the side surfaces across all the laser powers are relatively similar.

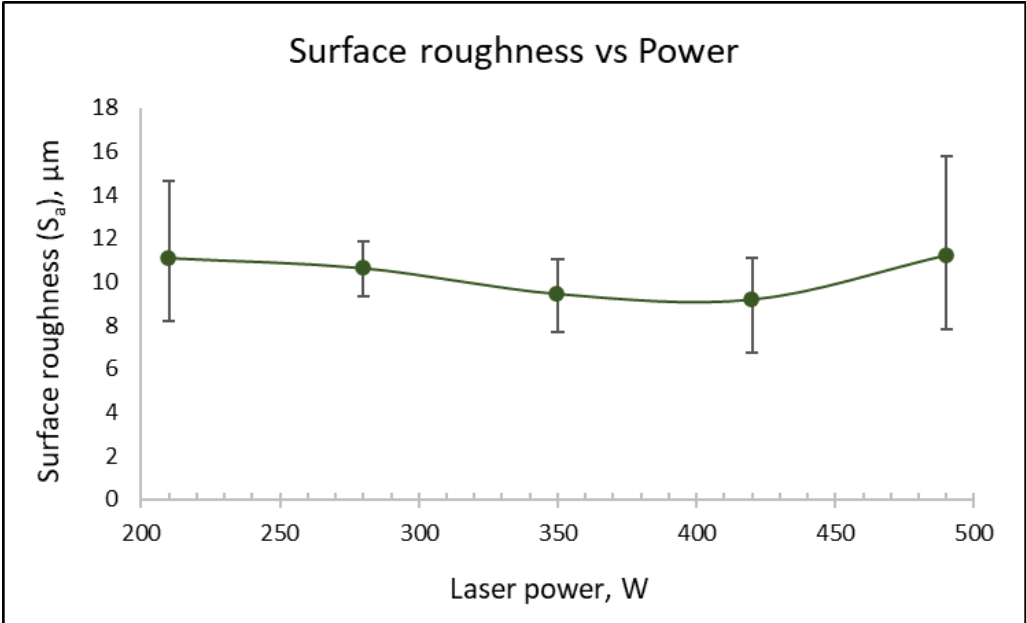


Figure 50: Plot of side surface roughness, S_a , as a function of laser power, with error bars

4. Metallographic examination

The cross-sectioning and subsequent mounted area visible is shown in Figure 51. The exposed plane is labelled.

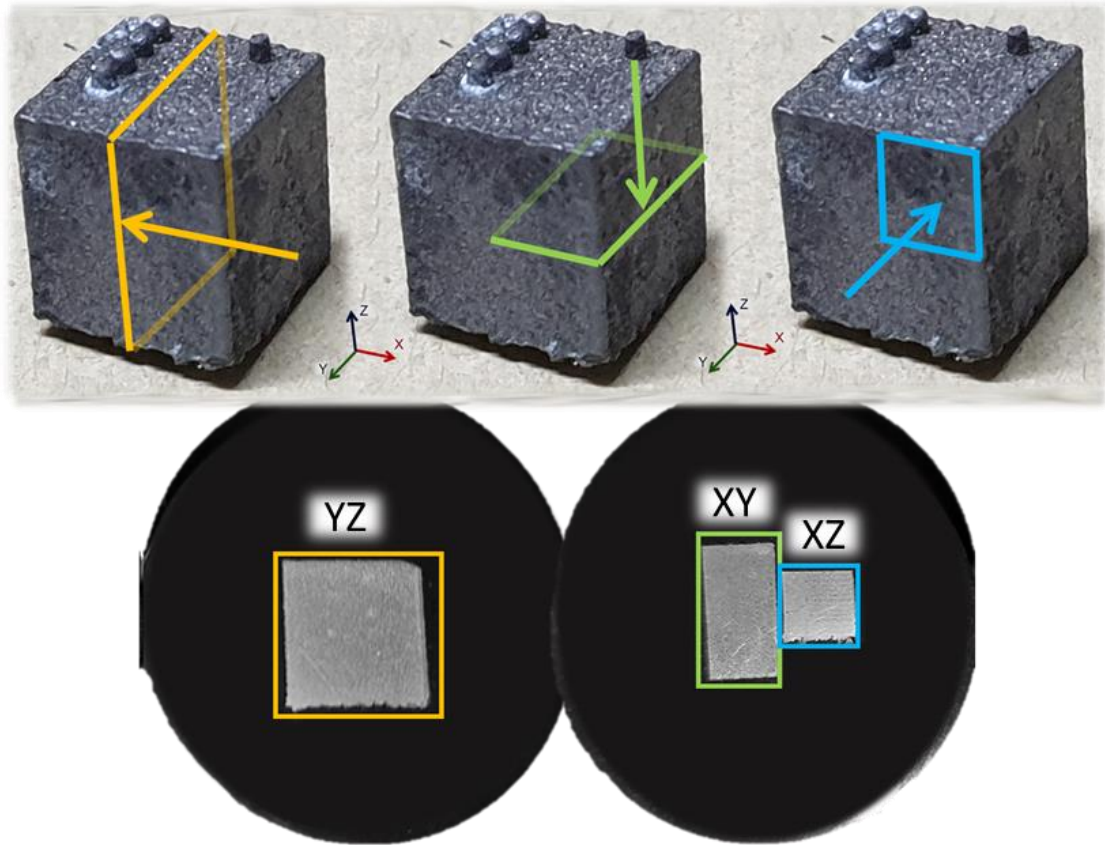


Figure 51: Sectioning and mounted samples to show the three exposed planes that were examined

The microstructure of the samples from all five laser powers is shown in Figure 52. The initial appearance does not show a large difference in the microstructure between each laser power. The purple arrows point out coarse cellular zones, similar to what is described in Chapter II: Section [3.2](#) “Characterisation of L-PBF parts”, Figure 7.

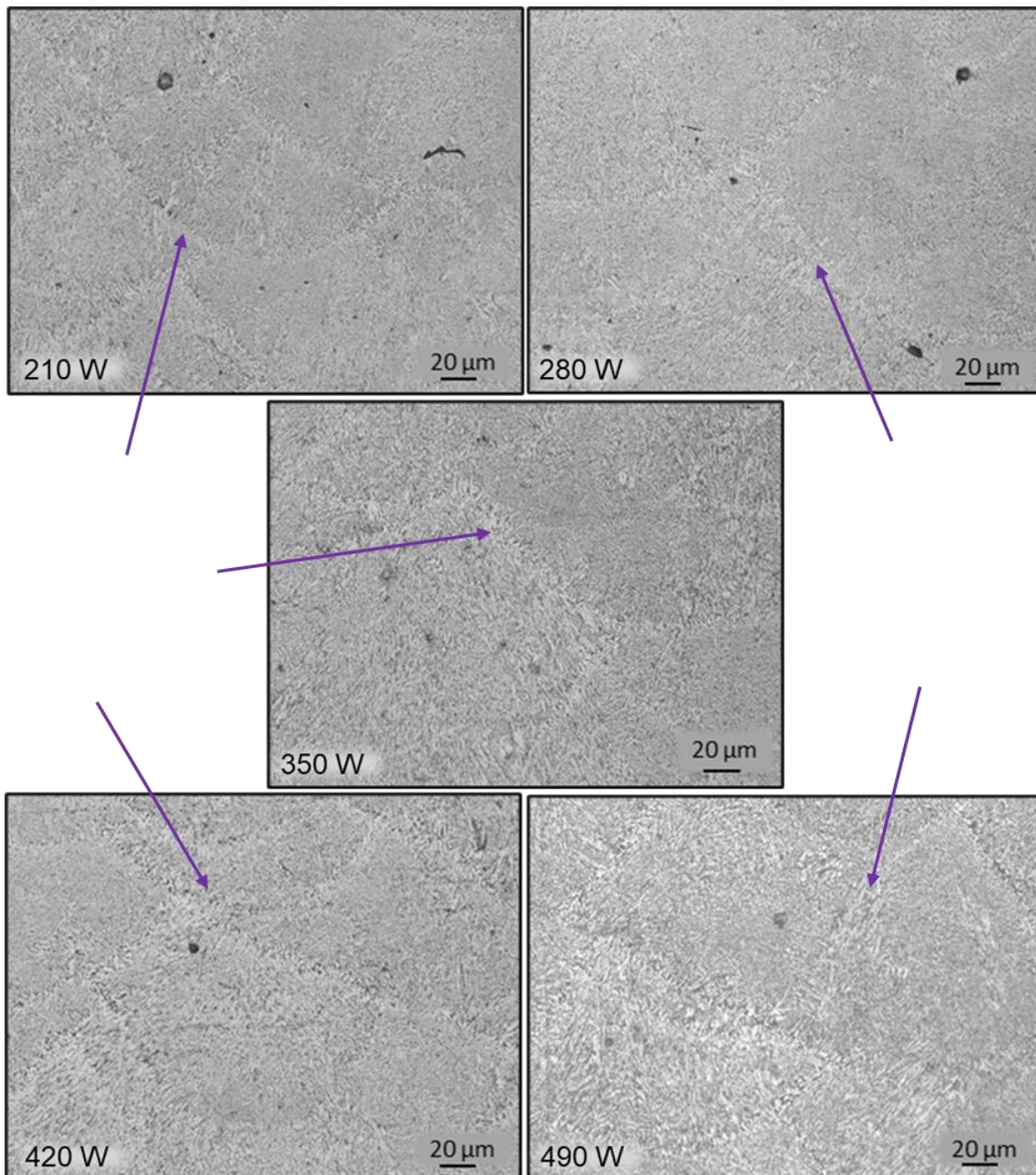


Figure 52: Microstructures of all five laser power samples

To further investigate whether there are significant differences in the structure, hardness tests were performed on samples from each laser power set. A large change in microstructure would lead to a large difference in hardness. The graph for Vickers hardness versus laser power is shown in Figure 53. A minimum of five hardness measurements were taken across the entire sample surface to obtain a representative value, while aiming to avoid indentations on or near visible pores. The indentation areas were chosen by making sure previous indents were not visible through the eyepiece of the Vickers hardness machine and by visually checking that there is sufficient coverage of the whole sample surface.

From literature in Chapter II: Section [3](#) “The alloy AlSi10Mg”, hardness values for as-built AlSi10Mg ranged from 120-127 HV and in one case up to 136 HV.

The values shown in Figure 53 are all higher than the typical values reported, apart from the one that reported values up to 136 HV. However, their values were measured from the surface to 2.5 mm into the samples, whereas the measurements here are all at the same depth (exposed surface of mounted samples). They also used different process parameters [35].

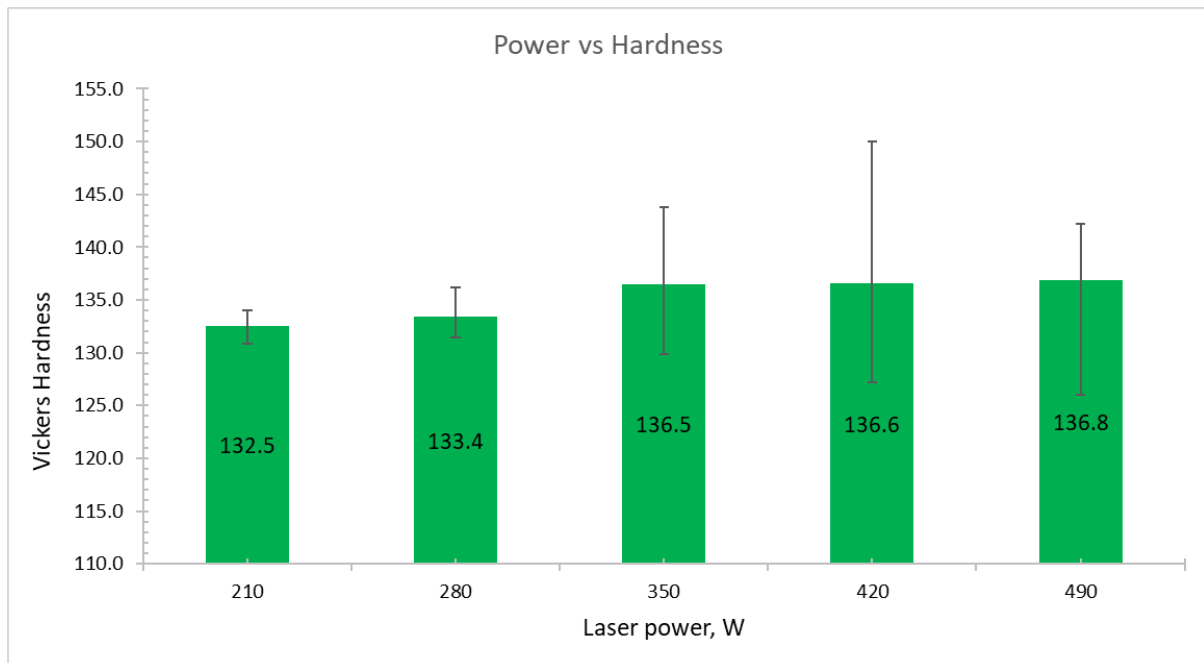


Figure 53: Vickers Hardness versus laser power, with error bars

From the graph it is clear that the difference in hardness is very small, as the difference in average hardness is below five (5) Vickers (4.3 HV). This is within the margin of error of measurement for a single sample. This verifies that there is not a significant difference in microstructure between the laser power sets. The larger error bars for the higher laser powers are due to the increased amount of porosity. This means care had to be taken when measuring, as pores could cause a much lower hardness result. Also, by trying to avoid pores during measurement, there was an increased chance to place an indentation over an inclusion, which would subsequently result in a much higher hardness result.

The chemical composition was analysed using SEM-EDS over multiple areas to better represent the whole sample. Special focus was on the magnesium (Mg) and silicon (Si) amounts. Magnesium was found to range between 0.22 wt% and 0.44 wt%, while silicon ranged between 10.03 wt% and 10.72 wt%. The highest laser power had the lowest %Mg and highest %Si. This can be due to the vaporisation of Mg at higher temperatures [4,107,108].

Referring back to the hardness values obtained in Figure 53, there was only a small difference, and hardness is influenced by microstructure, not composition. This slight variation in composition did not play a large role, as no heat treatments were performed which could have precipitated Mg_2Si . SEM-EDS has merely shown the effect laser power has on the original chemical composition.

5. Porosity measurements

5.1 NanoCT scan porosity measurement

5.1.1 Solid cubes

CT scan images of one representative sample from each laser power set is shown in Figure 54. From left to right the power settings were 210, 280, 350, 420 and 490 W. It can be seen that the first two cross-sections on the left have very small amounts of porosity, which corresponds to the lower power settings. The last two cross-sections on the right are seen to contain pores larger in quantity and size and are rounded, which corresponds to the higher laser power. This large, rounded porosity at high power is attributed to keyhole mode porosity formation.

The encircled areas in Figure 54 show the presence of high-density inclusions, which could potentially be due to contamination from the powder itself, as Al-alloys usually have iron (Fe) containing impurities present. The system used at RMIT University has the advantage of only processing Al-alloys, so the inclusions are not contamination from a previous build. Higher density particles from the powder itself could include iron (~7.9 g/cm³), chrome (~7.2 g/cm³), manganese (~7.3 g/cm³), nickel (~8.9 g/cm³), titanium (~4.5 g/cm³) or copper (~8.9 g/cm³). It is also quite possible that some of the inclusions are Al₂O₃ (3.99 g/cm³) if oxidation occurred during spattering even in the inert gas atmosphere used for manufacturing. The density of the inclusions is higher than the alloy, thus appearing brighter in the scans. It is clear that as laser power increases, the number of high density inclusions decreases. This can be attributed to higher temperatures or larger or deeper melt pools creating more melting/remelting and homogenization of the material. The pins in these images refer to the laser power used to produce the samples, with one pin for 210 W and five pins for 490 W. The green vertical arrow indicates the build direction.

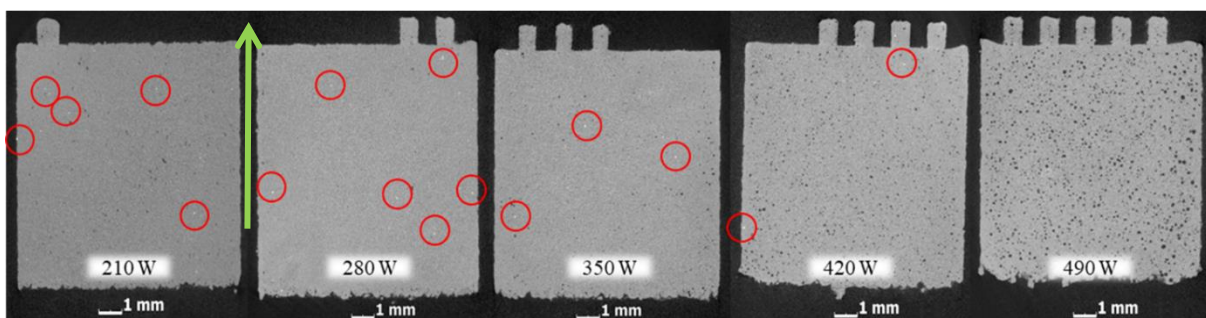


Figure 54: Representative CT cross-sectional images for each of the five different laser power settings showing porosity (black dots) and also indicating the presence of some dense inclusions (white dots encircled in red). Arrow indicates build direction

Table 17 shows the total percentage of porosity, obtained from the CT results, corresponding to each laser power set, as well as the relationship between the two in a graph insert. As seen in Figure 54 and Table 17, the lowest power E1 has slightly more porosity than E2. This can be explained as due to lack of fusion porosity at 210 W and the ideal melting with lowest porosity content at 280 W compared to 210 W.

The difference seems small in comparison to the difference with the higher laser powers, however there is a statistically significant difference. The 210 W laser power resulted in an average of 0.16% porosity with a variance of 0.0024 and standard deviation of 0.0495, whereas the 280 W laser power resulted in an average of 0.08% porosity with a variance of 0.0001 and standard deviation of 0.0103. As laser power increases further, the total amount of porosity increases, which is due to more keyhole porosity and consistent with previous work [17].

Table 17: Porosity percentage of each power set and plotted as a function of laser power (graph inset), solid cubes

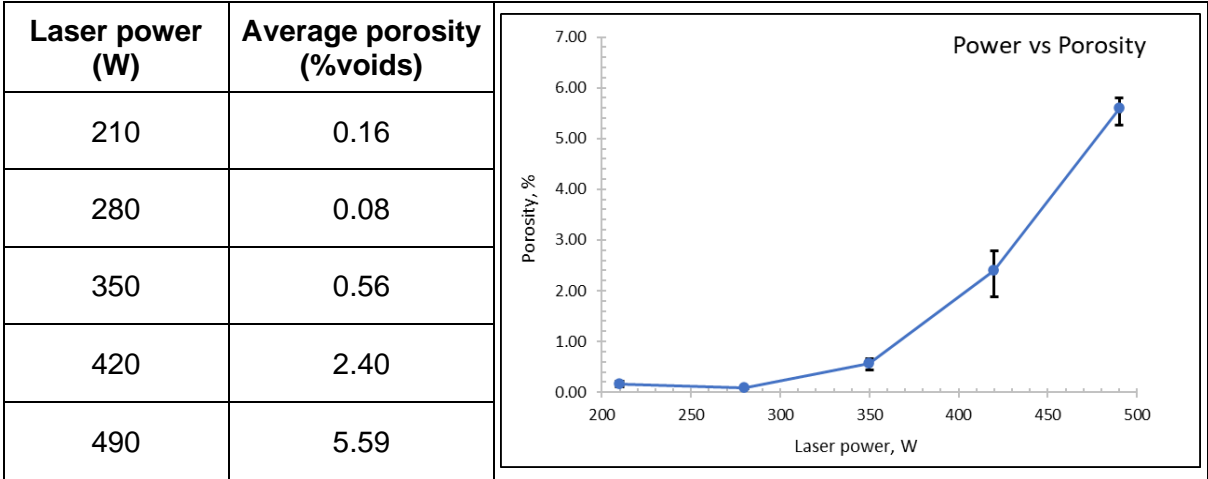


Figure 55 shows optical micrographs for low laser power (E1) showing lack-of-fusion pores (encircled in purple), and high laser power (E5) showing the more spherical pores (encircled in yellow).

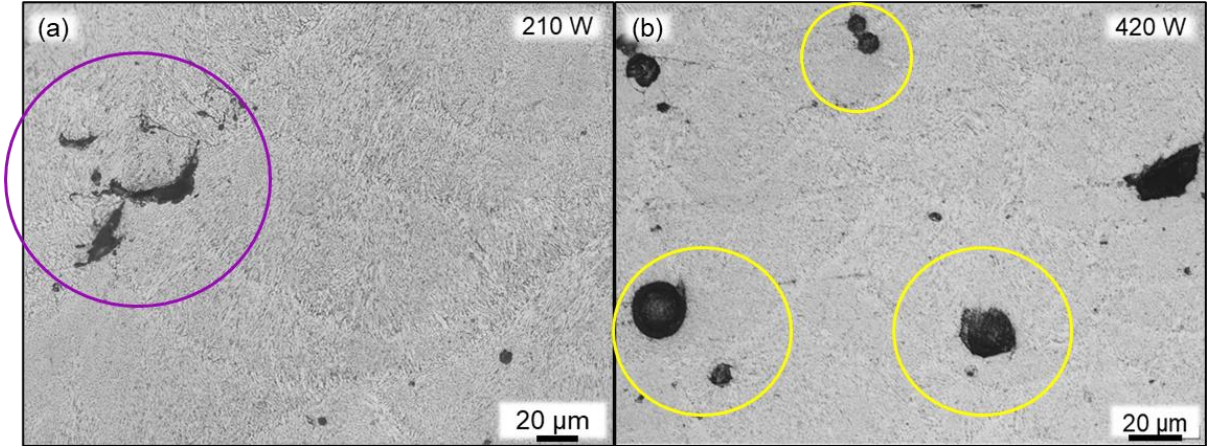


Figure 55: Optical micrograph of (a) lack-of-fusion pores at low laser power (E1) and (b) spherical pores at high laser power (E5) (Encircled), solid cubes

The CT porosity analyses are shown in 3D representations in Figure 56. The porosity percentage of those specific region of interest (ROI) (4 x 4 x 4 mm³) cubes are added as inserts, with the overall average of the porosity from all 10 x 10 x 10 mm³ cubes in each laser power set in brackets next to it.

Here it is clearly seen that the lower laser power samples have relatively little porosity, especially compared to the samples manufactured at the higher laser powers. The higher laser power samples are seen to have much higher porosity and the pores are more spherical in shape, whereas the lower power samples are seen to have less spherical, lack-of-fusion type pores.

The trend seen in the porosity should have an inverse relationship to the trend in density seen in Figure 43 and Table 15, as higher porosity levels are expected to lower the density. However, the presence of lack of fusion porosity at higher values in E1 compared to E2 is not consistent with the calculated density values in Figure 43 and Table 15 and therefore requires explanation. Despite the small average values of 0.16 and 0.08% porosity, all density methods showed the E1 sample to be slightly denser. The most likely explanation for this observation is that the bulk density measurements inaccurately measure the bulk density when irregular shaped pores are present on the surface. Small variations in high-density inclusion content will not have an effect, as all samples were made with the same powder and whether the inclusions melt or not will not make a difference to the mass.

Such pores create open cavities allowing water or gas to enter the object in surface-connected pores and are thus excluded from the measurements. The CT-based segmentation also might select more of this or may be inaccurate - the CT volume measurement for bulk density requires accurate calibration of the voxel size, unlike the porosity % value in Table 17 and Figure 56. The shape of the porosity is clearly more irregular at the lowest laser power and more spherical at higher power. The long, irregular pores are seen clearly in E1 versus the more spherical pores at higher laser powers. A scale representation is inserted to show the lengths of each side for all five cubes.

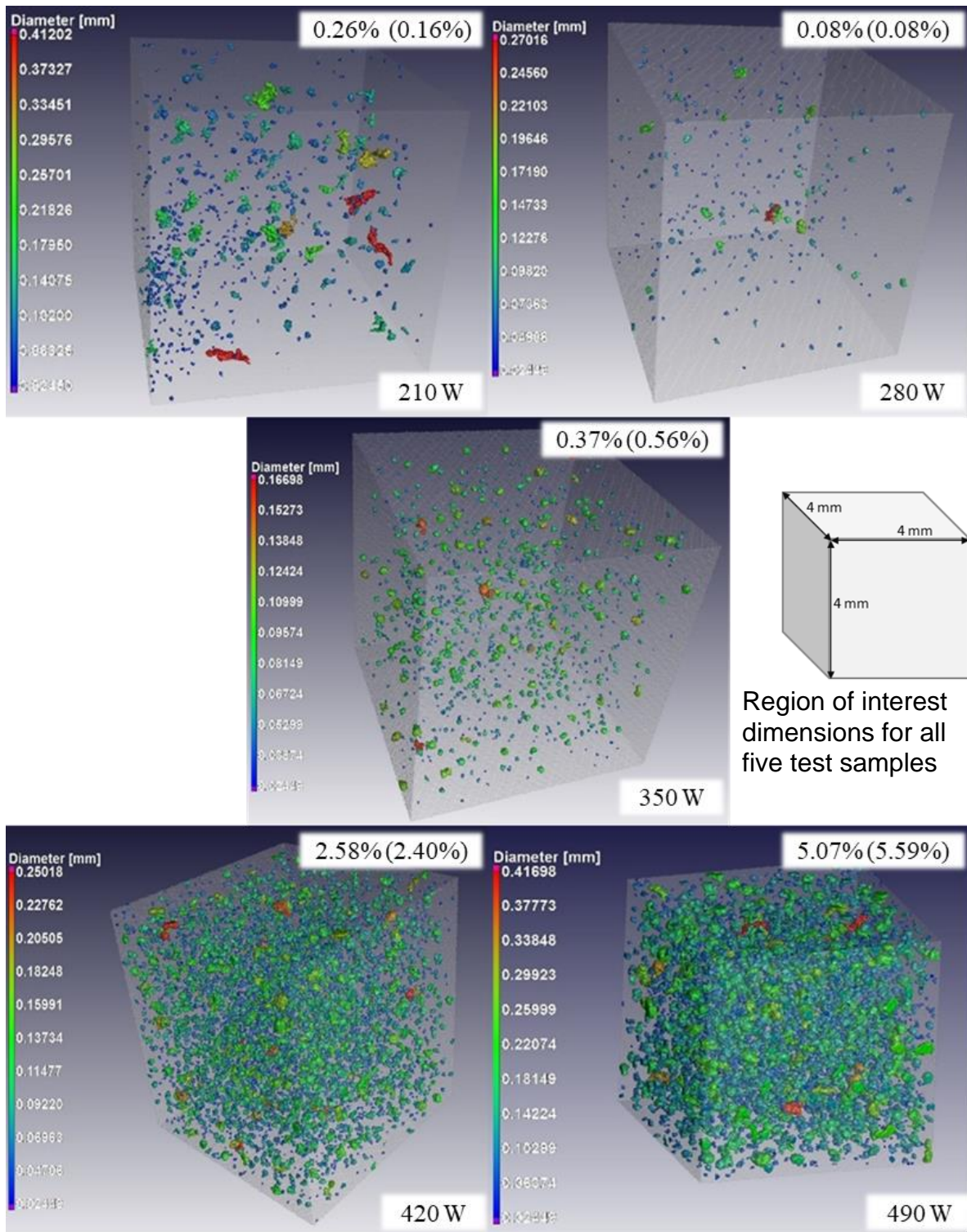
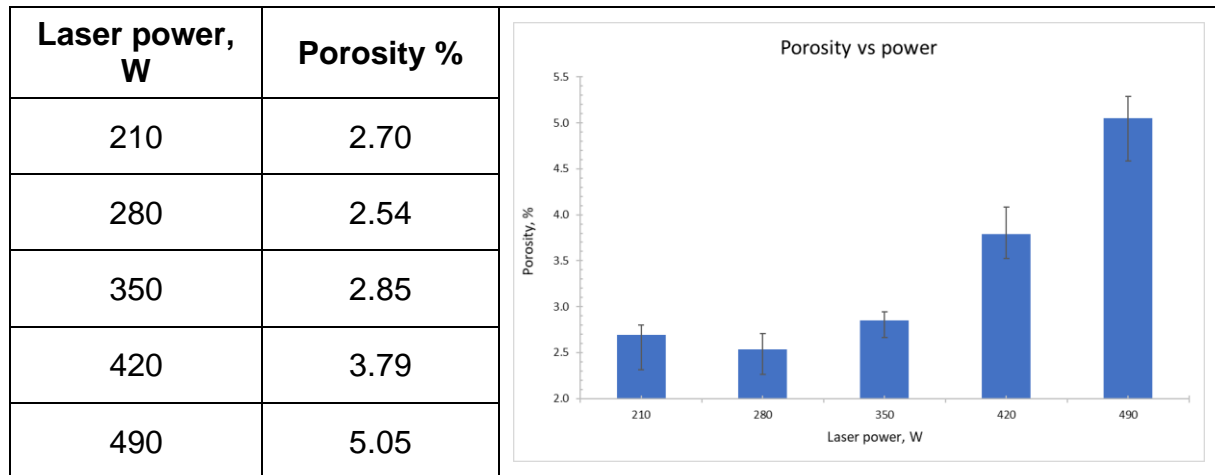


Figure 56: Porosity analyses, for a 4x4x4 mm³ region of interest, of representative samples for each of the five laser power settings, from (top) low power to (bottom) high power, with actual porosity value of ROI as insert, and overall average of whole cube (10x10x10mm³) in brackets, solid samples.

5.1.2 Lattice cubes

Table 18 shows the average porosity percentages for each laser power, with graph insert.

Table 18: Porosity versus laser power, graph insert with error bars (lattices)



The results show a general increase in porosity with an increase in laser power, which is the same trend as in the solid cubes.

Figure 57 shows NanoCT slice images of the lattice structure. The slice images clearly show the uneven top and bottom surfaces. All slices were taken from the centre of the sample.

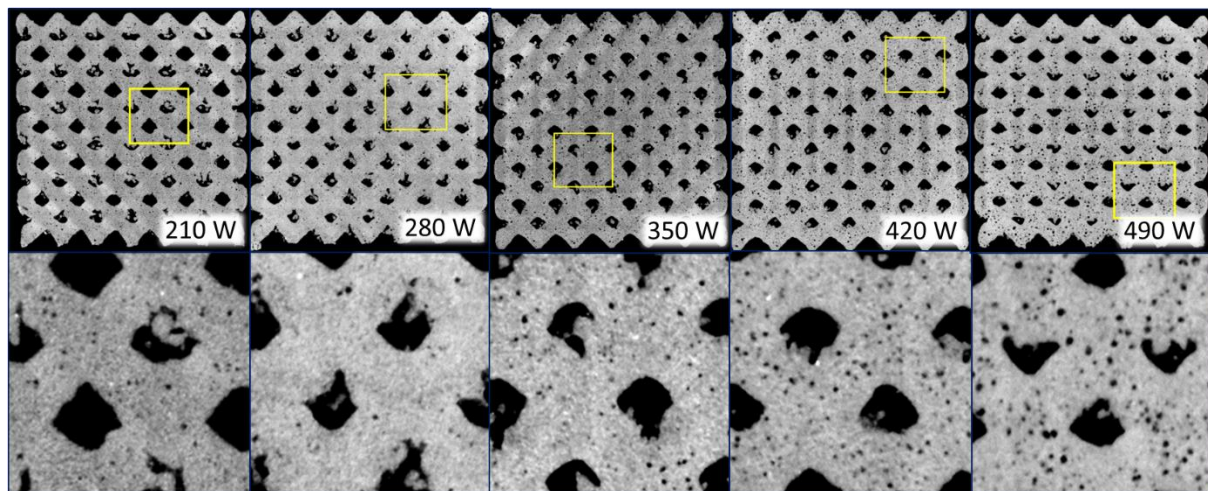


Figure 57: NanoCT slice images of the lattice structure for each laser power, with zoomed in slices below each overview image

Zoomed in areas are shown below the overview image to highlight the trend in porosity is similar to the solid cubes. As with the slice images of the cubes in Figure 54, it is seen that there is increased microporosity in the struts with higher laser power.

Optical micrographs in Figure 58 show that at high laser powers, the lattice struts have spherical pores, as well as at low laser power (encircled in yellow).

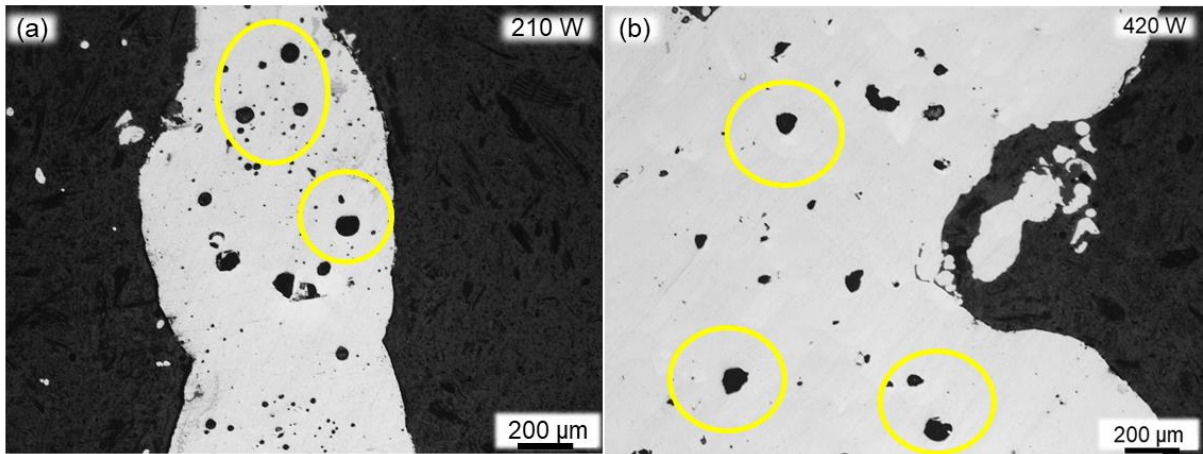


Figure 58: Optical micrographs of spherical pores at (a) low laser power (E1) and (b) high laser power (E4) (Encircled)

Figure 59 shows NanoCT scans of lattices from all laser power sets, with porosity analysed.

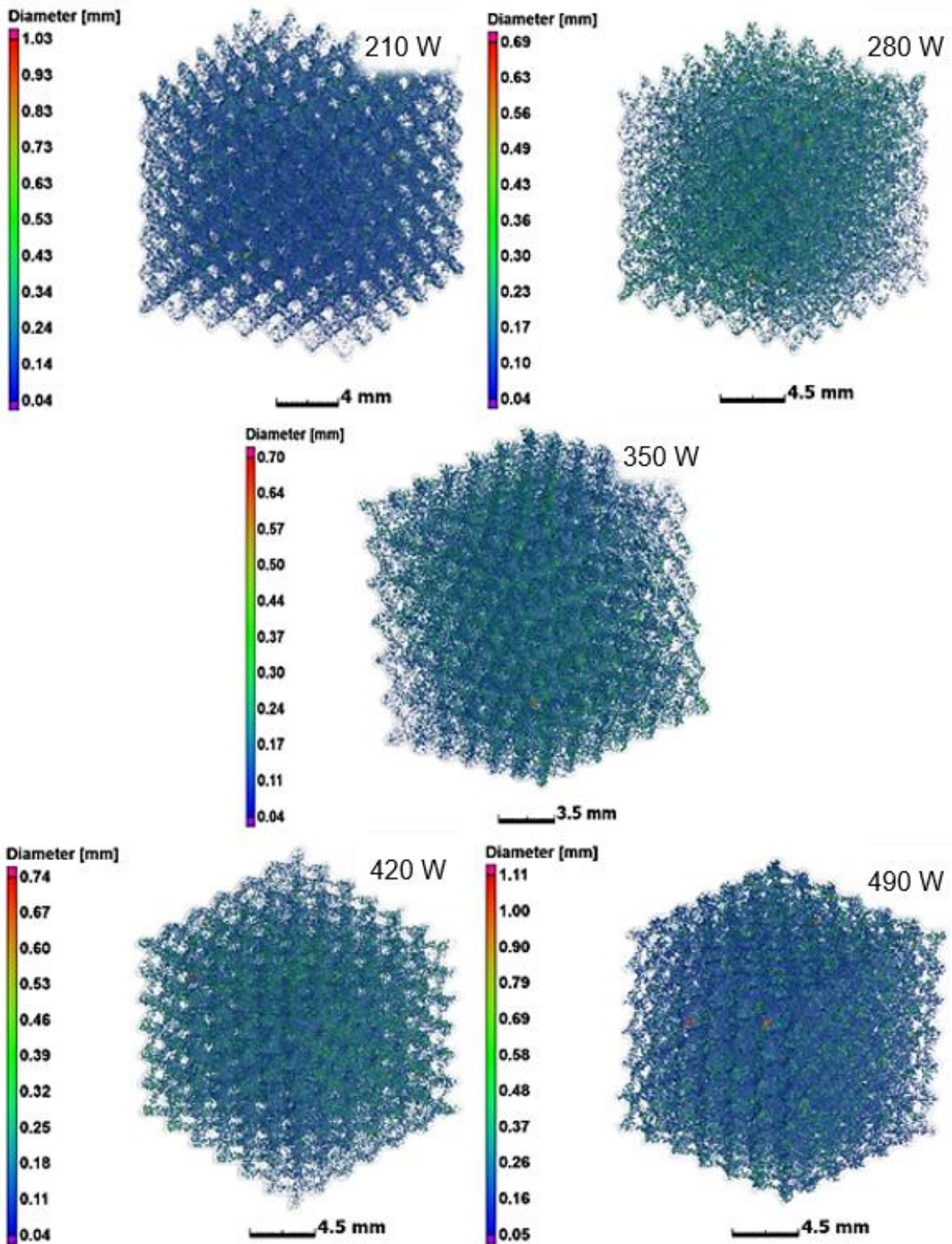


Figure 59: Porosity analyses of the lattice samples for each laser power

The colour scale bar on the left side of each lattice shows that the lattices have variations in pore size, with the highest and lowest laser power having pores larger than 1 mm in size. The second lowest and middle laser powers have similar size ranges, and the second highest laser power has a slightly larger size range than the former two.

6. Compression testing (Lattice structures)

Figure 60 shows a photo of a compression test. The photo was taken soon after the point where the first compressive yield stress had been reached for some of the sample's struts, and some struts have already experienced shear failure. The failure is observed to occur in a diagonal 45 degree direction. As the failure occurs, there are repeated yield and recovery cycles.

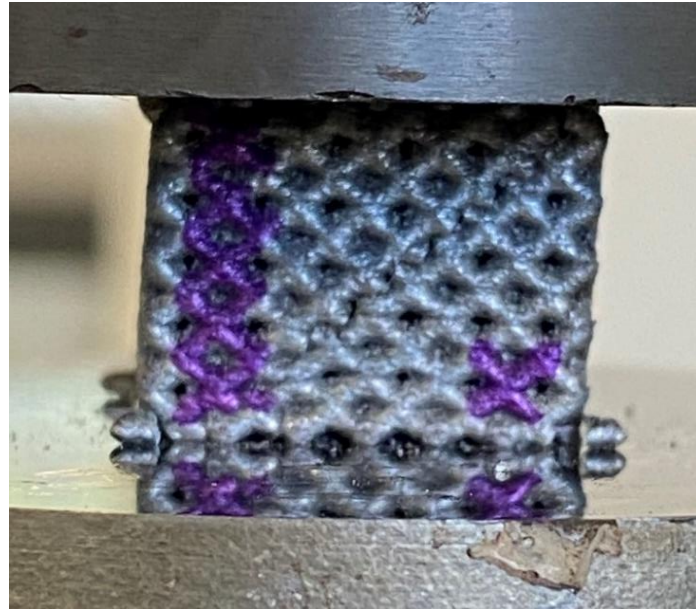


Figure 60: Compression test in action

The relationship between compressive strength and laser power is shown in the graph in Figure 61. This is the maximum compressive yield strength reached at the peak of the initial linear elastic region, before corrosion exposure.

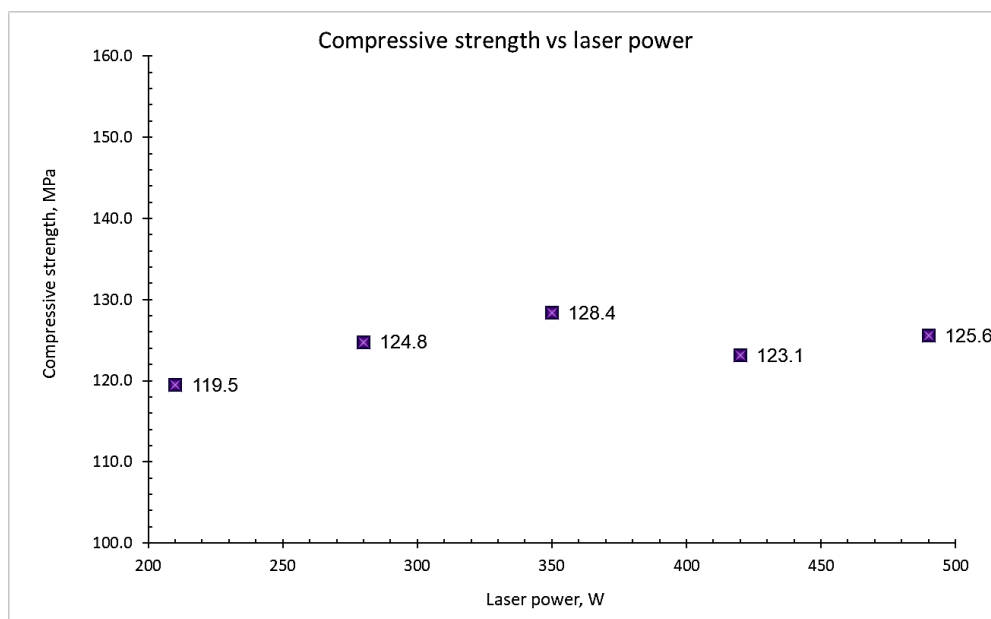


Figure 61: Compressive strength vs laser power, before corrosion exposure, lattice structures

It can be seen that the compressive strength for all five (5) laser power sets are close in magnitude, with a range of 8.9 MPa between the maximum and minimum strength. This falls within the margin of measurement for one set. The compressive stress-strain curves are shown in Figure 62. The purple arrow indicates where the compressive strength was recorded, as the maximum yield value after the initial linear elastic region.

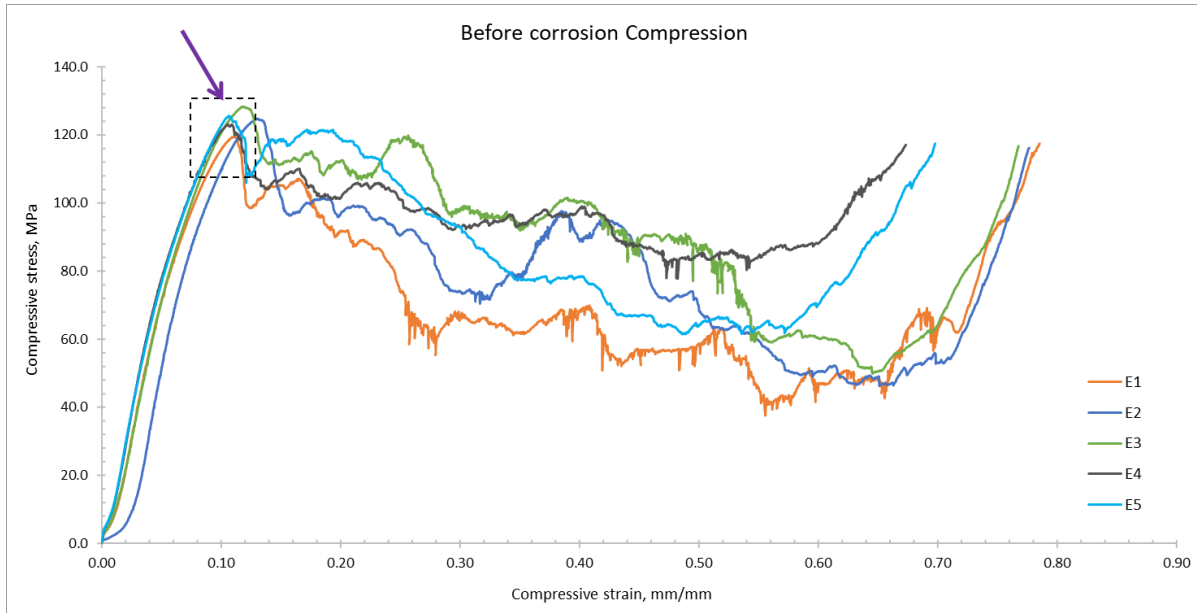


Figure 62: Compressive stress-strain curve for the five samples before corrosion exposure, lattice structures

The compressive stress-strain curves for the samples before corrosion exposure show a similar trend in the initial linear elastic response. The yield and recovery cycles vary between the samples, and the start of full densification also varies. This is similar to what was seen in Figure 26 of Chapter II: Section 9.2 “Design considerations”. The compressive yield strength is taken as the first yield point reached, which is also the maximum yield strength.

7. Salt spray

7.1 Neutral salt spray (NSS)

Figure 63 shows the solid and lattice samples taken out after 72 and 168 hours.

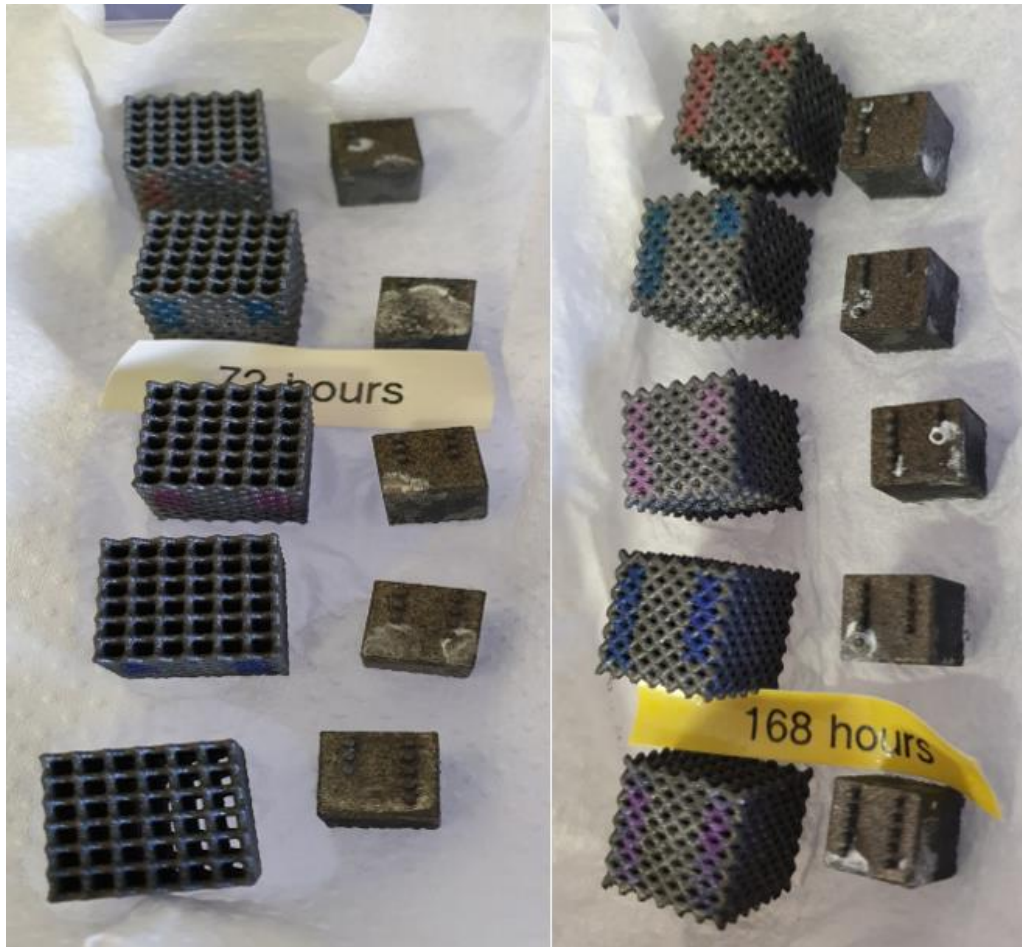


Figure 63: NSS after (a) 72 hours and (b) 168 hours

Some corrosion product has formed, but visually alone it cannot be said what the extent of corrosion is and whether it differs between the time steps.

7.2 Acetic acid salt spray (AASS)

Figure 64 shows the samples from the acetic acid salt spray test taken out after 120 hours for the top image, and taken out after 168 hours for the bottom image.



Figure 64: AASS for (top) after 120 hours and (bottom) after 168 hours

Here it can be seen that there was more extensive corrosion product that formed than with the NSS test. The samples taken out after 168 hours show even more corrosion product than those taken out after 120 hours.

8. After corrosion exposure

8.1 CT scanning

8.1.1 Solid cubes

The NSS corrosion test results showed limited corrosion, even after 168 hours (7 days). Therefore, the AASS corrosion test was carried out the set of samples from the NSS test that were subjected to only 24 hours NSS corrosion exposure. This is due to virtually no corrosion observed in the 24 hour NSS samples. With the AASS test, the corroded samples showed some low-density material (corrosion product) on and near the surface. No significant pitting was observed, and this could be due to the initial corrosion behaviour mainly being uniform corrosion with metastable pitting on the surface. It could also be due to a passive oxide layer decreasing the surface's susceptibility to selective or pitting attacks. These possibilities were mentioned in Chapter II: Section [8.4](#) "Review studies on Al corrosion". An overlap of before/after scans to precisely image locations of corrosion was performed. A deviation calculation (called nominal-actual comparison) visually highlights the largest corrosion locations as well as locations of excess material (likely corrosion product).

Figure 65 shows a 3D image of a sample from the lowest laser power (E1) exposed to AASS for 168 hours, with the corroded areas shown in an overlap by the blue regions, and the corrosion product by the red material.

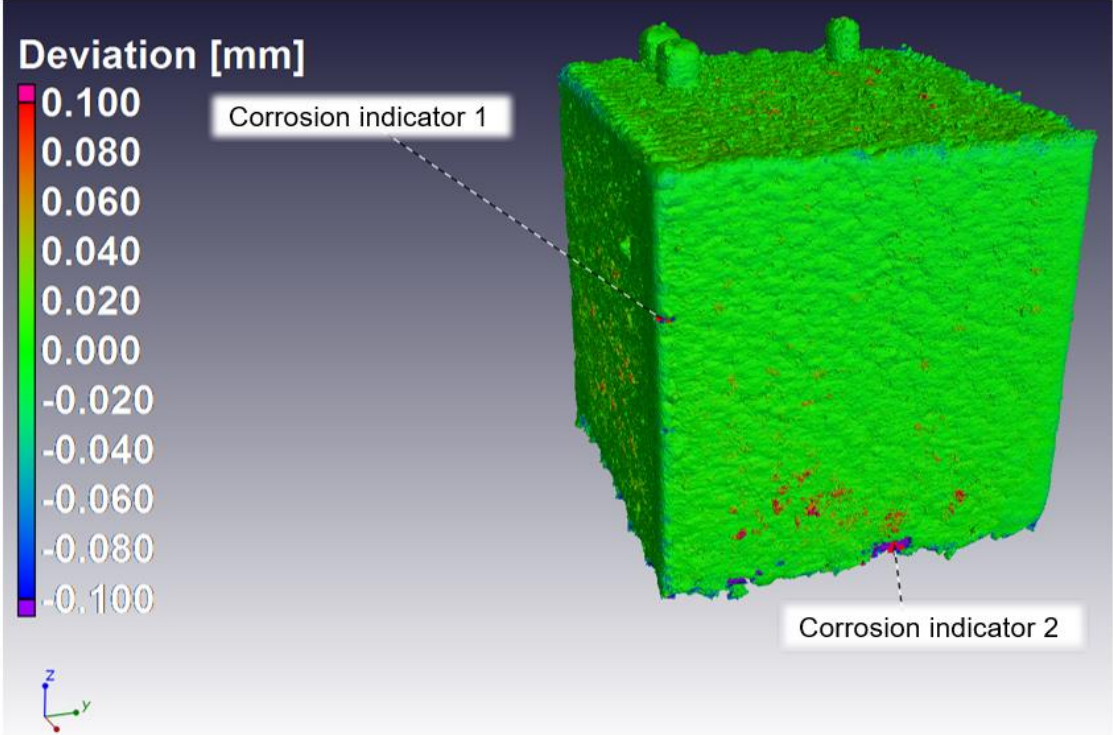


Figure 65: Sample from the lowest laser power (E1), with corrosion overlap in blue, and corrosion product in red, with 3D image inset after 168 hours AASS

Figure 66 shows a 2D cross-section of the of the “Corrosion indicator 1” site from Figure 65.

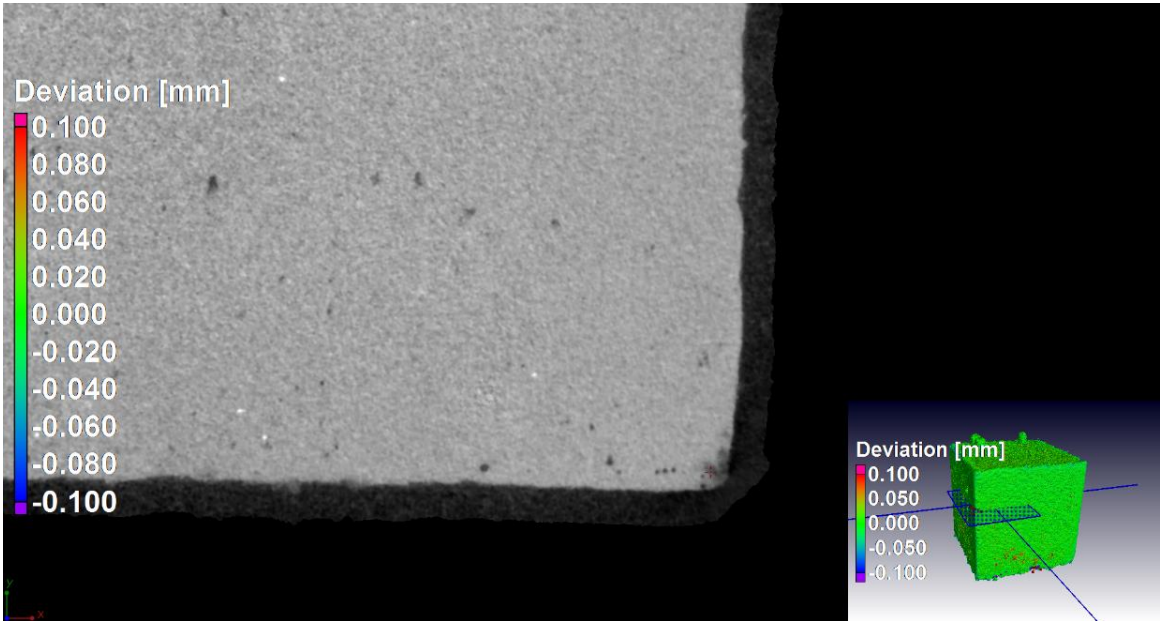


Figure 66: A 2D cross section from the E1 sample at “Corrosion indicator 1” site after 168 hours AASS

Figure 67 shows the 2D cross-section of the of the “Corrosion indicator 2” site from Figure 65.

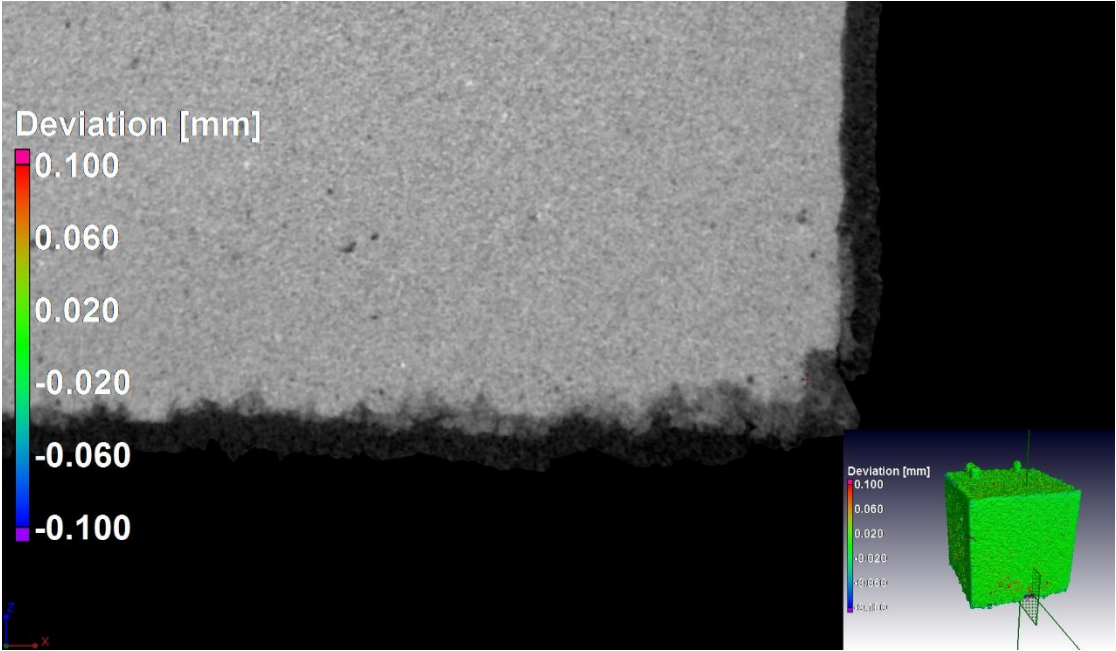


Figure 67: A 2D cross section from the E1 sample at “Corrosion indicator 2” site after 168 hours AASS

Figure 68 gives a comparison of a cross-section before and after corrosion, showing the corrosion and corrosion product, for the lowest laser power (E1).

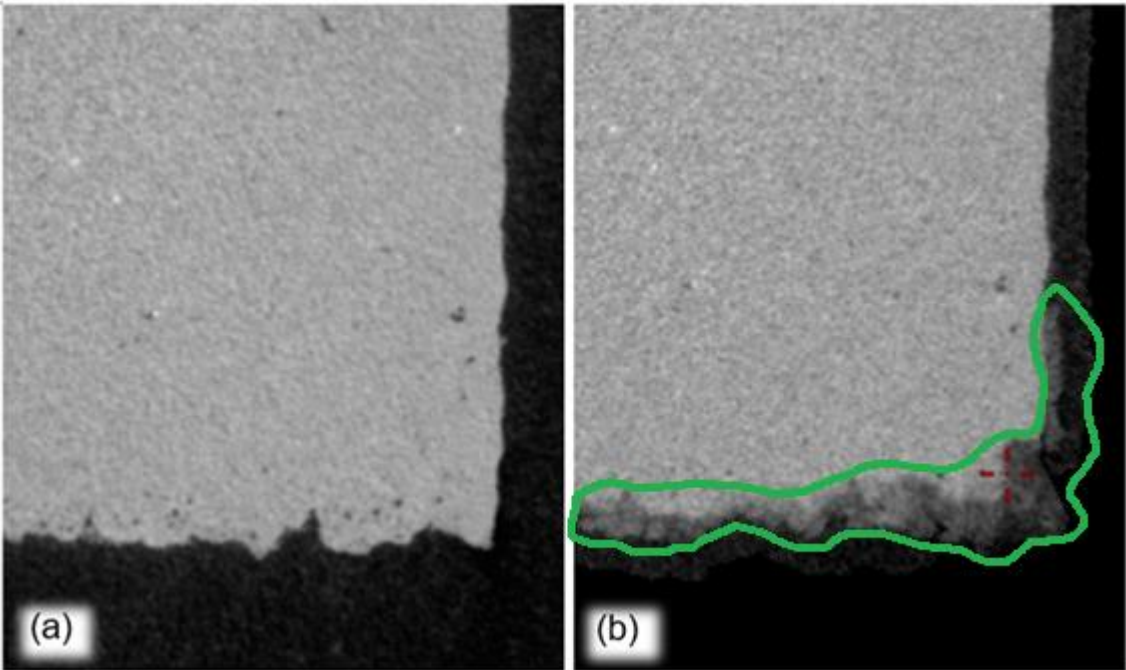


Figure 68: Comparison cross-section for E1 with (a) before and (b) after AASS corrosion (outlined) (AASS for 168 hours)

In Figure 69 it is seen that there is slightly more corrosion for the second lowest laser power (E2).

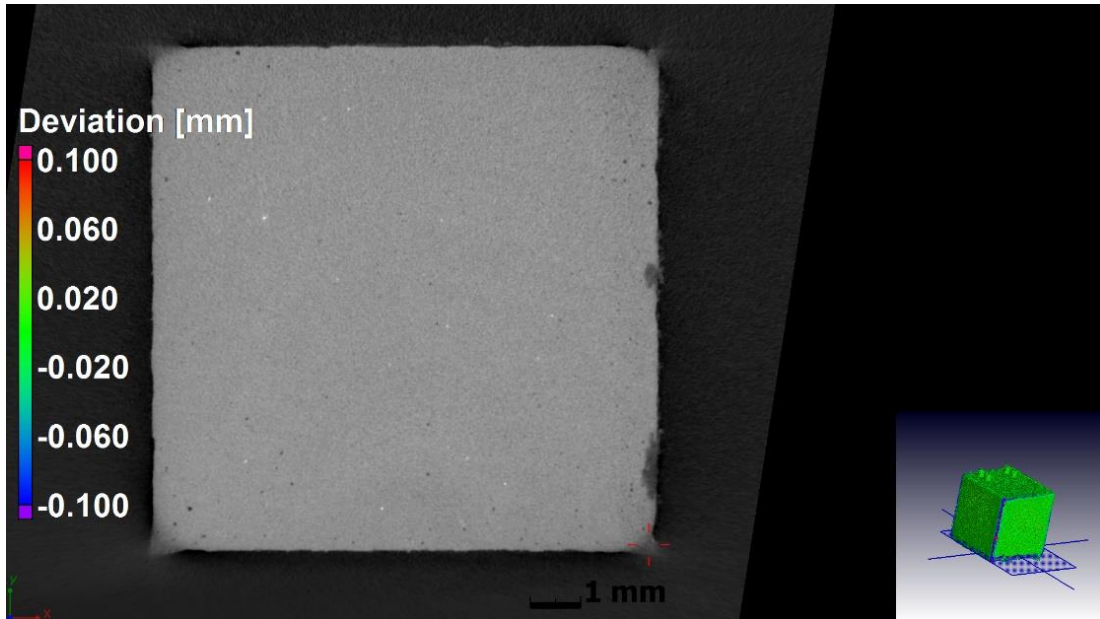


Figure 69: Corrosion slice image of sample from second lowest laser power (E2), with 3D image inset (AASS for 168 hours)

Figure 70 shows a comparison for the second lowest laser power (E2) for before and after corrosion.

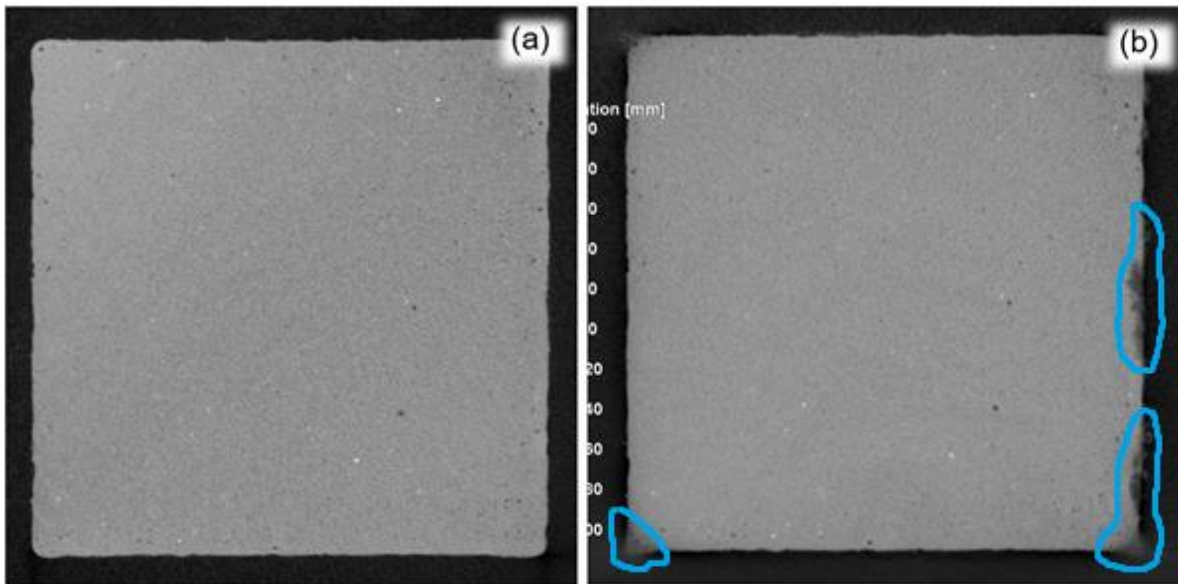


Figure 70: Comparison cross-section for E2 with (a) before and (b) after AASS corrosion (outlined) (AASS for 168 hours)

For the middle laser power (E3), significantly more corrosion took place, as seen in Figure 71.

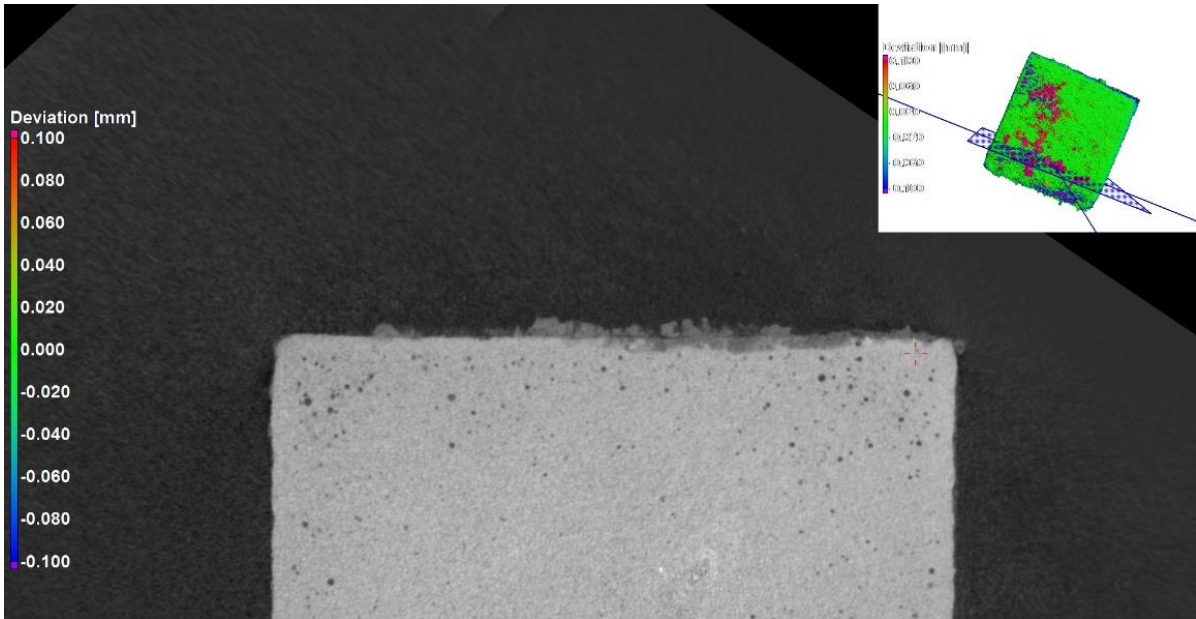


Figure 71: Corrosion slice image of sample from middle laser power (E3), with 3D image inset (AASS for 168 hours)

This is compared to the before slice image in Figure 72.

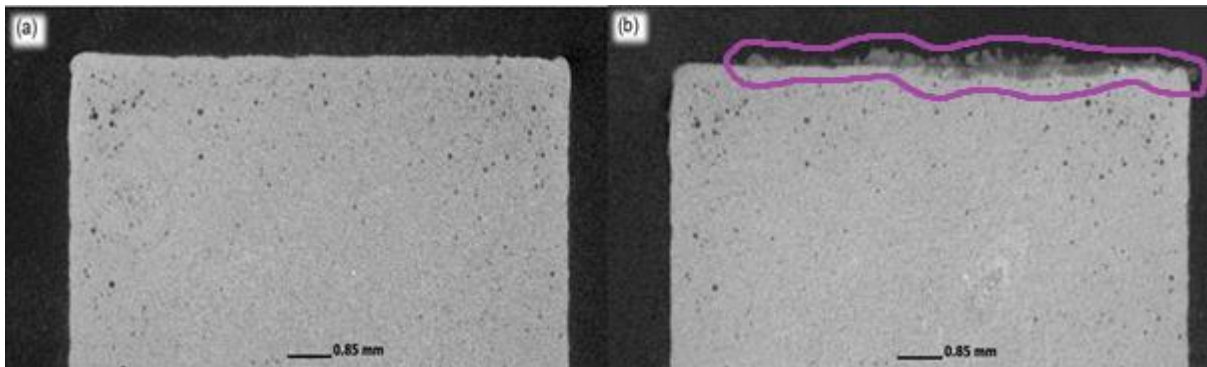


Figure 72: Comparison cross-section for E3 with (a) before and (b) after AASS corrosion (outlined) (AASS for 168 hours)

The second highest laser power (E4) has less corrosion product, but shows a bigger corroded area (blue regions), as shown in Figure 73.

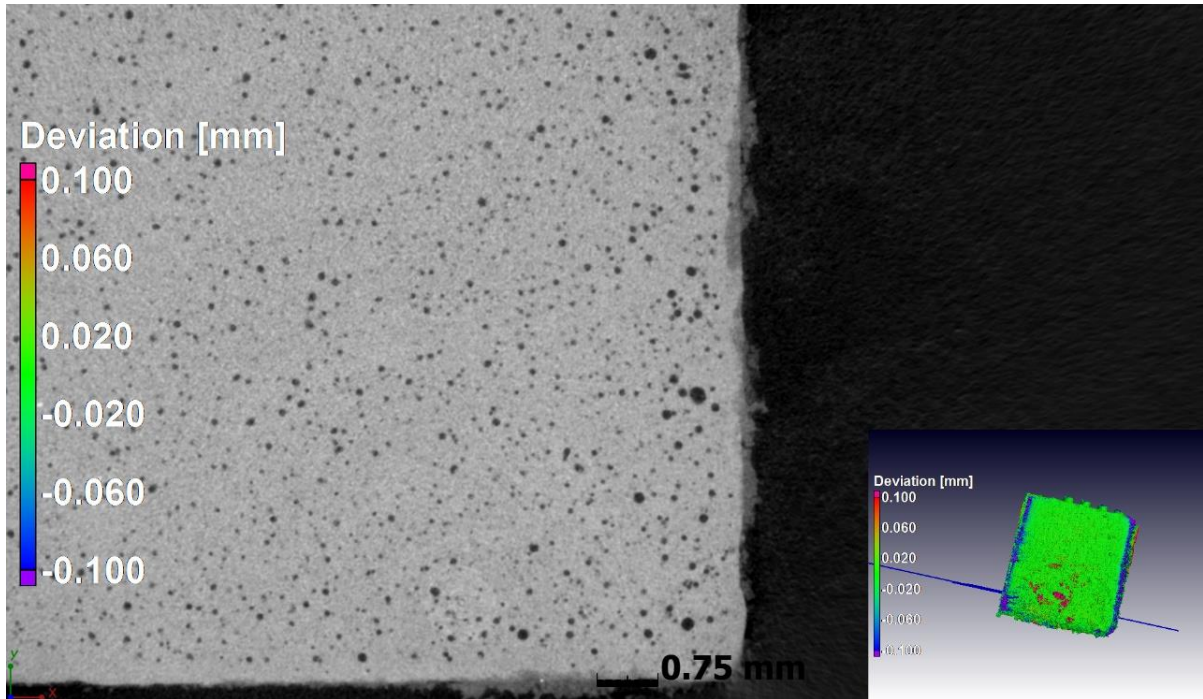


Figure 73: Corrosion slice image of sample from second highest laser power (E4) (AASS for 168 hours)

The before and after corrosion slice comparison is shown in Figure 74, for one corner of the sample.

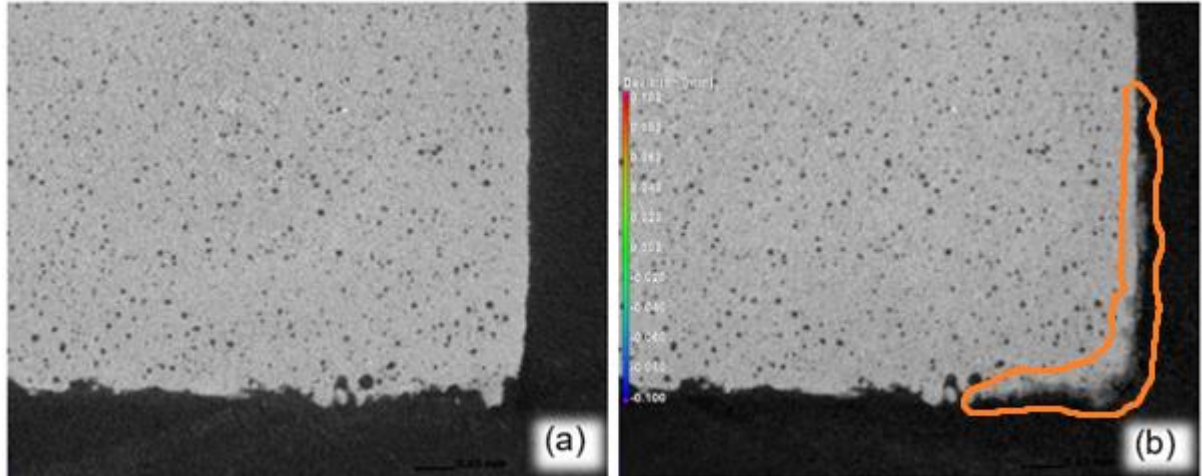


Figure 74: Comparison cross-section for E4 with (a) before and (b) after AASS corrosion (outlined) (AASS for 168 hours)

Another comparison is shown in Figure 75, where it can be seen that corrosion occurred mainly on two sides of the sample, with slight corrosion on the other sides.

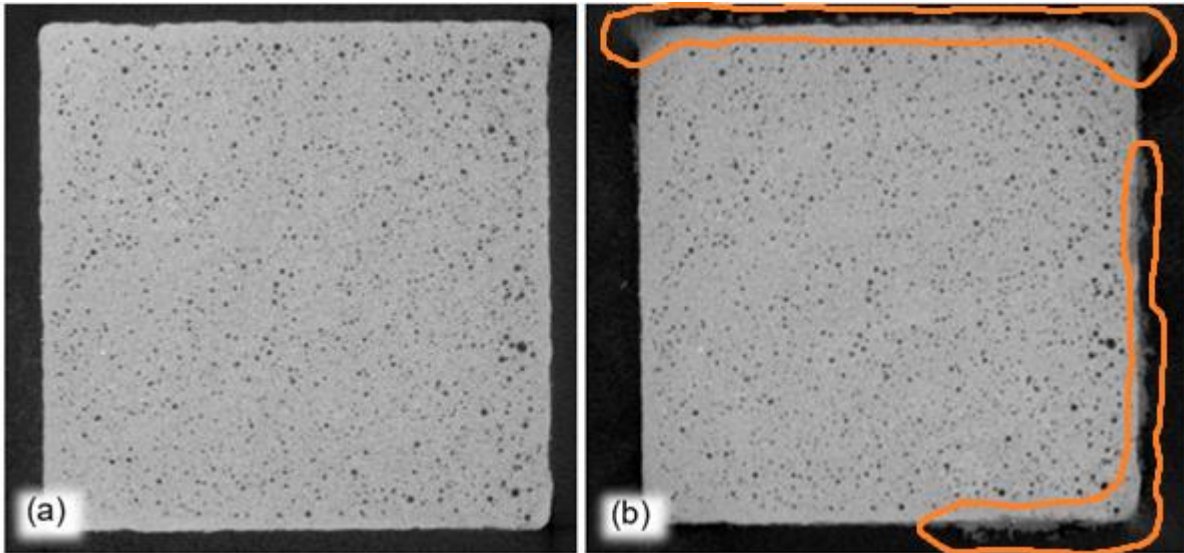


Figure 75: Another comparison cross-section for E4 with (a) before and (b) after AASS corrosion (outlined) (AASS for 168 hours)

The highest laser power (E5) shows some corrosion product, with less corroded regions than for E4. This is evident in Figure 76.

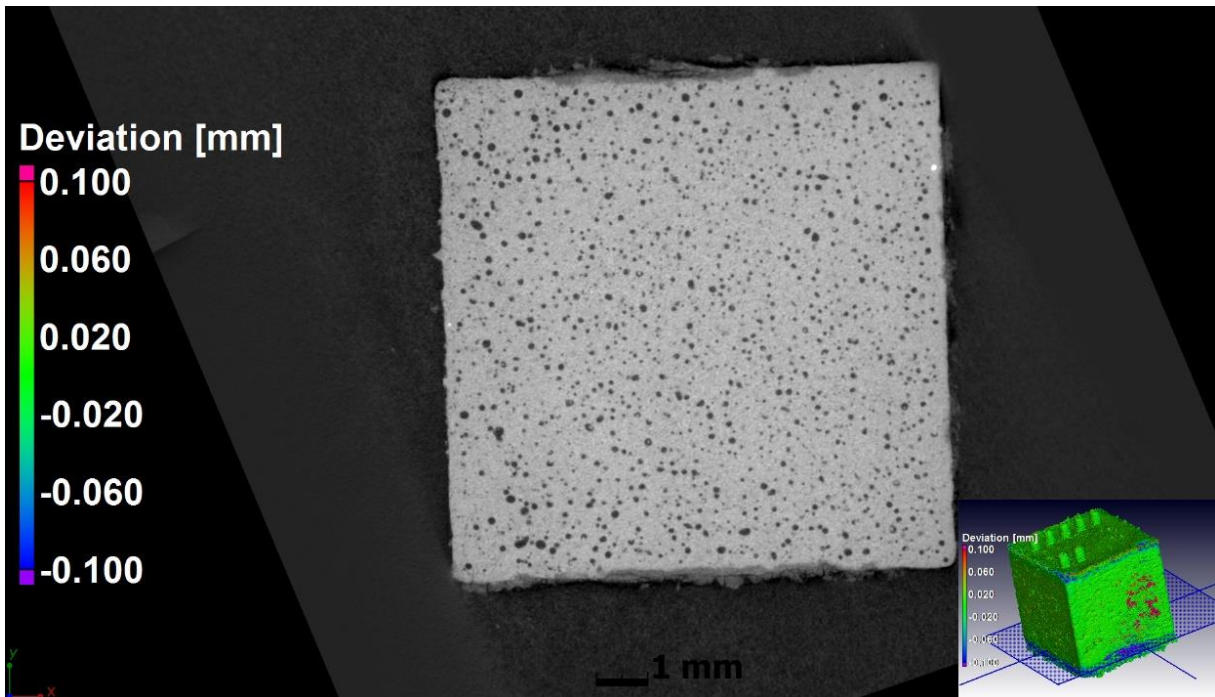


Figure 76: Corrosion slice image of sample from highest laser power (E5) (AASS for 168 hours)

Figure 77 shows a comparison for before and after corrosion for the highest laser power (E5), where it is again seen that corrosion mainly occurred on two sides, with some corrosion on a third side.

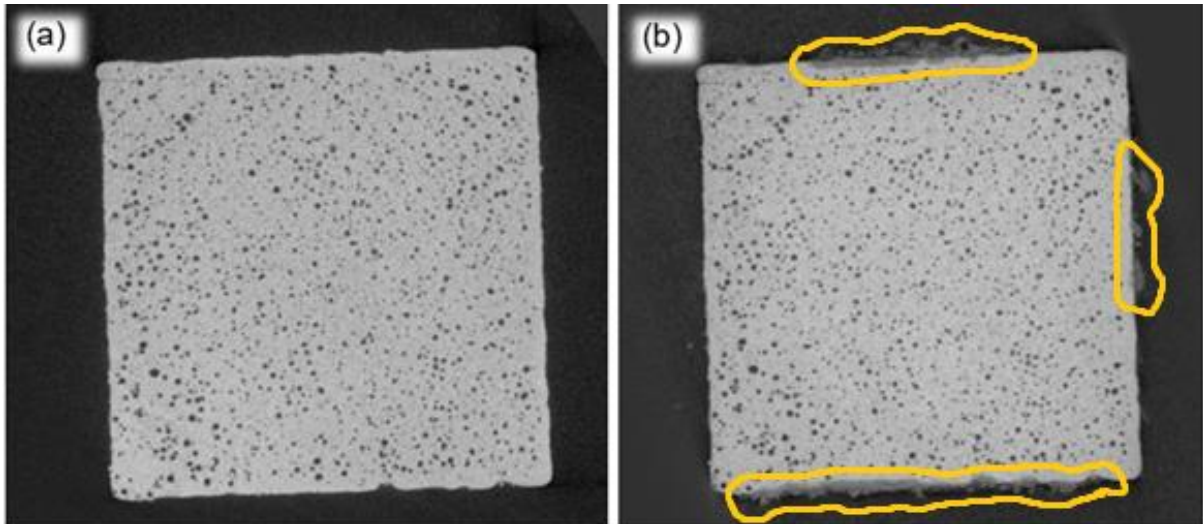


Figure 77: Comparison cross-section for E5 with (a) before and (b) after AASS corrosion (outlined) (AASS for 168 hours)

Figure 78 shows a close-up slice comparison for before and after corrosion for E5.

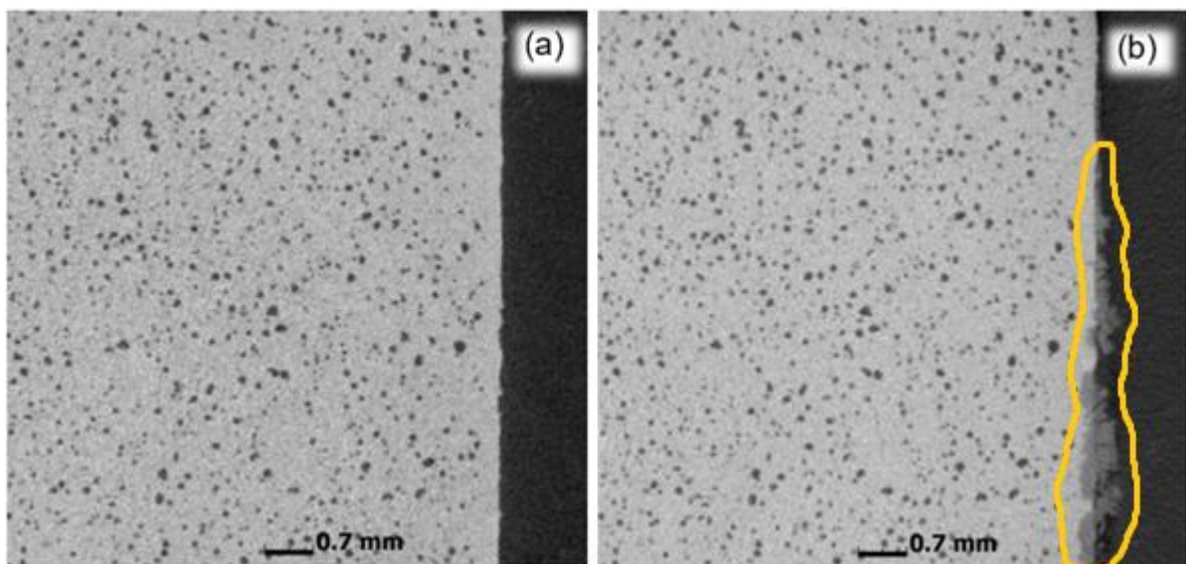


Figure 78: Another comparison cross-section for E5 with (a) before and (b) after AASS corrosion (outlined) (AASS for 168 hours)

8.1.2 Lattice cubes

Figure 79 shows NanoCT slice images for the lowest laser power, E1. The slices are before and after corrosion exposure (AASS for 168 hours) comparisons. The corrosion product appears more in the cavities near the edges of the lattice, rather than in the centre. As shown in the small 3D insert, the slice image comparison was done at the bottom edge of the lattice.

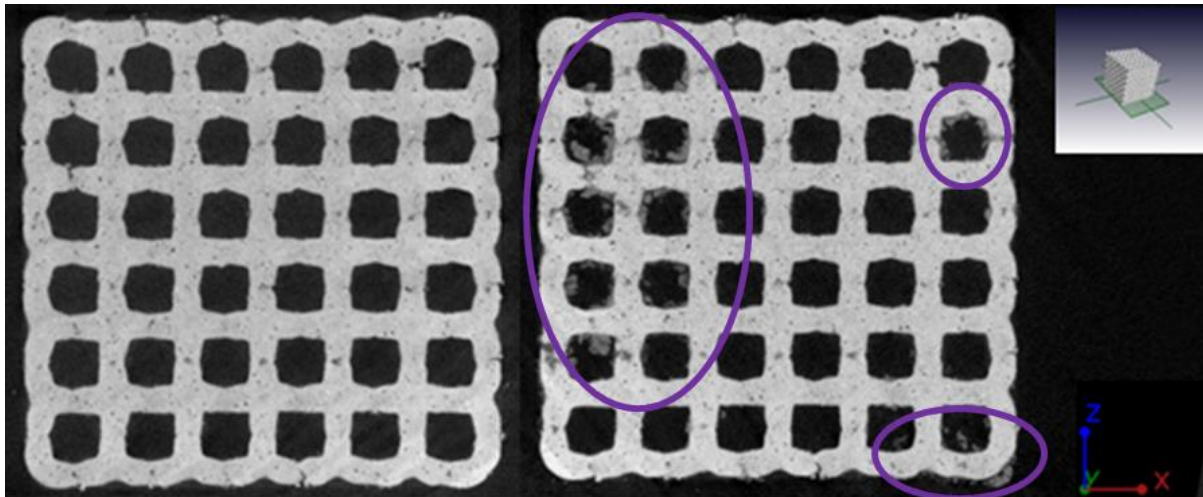


Figure 79: NanoCT slice image comparison before and after corrosion exposure for E1 (AASS for 168 hours)

Figure 80 shows before and after corrosion slice image comparisons for the highest laser power, E5.

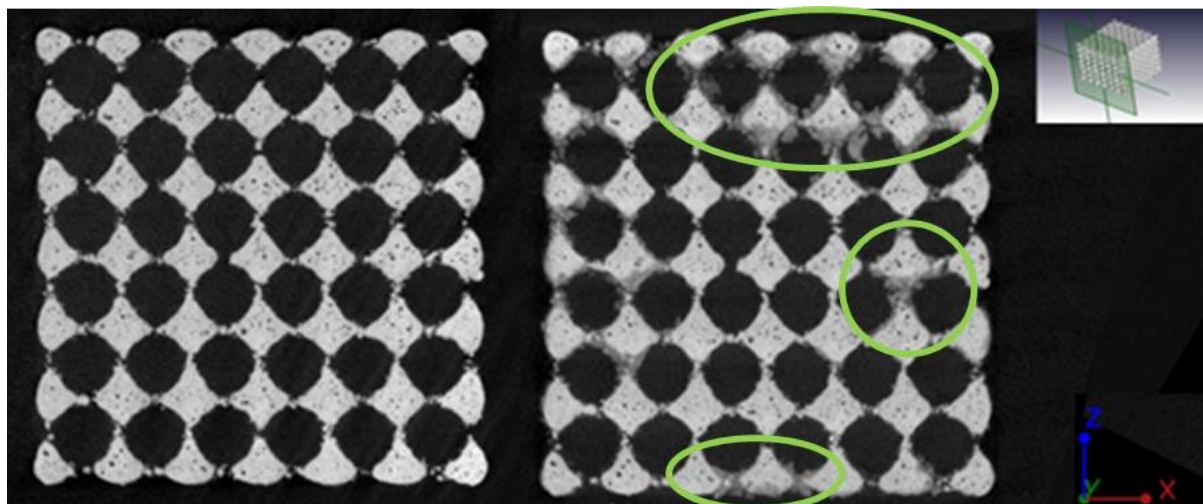


Figure 80: NanoCT slice image comparison before and after corrosion exposure for E5 (AASS for 168 hours)

These slice image comparisons for both E1 and E5 show that the corrosion did not occur preferentially at any particular location. It is also clearly seen how corrosion product has formed in the cavities of the lattice structure. The corrosion product is discussed in Chapter IV: Section [8.2](#), where XRD suggests the presence of amorphous compounds. As discussed in Chapter II: [8.3](#), the volume ratio of corrosion product to corroded metal is quite high at 6.5. This is seen in these samples, where there is a substantial amount of corrosion product, but careful inspection shows negligible signs of corroded metal. So the corrosion for up to 168 h was not strongly influenced by the different parameters leading to different porosity contents and surface conditions. Such CT before/after scans have not been reported for corrosion of metal AM to date.

8.2 Corrosion product analysis

The corrosion product that formed was white and powdery. However, before it completely dried, it appeared as shown in Figure 81. It can be seen that it appears gelatinous.



Figure 81: Corrosion product that formed on a top surface after 168 hours in AASS test

As it dried, it started to appear more like what can be seen in Figure 82. It looks less viscous, but still not fully solid.

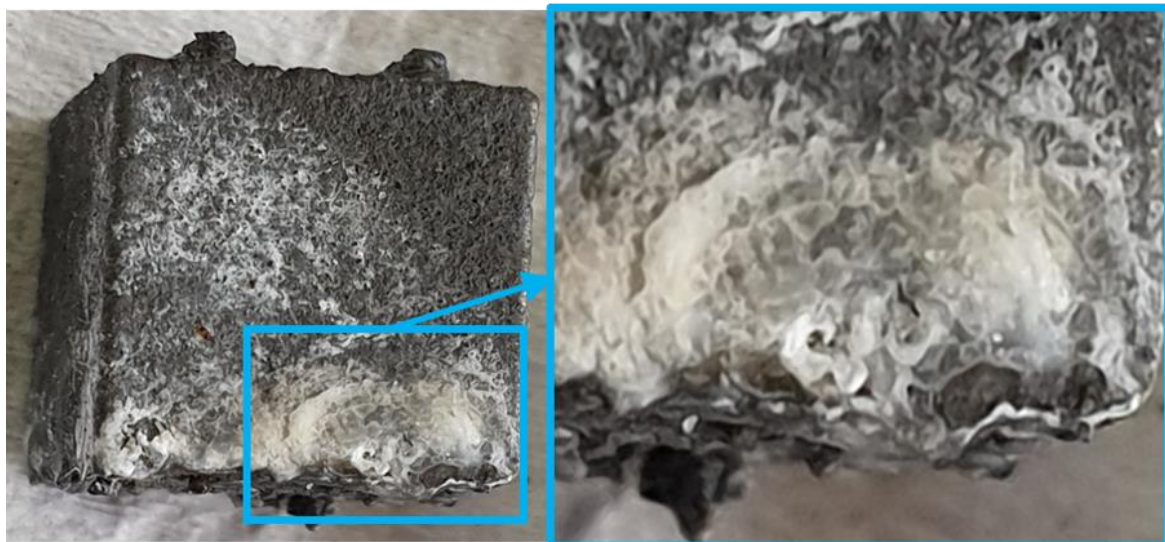


Figure 82: Corrosion product that formed on a side surface after 168 hours in AASS test

When the corrosion product fully dried out, it was chalky in texture. This is shown in Figure 83. The corrosion product was carefully scraped off so as to minimise or exclude substrate in the powder sample.

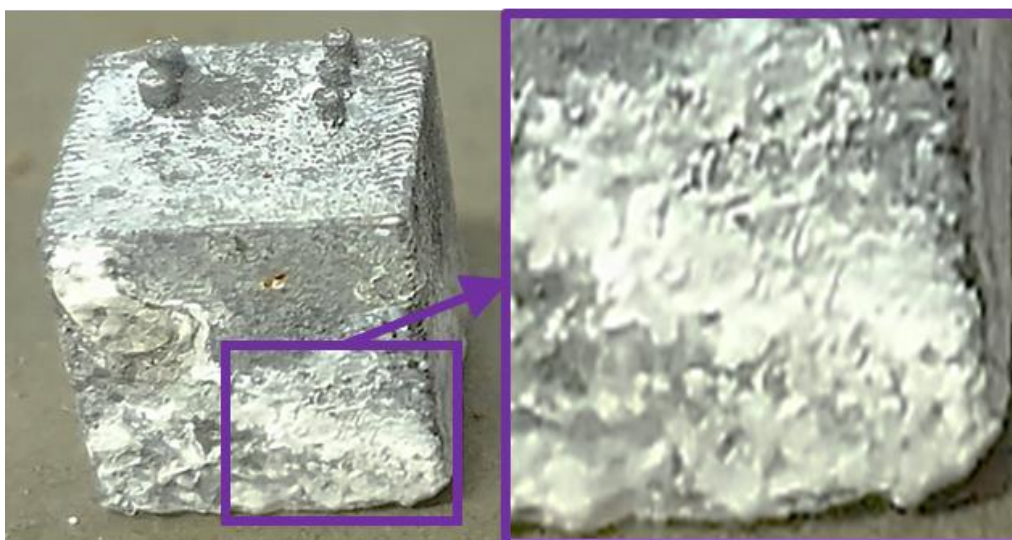


Figure 83: Dried corrosion product that formed on a side surface after 168 hours in AASS test

The corrosion product that was scraped off was analysed using SEM-EDS as well as XRD analysis. The SEM-EDS results showed high levels of oxygen (O), moderate levels of chlorine (Cl) and low levels of magnesium (Mg) and no sodium (Na). However, XRD did not pick up any traces of oxides, hydroxides or chlorides. This suggests that the corrosion product is amorphous, as XRD can only pick up crystalline phases. This is in line with what was discussed by [Gustafsson](#) [80], [Leygraf](#) et. al. [92] and [Vargel](#) [93], who all describe the initial $\text{Al}(\text{OH})_3$ as an amorphous product. It will be amorphous initially, due to containing large amounts of water which hydrate it, as described in Chapter II: Section [8.3](#). The dried powder seen here is in line with what is discussed in the aforementioned [section](#) [93].

Initial SEM-EDS and XRD results suggest the presence of oxides or hydroxides of aluminium. With SEM-EDS different areas were analysed to build a better picture. Several regions had more than two (2) times the amount of oxygen (O) than aluminium (Al). The powder submitted for XRD analysis yielded no phase results, only elemental aluminium and silicon. The raw data graph for XRD is shown in Figure 84.

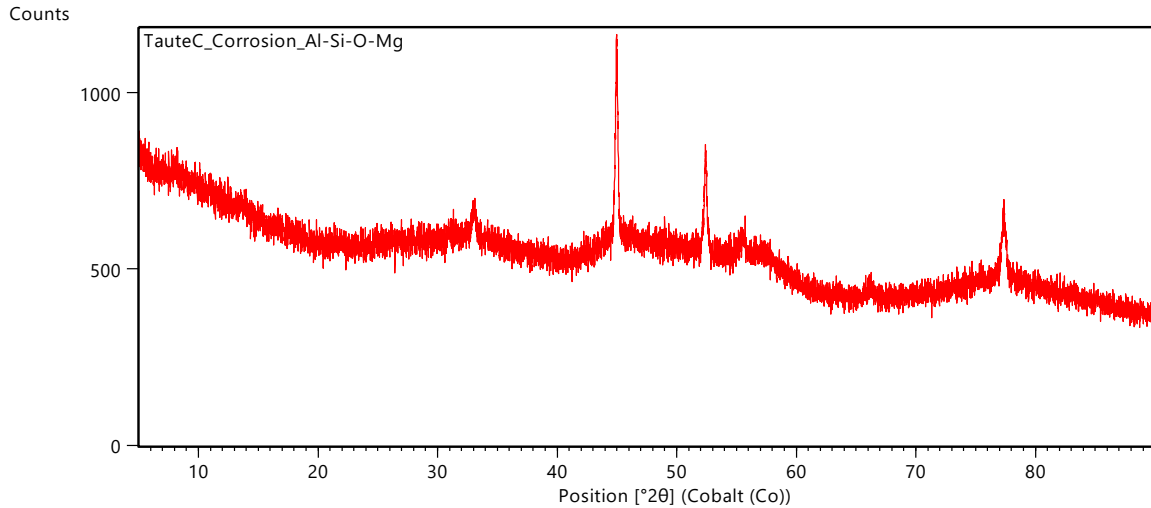


Figure 84: Raw XRD data

The three (3) sharp peaks correspond to Al, as shown in Figure 85, which are the finalised results. The Si peaks are smaller, but still visible, due to lower peak intensity.

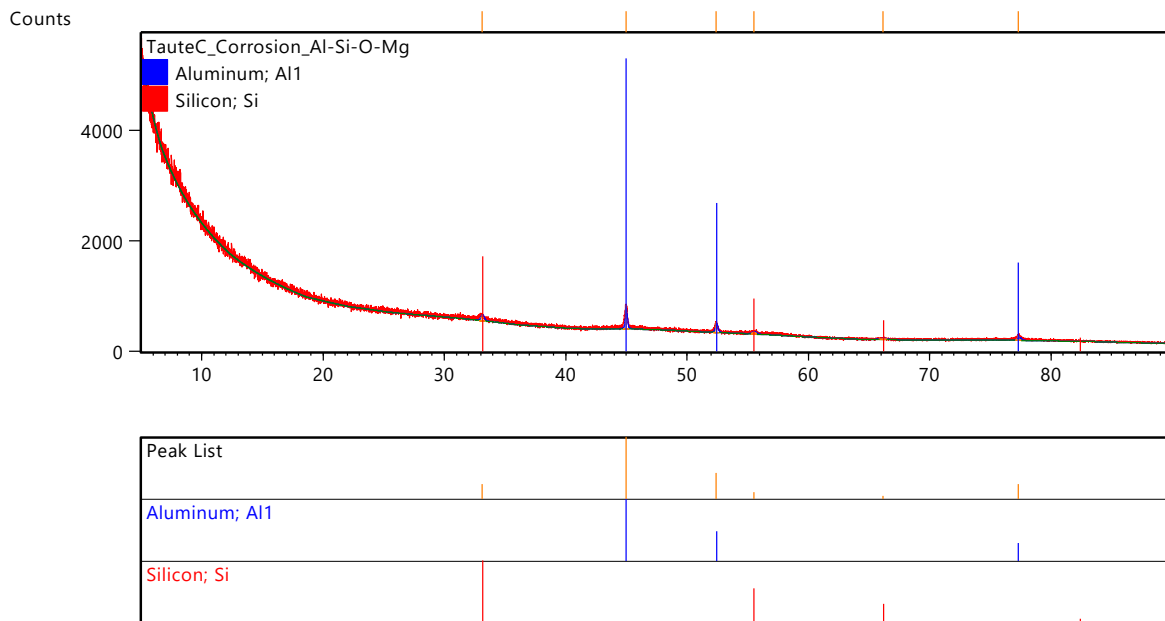


Figure 85: Finalised XRD data

As XRD is used to determine crystalline phases present in a sample it is only sensitive to those phases. It cannot detect amorphous compounds. This coupled with the SEM-EDS elemental results are what suggests the presence of amorphous oxides or hydroxides, coupled with the literature by [Gustafsson](#) [80], [Leygraf](#) et. al. [92] and [Vargel](#) [93].

8.3 Compression testing

Figure 86 shows the compressive yield strength vs laser power for before corrosion exposure, after the neutral salt spray (NSS) and after the acetic acid salt spray (AASS).

The graph shows the general trend for all three situations as columns with data labels, to easily compare the actual values in line with the visual trend.

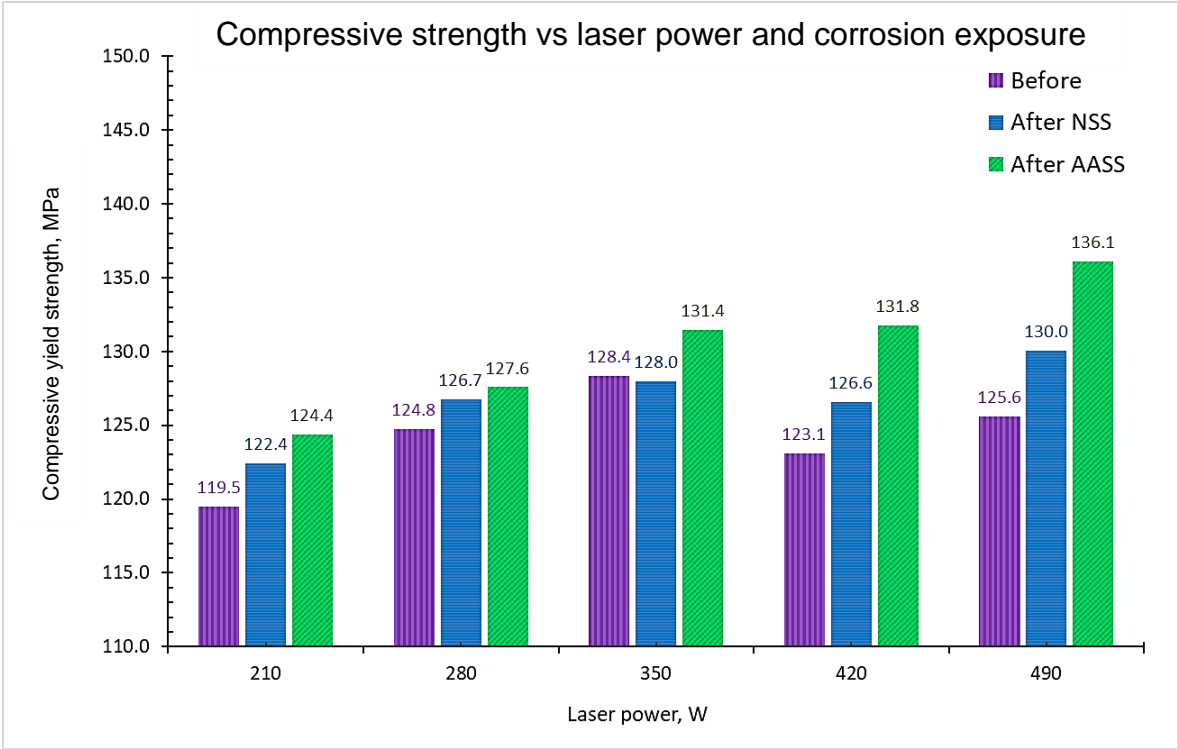


Figure 86: Compressive yield strength versus laser power, before and after corrosion, with data labels, lattice structures

It can be seen that the compressive yield strength (maximum compressive stress reached at the peak of the initial linear elastic region, as indicated in Figure 62) varies slightly between laser powers, as well as after each corrosion test.

The actual values show a difference of 8.9 MPa between the maximum and minimum compressive strengths before corrosion, 7.6 MPa for after NSS and 11.7 MPa after AASS. The higher difference after AASS compared to NSS can also be attributed to more corrosion product present in those lattices than in the NSS lattices.

The possibility is that crack initiation sites are filled with corrosion product, delaying the onset of cracking and failure. The corrosion product in the cavities will have a higher compressive strength compared to no strength of the air in the void for the non-corroded structure. It is therefore probable that the compressive strength of the corrosion product adds to the full strength of the lattice, compared to that of the non-corroded structure.

Figure 63 showed that the NSS test formed small amounts of corrosion product, and that the AASS test formed significantly more (Figure 64). This is correlated in the graph in Figure 86, where more corrosion product is linked to slightly higher compressive strength. It is improbable that the effect of corrosion product delaying onset of cracking in a compression test will be the same for a tensile test. The compression test effectively pushes corrosion product into the cavities, whereas a tensile test pulls the sample apart. For a tensile test it is more likely that the corrosion product will have less of an effect than the areas of the sample degraded by the corrosion exposure.

CHAPTER V: CONCLUSIONS

Corrosion product within pores is seen clearly in CT scans and can be visualized with aligned CT images of before-after states, which has not been reported yet for corrosion of metal AM. The presence of porosity does not seem to affect the progression of corrosion during the early corrosion stages. This implies that the alloy can delay corrosion (specifically saltspray) with some pores present. The corrosion is not evenly distributed but more on side surfaces and rough downskin surface than on the top surface. The process parameters did not strongly affect the corrosion, despite differences in porosity and surface conditions. The parameters also did not strongly affect the microstructure, as it was similar across all the laser power sets.

It is seen that not much corrosion took place, but with slightly more corrosion product in the keyhole-mode samples with higher power (E5) compared to low power (lack of fusion regime, E1). While this is interesting, the main result is that porosity does not seem to affect corrosion in the early stages of corrosion (first 168 hours). It might affect the progression of corrosion later on.

CT scans clearly show some corrosion when before-after slice images are aligned. The corrosion does not take place homogeneously over the samples. They also clearly show more corrosion product formed after AASS than after NSS.

It is probable that crack initiation sites such as internal porosity and defects are filled with corrosion product, delaying the onset of cracking and failure, and the corrosion product that fill the voids adding to the full strength of the lattice will also slightly increase the compressive strength of the samples.

1. Recommendations

Further investigation is required to determine the full effect of corrosion after the first seven (7) days. It is recommended that:

- (a) Corrosion testing is carried out for a period longer than 168 hours.
- (b) A larger sample size is used to have more samples per laser power set for compression testing to gain a more representative average.
- (c) The larger sample size should include extra samples for corrosion testing as well as elemental analysis and mechanical tests such as hardness, again to gain a more representative average.
- (d) The corrosion product should be analysed in-depth with techniques such as Fourier-transform infrared spectroscopy (FTIR) or Raman to determine what exactly it is.
- (e) Further in-depth CT scans to verify whether there was more corrosion product formed at higher laser powers.
- (f) Polarisation studies to determine pitting and repassivation potentials as a function of sample porosity% and surface roughness.

BIBLIOGRAPHY

- [1] T. DebRoy, H.L. Wei, J.S. Zuback, T. Mukherjee, J.W. Elmer, J.O. Milewski, A.M. Beese, A. Wilson-Heid, A. De, W. Zhang, Additive manufacturing of metallic components – Process, structure and properties, *Prog. Mater. Sci.* 92 (2018) 112–224. <https://doi.org/10.1016/j.pmatsci.2017.10.001>.
- [2] ASTM.52900:2015, Standard Terminology for Additive Manufacturing – General Principles – Terminology, 2015. <https://doi.org/10.1520/F2792-12A.2>.
- [3] M. Cabrini, F. Calignano, P. Fino, S. Lorenzi, M. Lorusso, D. Manfredi, C. Testa, T. Pastore, Corrosion behavior of heat-treated AlSi10Mg manufactured by laser powder bed fusion, *Materials (Basel)*. 11 (2018) 1–18. <https://doi.org/10.3390/ma11071051>.
- [4] N.T. Aboulkhair, N.M. Everitt, I. Ashcroft, C. Tuck, Reducing porosity in AlSi10Mg parts processed by selective laser melting, *Addit. Manuf.* 1 (2014) 77–86. <https://doi.org/10.1016/j.addma.2014.08.001>.
- [5] M. Rafieezad, M. Mohammadi, A. Gerlich, A. Nasiri, Enhancing the corrosion properties of additively manufactured AlSi10Mg using friction stir processing, *Corros. Sci.* 178 (2021) 109073. <https://doi.org/10.1016/j.corsci.2020.109073>.
- [6] Renishaw, Datasheet: AlSi10Mg-0403 powder for additive manufacturing, (2015) 2. <http://resources.renishaw.com/en/download/data-sheet-alsi10mg-0403-400-w-powder-for-additive-manufacturing--73122>.
- [7] N. Read, W. Wang, K. Essa, M.M. Attallah, Selective laser melting of AlSi10Mg alloy: Process optimisation and mechanical properties development, *Mater. Des.* 65 (2015) 417–424. <https://doi.org/10.1016/j.matdes.2014.09.044>.
- [8] J.R. Davis, Alloy and Temper Designation Systems, in: J.R. Davis (Ed.), *ASM Spec. Handb. Alum. Alum. Alloy.*, ASM International, United States, 1993: pp. 18–31.
- [9] S. Bremen, W. Meiners, A. Diatlov, Selective Laser Melting, *Laser Tech. J.* 9 (2012) 33–38. <https://doi.org/10.1002/latj.201290018>.
- [10] S. Kumar, Selective Laser Sintering/Melting, in: *Compr. Mater. Process.*, Elsevier, 2014: pp. 93–134. <https://doi.org/10.1016/B978-0-08-096532-1.01003-7>.
- [11] C.Y. Yap, C.K. Chua, Z.L. Dong, Z.H. Liu, D.Q. Zhang, L.E. Loh, S.L. Sing, Review of selective laser melting: Materials and applications, *Appl. Phys. Rev.* 2 (2015) 041101. <https://doi.org/10.1063/1.4935926>.
- [12] A.M. Philo, C.J. Sutcliffe, S.A. Sillars, J. Siens, A.M. Philo, C.J. Sutcliffe, S. Sillars, S.G.R. Brown, N.P. Lavery, A STUDY INTO THE EFFECTS OF GAS FLOW INLET DESIGN OF THE RENISHAW AM250 LASER POWDER BED FUSION MACHINE USING COMPUTATIONAL MODELLING Swansea Additive Manufacturing Research View project Investigation into near-infrared process technology for coated-steel, *Solid Free. Fabr. 2017 Proc. 28th Annu. Int.* (2017) 1203–1219. <https://www.researchgate.net/publication/321748261>.
- [13] S.K. Everton, P. Dickens, C. Tuck, B. Dutton, Identification of Sub-Surface Defects in Parts Produced by Additive Manufacturing, Using Laser Generated

- Ultrasound, in: Mater. Sci. Technol. Conf. Exhib., Salt Lake City, 2016: pp. 141–148.
- [14] B. Zhang, Y. Li, Q. Bai, Defect Formation Mechanisms in Selective Laser Melting: A Review, *Chinese J. Mech. Eng. (English Ed.)* 30 (2017) 515–527. <https://doi.org/10.1007/s10033-017-0121-5>.
- [15] M. Tang, Inclusions, porosity, and fatigues of AlSi10Mg parts produced by selective laser melting, Carnegie Mellon University, 2017. <http://repository.cmu.edu/dissertations/903>.
- [16] M. Tang, P.C. Pistorius, J.L. Beuth, Prediction of lack-of-fusion porosity for powder bed fusion, *Addit. Manuf.* 14 (2017) 39–48. <https://doi.org/10.1016/j.addma.2016.12.001>.
- [17] A. du Plessis, Effects of process parameters on porosity in laser powder bed fusion revealed by X-ray tomography, *Addit. Manuf.* 30 (2019). <https://doi.org/10.1016/j.addma.2019.100871>.
- [18] J.G. Kaufman, E.L. Rooy, Aluminum Casting Alloys, in: J.G. Kaufman (Ed.), *Alum. Alloy Cast. Prop. Process. Appl.*, ASM International, 2004: p. 10.
- [19] N.T. Aboulkhair, I. Maskery, C. Tuck, I. Ashcroft, N.M. Everitt, The microstructure and mechanical properties of selectively laser melted AlSi10Mg: The effect of a conventional T6-like heat treatment, *Mater. Sci. Eng. A.* 667 (2016) 139–146. <https://doi.org/10.1016/j.msea.2016.04.092>.
- [20] N.T. Aboulkhair, C. Tuck, I. Ashcroft, I. Maskery, N.M. Everitt, On the Precipitation Hardening of Selective Laser Melted AlSi10Mg, *Metall. Mater. Trans. A Phys. Metall. Mater. Sci.* 46 (2015) 3337–3341. <https://doi.org/10.1007/s11661-015-2980-7>.
- [21] K. Kempen, L. Thijs, J. Van Humbeeck, J.P. Kruth, Mechanical Properties of AlSi10Mg Produced by Selective Laser Melting, *Phys. Procedia.* 39 (2012) 439–446. <https://doi.org/10.1016/j.phpro.2012.10.059>.
- [22] T.B. Sercombe, X. Li, Selective laser melting of aluminium and aluminium metal matrix composites: Review, *Mater. Technol.* 31 (2016) 77–85. <https://doi.org/10.1179/1753555715Y.0000000078>.
- [23] W. Li, S. Li, J. Liu, Y. Zhou, Q. Wei, C. Yan, Y. Shi, Effect of heat treatment on AlSi10Mg alloy fabricated by selective laser melting: Microstructure evolution, mechanical properties and fracture mechanism, *Mater. Sci. Eng. A.* 663 (2016) 116–125. <https://doi.org/10.1016/j.msea.2016.03.088>.
- [24] W. Stumpf, Dislocations and deformation, in: W. Stumpf (Ed.), *Mech. Metall.*, University of Pretoria, Pretoria, 2018: pp. 2.7.12-14.
- [25] S.H. Whang, Introduction, in: S.H. Whang (Ed.), *Nanostructured Met. Alloy. Process. Microstruct. Mech. Prop. Appl.*, Woodhead Publishing, 2011: pp. xxi–xxxv. <https://doi.org/10.1016/B978-1-84569-670-2.50028-9>.
- [26] A.H. Maamoun, M. Elbestawi, G.K. Dosbaeva, S.C. Veldhuis, Thermal post-processing of AlSi10Mg parts produced by Selective Laser Melting using recycled powder, *Addit. Manuf.* 21 (2018) 234–247. <https://doi.org/10.1016/j.addma.2018.03.014>.

- [27] A. Saronic, Conventional heat treatment of additively manufactured AlSi10Mg, Luleå University of Technology, 2019. <http://www.diva-portal.org/smash/get/diva2:1331589/FULLTEXT01.pdf>.
- [28] J.R. Davis, Physical Metallurgy - Strengthening mechanisms, in: J.R. Davis (Ed.), ASM Spec. Handb. Alum. Alum. Alloy., ASM International, United States, 1993: p. 35.
- [29] SLM Solutions, MDS Al-Alloy AlSi10Mg, (2021) 5. https://www.slm-solutions.com/fileadmin/Content/Powder/MDS/MDS_Al-Alloy_AlSi10Mg_0221.pdf.
- [30] I. Rosenthal, A. Stern, Heat treatment investigation of the AlSi10Mg alloy produced by selective laser melting (SLM): Microstructure and hardness, Ann. "Dunarea Jos" Univ. Galati, Fascicle XII, Weld. Equip. Technol. 27 (2016) 7–11.
- [31] 3T Additive Manufacturing, Aluminium AlSi10Mg Aluminium AlSi10Mg, 3T AM. (2021) 2. https://www.3t-am.com/sites/threeT/files/Aluminium_AlSi10Mg_Datasheet_0.pdf.
- [32] EOS GmbH - Electro Optical Systems, EOS Aluminium AlSi10Mg, GPI Prototype Manuf. Serv. 49 (2014) 1–5. https://gpiprototype.com/pdf/EOS_Aluminium_AlSi10Mg_en.pdf.
- [33] Zare, Material Data Sheet, DMLS/SLM technology, Aluminium AlSi10Mg, (2014) 1. https://www.zare.it/sites/default/files/manuals/DMLS-SLM-Aluminium-AlSi10Mg_0.pdf.
- [34] R. Lumley, CSIRO Light Metals Flagship: Technical data sheets for heat treated aluminium high pressure die castings, Victoria, Australia, 2008. http://mastersonics.com/documents/mmm_applications/ultrasonic_metallurgy/pio2-hpdc-aluminum.pdf.
- [35] X. Xing, X. Duan, T. Jiang, J. Wang, F. Jiang, Ultrasonic peening treatment used to improve stress corrosion resistance of AlSi10Mg components fabricated using selective laser melting, Metals (Basel). 9 (2019). <https://doi.org/10.3390/met9010103>.
- [36] A.A. Raus, M.S. Wahab, M. Ibrahim, K. Kamarudin, A. Ahmed, S. Shamsudin, Mechanical and Physical Properties of AlSi10Mg Processed through Selective Laser Melting, Int. J. Eng. Technol. 8 (2017) 2612–2618. <https://doi.org/10.21817/ijet/2016/v8i6/160806217>.
- [37] K. Zygula, B. Nosek, H. Pasiowiec, N. Szysiak, Mechanical properties and microstructure of AlSi10Mg alloy obtained by casting and SLM technique, 104 (2018) 462–472.
- [38] A. Mertens, O. Dedry, D. Reuter, O. Rigo, J. Lecomte-Beckers, Thermal Treatments of AlSi10Mg Processed by Laser Beam Melting, in: 26th Int. Solid Free. Fabr. Symp., Austin, Texas, 2015: pp. 1007–1016. https://www.researchgate.net/publication/282291789_THERMAL_TREATMENTS_OF_ALSi10Mg_PROCESSED_BY_LASER_BEAM_MELTING.
- [39] ASTM.E8/E8M-15a, Standard Test Methods for Tension Testing of Metallic Materials, 2015. https://doi.org/10.1520/E0008_E0008M-15A.

- [40] ISO 6892-1:2018, Metallic materials – Tensile testing, Part 1: Method of test at room temperature, 2016.
- [41] K. Kempen, L. Thijs, J. Van Humbeeck, J.P. Kruth, Processing AlSi10Mg by selective laser melting: Parameter optimisation and material characterisation, *Mater. Sci. Technol.* (United Kingdom). 31 (2015) 917–923. <https://doi.org/10.1179/1743284714Y.0000000702>.
- [42] Z. Ma, A.M. Samuel, H.W. Doty, F.H. Samuel, On the Fractography of Impact-Tested Samples of Al-Si Alloys for Automotive Alloys, in: L.M. Alves (Ed.), *Fract. Mech. - Prop. Patterns Behav.*, IntechOpen, 2016: p. 29. <https://doi.org/10.5772/63409>.
- [43] E.W. Hovig, A.S. Azar, M. Mhamdi, K. Sørby, Mechanical properties of AlSi10Mg processed by laser powder bed fusion at elevated temperature, in: *The Minerals Metals & Materials Society (Ed.), TMS 2020 149th Annu. Meet. Exhib. Suppl. Proc.*, 2020: pp. 395–404. https://doi.org/10.1007/978-3-030-36296-6_37.
- [44] GranuTools, The Importance Of Powder Flow Characterization, (2020). https://www.granutools.com/en/news/61_the-importance-of-powder-flow-characterization#:~:text=ls Powder Flow%3F-,Powder flow%2C also known as flowability%2C is defined as the,piece of equipment %5B2%5D.
- [45] O.D. Neikov, Atomization and Granulation, in: O.D. Neikov, S.S. Naboychenko, N.A. Yefimov (Eds.), *Handb. Non-Ferrous Met. Powders*, 2nd ed., Elsevier, 2019: p. 143.
- [46] L. Cordova, M. Campos, T. Tinga, Revealing the Effects of Powder Reuse for Selective Laser Melting by Powder Characterization, *Jom.* 71 (2019) 1062–1072. <https://doi.org/10.1007/s11837-018-3305-2>.
- [47] C. Yan, L. Hao, A. Hussein, S.L. Bubb, P. Young, D. Raymont, Evaluation of light-weight AlSi10Mg periodic cellular lattice structures fabricated via direct metal laser sintering, *J. Mater. Process. Technol.* 214 (2014) 856–864. <https://doi.org/10.1016/j.jmatprotec.2013.12.004>.
- [48] H.K. Rafi, N. V. Karthik, H. Gong, T.L. Starr, B.E. Stucker, Microstructures and mechanical properties of Ti6Al4V parts fabricated by selective laser melting and electron beam melting, *J. Mater. Eng. Perform.* 22 (2013) 3872–3883. <https://doi.org/10.1007/s11665-013-0658-0>.
- [49] S. Liu, H. Guo, Balling Behavior of Selective Laser Melting (SLM) Magnesium Alloy, *Mater.* 13 (2020) 3632. <https://doi.org/10.3390/ma13163632>.
- [50] R. Lumley, Additive manufacturing of aluminium based alloys and composites, in: R. Lumley (Ed.), *Fundam. Alum. Metall. - Recent Adv.*, 1st ed., Woodhead Publishing, Australia, 2018: pp. 47–92.
- [51] A. du Plessis, J.M. Waller, Simple and standardized CT testing in metal Additive Manufacturing, *Met. Addit. Manuf.* 4 (2018) 87–96.
- [52] A. du Plessis, S.G. le Roux, Standardized X-ray tomography testing of additively manufactured parts: A round robin test, *Addit. Manuf.* 24 (2018) 125–136. <https://doi.org/10.1016/j.addma.2018.09.014>.
- [53] Mettler Toledo, Draft Shields, (2020) 2.

https://www.mt.com/sg/en/home/products/Laboratory_Weighing_Solutions/Accessories/weighing-pans-and-draft-shields/draft-shields.html.

- [54] W.W. Wits, S. Carmignato, F. Zanini, T.H.J. Vaneker, Porosity testing methods for the quality assessment of selective laser melted parts, *CIRP Ann. - Manuf. Technol.* 65 (2016) 201–204. <https://doi.org/10.1016/j.cirp.2016.04.054>.
- [55] A.B. Spierings, M. Schneider, R. Eggenberger, Comparison of density measurement techniques for additive manufactured metallic parts, *Rapid Prototyp. J.* 17 (2011) 380–386. <https://doi.org/10.1108/13552541111156504>.
- [56] Micromeritics, AccuPyc II 1345 Pycnometer, (2020) 3. <https://www.micromeritics.com/product-showcase/accupyc-ii-1340.aspx>.
- [57] A. du Plessis, I. Yadroitsava, I. Yadroitsev, Effects of defects on mechanical properties in metal additive manufacturing: A review focusing on X-ray tomography insights, *Mater. Des.* 187 (2020). <https://doi.org/10.1016/j.matdes.2019.108385>.
- [58] United States. Dept. of Defense, Military Standard, Issues 200-218, The Department., 2011. [https://books.google.co.za/books?id=RAco4TlrT54C&pg=PP59&dq=salt+spray+test+how&hl=en&sa=X&ved=2ahUKEwi8nqWp5_jvAhVBsXEKHUCYC8YQ6AEwA3oECAIQAg#v=onepage&q=salt spray test how&f=false](https://books.google.co.za/books?id=RAco4TlrT54C&pg=PP59&dq=salt+spray+test+how&hl=en&sa=X&ved=2ahUKEwi8nqWp5_jvAhVBsXEKHUCYC8YQ6AEwA3oECAIQAg#v=onepage&q=salt%20spray%20test%20how&f=false).
- [59] R. Baboian, Cabinet Tests, in: *Corros. Tests Stand. Appl. Interpret.*, ASTM International, 2005: p. 131. [https://books.google.co.za/books?id=8C7pXhnqje4C&pg=PA132&dq=salt+spray+test+how&hl=en&sa=X&ved=2ahUKEwi8nqWp5_jvAhVBsXEKHUCYC8YQ6AEwBXoECAMQAg#v=onepage&q=salt spray test how&f=false](https://books.google.co.za/books?id=8C7pXhnqje4C&pg=PA132&dq=salt+spray+test+how&hl=en&sa=X&ved=2ahUKEwi8nqWp5_jvAhVBsXEKHUCYC8YQ6AEwBXoECAMQAg#v=onepage&q=salt%20spray%20test%20how&f=false).
- [60] ASTM.B117-18, Standard Practice for Operating Salt Spray (FOG) Apparatus., 2018. <https://doi.org/10.1520/B0117-18>.
- [61] ISO 9227:2017, Corrosion tests in artificial atmospheres – Salt spray tests, 2017. <https://www.iso.org/standard/63543.html>.
- [62] MIL-DTL-5541F, CHEMICAL CONVERSION COATINGS ON ALUMINUM AND ALUMINUM ALLOYS, 2006. http://everyspec.com/MIL-SPECS/MIL-SPECS-MIL-DTL/MIL-DTL-5541F_10200/.
- [63] C. Lancea, L.A. Chicos, S.M. Zaharia, M.A. Pop, A. Semenescu, B. Florea, O.R. Chivu, Accelerated corrosion analysis of alsi10mg alloy manufactured by Selective Laser Melting (SLM), *Rev. Chim.* 69 (2018) 975–981. <https://doi.org/10.37358/rc.18.4.6240>.
- [64] S.M. Zaharia, C. Lancea, L.A. Chicos, M.A. Pop, G. Caputo, E. Serra, Mechanical properties and corrosion behaviour of 316l stainless steel honeycomb cellular cores manufactured by selective laser melting, *Trans. Famena.* 41 (2017) 11–24. <https://doi.org/10.21278/TOF.41402>.
- [65] A. Zakay, E. Aghion, Effect of Post-heat Treatment on the Corrosion Behavior of AISi10Mg Alloy Produced by Additive Manufacturing, *Jom.* 71 (2019) 1150–1157. <https://doi.org/10.1007/s11837-018-3298-x>.
- [66] A. Forn, E. Rupérez, M.T. Baile, M. Campillo, S. Menargues, I. Espinosa,

- Corrosion behaviour of A380 aluminium alloy by semi-solid rheocasting, in: AIP Conf. Proc., 2007: pp. 1161–1166. <https://doi.org/10.1063/1.2729671>.
- [67] M. Cabrini, S. Lorenzi, T. Pastore, S. Pellegrini, M. Pavese, P. Fino, E.P. Ambrosio, F. Calignano, D. Manfredi, Corrosion resistance of direct metal laser sintering AlSiMg alloy, *Surf. Interface Anal.* 48 (2016) 818–826. <https://doi.org/10.1002/sia.5981>.
- [68] M. Leary, A. Sarker, J. Tran, K. Fox, D. Downing, M. Khorasani, A. du Plessis, Surface roughness, in: I. Yadroitsev, I. Yadroitsava, A. du Plessis, E. MacDonald (Eds.), *Fundam. Laser Powder Bed Fusion Met.*, 1st ed., Elsevier, 2021: p. 500.
- [69] M.H. Nasab, D. Gastaldi, N.F. Lecis, M. Vedani, On morphological surface features of the parts printed by selective laser melting (SLM), *Addit. Manuf.* 24 (2018) 373–377. <https://doi.org/10.1016/j.addma.2018.10.011>.
- [70] G. Kerckhofs, G. Pyka, M. Moesen, J. Schrooten, M. Wevers, High-resolution micro-CT as a tool for 3D surface roughness measurement of 3D additive manufactured porous structures, *Adv. Eng. Mater.* 17 (2012) 77–83. <https://www.ndt.net/search/docs.php?id=13708>.
- [71] A. Karme, A. Kallonen, V.P. Matilainen, H. Piili, A. Salminen, Possibilities of CT Scanning as Analysis Method in Laser Additive Manufacturing, *Phys. Procedia.* 78 (2015) 347–356. <https://doi.org/10.1016/j.phpro.2015.11.049>.
- [72] Keyence, Sa (arithmetical mean height), (2020) 2. <https://www.keyence.com/ss/products/microscope/roughness/surface/parameters.jsp>.
- [73] Keyence, Sz (Maximum height), (2020) 2. <https://www.keyence.com/ss/products/microscope/roughness/surface/sz-maximum-height.jsp>.
- [74] Harrison Electropolishing, Ra vs RMS, (2014) 2. <https://www.ra.com/what-is-rheumatoid-arthritis/ra-vs-oa>.
- [75] Olympus, Surface Roughness Measurement—Parameters, (2020) 12. [https://www.olympus-ims.com/en/metrology/surface-roughness-measurement-portal/parameters/#!cms\[focus\]=areal-method](https://www.olympus-ims.com/en/metrology/surface-roughness-measurement-portal/parameters/#!cms[focus]=areal-method).
- [76] Total Materia, Corrosion of Aluminum and Its Alloys: Forms of Corrosion, (2008) 4. <https://www.totalmateria.com/page.aspx?ID=CheckArticle&site=ktn&NM=187>.
- [77] AFSA, Corrosion Resistance of Aluminium and Protective Measures where Appropriate, *Alum. Fed. South Africa.* (2011) 1–34. http://www.conways.co.za/pdf/afsa_corrosion_pocket_guide.pdf (accessed September 20, 2004).
- [78] ASTM.G46-94, Standard Guide for Examination and Evaluation of Pitting Corrosion, 2018. <https://doi.org/10.1520/G0046-94R18>.
- [79] B.K. Biswas, A. Raihan, Corrosion engineering, SlideShare. (2015) 81–82. https://www.slideshare.net/rayhan_u01/corrosion-engineering-54230652?from_action=save.

- [80] S. Gustafsson, Corrosion properties of aluminium alloys and surface treated alloys in tap water, Uppsala Universitet, 2011.
- [81] P.J. Hyde, I.M. Ritchie, The Reaction Between Aluminium Metal and Aqueous Solutions of the Nitrite Ion, *Aust. J. Chem.* 33 (1980) 169–171. <https://www.publish.csiro.au/ch/pdf/ch9800169>.
- [82] OxyPlastUK, Different types of corrosion, (2020) 2. <https://oxyplastuk.com/technical/different-types-of-corrosion/>.
- [83] A. Leon, A. Shirizly, E. Aghion, Corrosion behavior of AlSi10Mg alloy produced by additive manufacturing (AM) vs. Its counterpart gravity cast alloy, *Metals (Basel)*. 6 (2016) 9. <https://doi.org/10.3390/met6070148>.
- [84] ISO 11846:1995, Corrosion of metals and alloys — Determination of resistance to intergranular corrosion of solution heat-treatable aluminium alloys, 1995.
- [85] ASTM.G31-12a, Standard Guide for Laboratory Immersion Corrosion Testing of Metals, 2012. <https://doi.org/10.1520/NACEASTMG0031-12A>.
- [86] A. Leon, E. Aghion, Effect of surface roughness on corrosion fatigue performance of AlSi10Mg alloy produced by Selective Laser Melting (SLM), *Mater. Charact.* 131 (2017) 188–194. <https://doi.org/10.1016/j.matchar.2017.06.029>.
- [87] Cathwell, What is corrosion?, (2019) 3. <https://cathwell.com/what-is-corrosion/>.
- [88] S. Thuketana, C. Taute, H. Möller, A. du Plessis, Characterization of surface roughness and subsurface pores and their effect on corrosion in 3D-printed AlSi10Mg, *J. South. African Inst. Min. Metall.* 120 (2020) 369–376. <https://doi.org/10.17159/2411-9717/1053/2020>.
- [89] M. Rafieazad, A. Chatterjee, A.M. Nasiri, Effects of Recycled Powder on Solidification Defects , Microstructure , and Corrosion Properties of DMLS Fabricated AlSi10Mg, *JOM.* 71 (2019) 3241–3252. <https://doi.org/10.1007/s11837-019-03552-2>.
- [90] N.L. Sukiman, X. Zhou, N. Birbilis, A.E. Hughes, J.M.C. Mol, S.J. Garcia, X. Zhou, G.E. Thompson, Durability and Corrosion of Aluminium and Its Alloys: Overview, Property Space, Techniques and Developments, in: Z. Ahmad (Ed.), *Alum. Alloy. - New Trends Fabr. Appl.*, IntechOpen, 2012. <https://doi.org/10.5772/53752>.
- [91] C. Butler, Understanding your aluminium oxide surface, *Innoval Technol.* (2021) 4. <https://www.innovaltec.com/aluminium-oxide-surfaces-blog/>.
- [92] C. Leygraf, I.O. Wallinder, J. Tidblad, T. Graedel, Appendix C: the Atmospheric Corrosion Chemistry of Aluminum, in: *Atmos. Corros.*, 2nd ed., John Wiley & Sons, 2016: pp. 272–281. <https://doi.org/10.1002/9781118762134.app9>.
- [93] C. Vargel, Corrosion products, in: *Corros. Alum.*, Second, 2020: pp. 317–319. <https://doi.org/10.1016/B978-0-08-099925-8.00026-0>.
- [94] C. Berlanga-Labari, M. V. Biezma-Moraleda, P.J. Rivero, Corrosion of cast aluminum alloys: A review, *Metals (Basel)*. 10 (2020) 29. <https://doi.org/10.3390/met10101384>.

- [95] A. du Plessis, C. Broeckhoven, I. Yadroitsava, I. Yadroitsev, C.H. Hands, R. Kunju, D. Bhate, Beautiful and Functional: A Review of Biomimetic Design in Additive Manufacturing, *Addit. Manuf.* 27 (2019) 408–427. <https://doi.org/10.1016/j.addma.2019.03.033>.
- [96] M. Benedetti, A. du Plessis, R.O. Ritchie, M. Dallago, S.M.J. Razavi, F. Berto, Architected cellular materials: A review on their mechanical properties towards fatigue-tolerant design and fabrication, *Mater. Sci. Eng. R.* 144 (2021) 100606. <https://doi.org/10.1016/j.mser.2021.100606>.
- [97] W. Tao, M.C. Leu, Design of lattice structure for additive manufacturing, in: *Int. Symp. Flex. Autom. ISFA*, 2016: pp. 325–332. <https://doi.org/10.1109/ISFA.2016.7790182>.
- [98] T. Maconachie, M. Leary, J. Zhang, A. Medvedev, A. Sarker, D. Ruan, G. Lu, O. Faruque, M. Brandt, Effect of build orientation on the quasi-static and dynamic response of SLM AlSi10Mg, *Mater. Sci. Eng. A.* 788 (2020) 139445. <https://doi.org/10.1016/j.msea.2020.139445>.
- [99] C. Taute, Photos: NIN 890, (2020).
- [100] Mettler Toledo, Mettler ML Series Product Brochure, (2020) 2. <https://manualzz.com/doc/8301549/mettler-ml-series-product-brochure>.
- [101] A. du Plessis, P. Sperling, A. Beerlink, L. Tshabalala, S. Hoosain, N. Mathe, S.G. le Roux, Standard method for microCT-based additive manufacturing quality control 2: Density measurement, *MethodsX.* 5 (2018) 1117–1123. <https://doi.org/10.1016/j.mex.2018.09.006>.
- [102] C. Taute, Photos: NPY 316, (2013).
- [103] A. du Plessis, I. Yadroitsev, I. Yadroitsava, S.G. le Roux, X-Ray Microcomputed Tomography in Additive Manufacturing: A Review of the Current Technology and Applications, *3D Print. Addit. Manuf.* 5 (2018) 227–247. <https://doi.org/10.1089/3dp.2018.0060>.
- [104] A. du Plessis, S.G. le Roux, M. Tshibalanganda, Advancing X-ray micro computed tomography in Africa: Going far, together, *Sci. African.* 3 (2019) e00061. <https://doi.org/10.1016/j.sciaf.2019.e00061>.
- [105] A. du Plessis, P. Sperling, A. Beerlink, L. Tshabalala, S. Hoosain, N. Mathe, S.G. le Roux, Standard method for microCT-based additive manufacturing quality control 1: Porosity analysis, *MethodsX.* 5 (2018) 1102–1110. <https://doi.org/10.1016/j.mex.2018.09.005>.
- [106] A. du Plessis, E. Macdonald, Hot isostatic pressing in metal additive manufacturing: X-ray tomography reveals details of pore closure, *Addit. Manuf.* 34 (2020) 13. <https://doi.org/10.1016/j.addma.2020.101191>.
- [107] A. Aversa, G. Marchese, A. Saboori, E. Bassini, D. Manfredi, S. Biamino, D. Ugues, P. Fino, M. Lombardi, New aluminum alloys specifically designed for laser powder bed fusion: A review, *Materials (Basel).* 12 (2019) 19. <https://doi.org/10.3390/ma12071007>.
- [108] A. Mauduit, S. Pillot, H. Gransac, Study of the suitability of aluminum alloys for additive manufacturing by laser powder-bed fusion, *UPB Sci. Bull. Ser. B Chem.*

Mater. Sci. 79 (2017) 219–238.
https://www.researchgate.net/publication/321679030_Study_of_the_suitability_of_aluminum_alloys_for_additive_manufacturing_by_laser_powder_bed_fusion.

APPENDIX

The article “Characterization of additively manufactured AlSi10Mg cubes with different porosities” by C. Taute, H. Möller, A. du Plessis, M. Tshibalanganda, and M. Leary has been accepted by JSAIMM for publication and herewith follows the final proof.



Characterization of additively manufactured AlSi10Mg cubes with different porosities

C. Taute¹, H. Möller¹, A. du Plessis^{2,3}, M. Tshibalanganda², and M. Leary⁴

Affiliation:

¹ Department of Materials Science and Metallurgical Engineering, University of Pretoria, Pretoria 0002, South Africa.

² Research group 3DInnovation, Stellenbosch University, Stellenbosch 7602, South Africa.

³ Department of Mechanical Engineering, Nelson Mandela University, Port Elizabeth 6001, South Africa.

⁴ RMIT Centre for Additive Manufacturing, RMIT University, Melbourne 3000, Australia.

Correspondence to:

Anton du Plessis

Email:

anton2@sun.ac.za

Dates:

Received: 27 Aug. 2020

Revised: 12 Apr. 2021

Accepted: 19 Apr. 2021

Published: April 2021

How to cite:

Taute, C., Möller, H., du Plessis, A., Tshibalanganda, M., and Leary, M. 2021

Characterization of additively manufactured AlSi10Mg cubes with different porosities.

Journal of the Southern African Institute of Mining and Metallurgy, vol. 121, no. 4, pp. 143–150.

DOI ID:

<http://dx.doi.org/10.17159/2411-9717/1331/2021>

ORCID

C. Taute
<https://orcid.org/0000-0001-5771-3915>

H. Möller
<https://orcid.org/0000-0001-6075-9965>

A. du Plessis
<https://orcid.org/0000-0002-4370-8661>

M. Tshibalanganda
<https://orcid.org/0000-0003-1933-5698>

M. Leary
<https://orcid.org/0000-0002-2135-1681>

Synopsis

Additive manufacturing can be used to produce complex and custom geometries, consolidating different parts into one, which in turn reduces the required number of assemblies and allows distributed manufacturing with short lead times. Defects, such as porosity and surface roughness, associated with parts manufactured by laser powder bed fusion, can severely limit industrial application. The effect these defects have on corrosion and hence long-term structural integrity must also be taken into consideration. The aim of this paper is to report on the characterization of porosity in samples produced by laser powder bed fusion, with the differences in porosity induced by changes in the process parameters. The alloy used in this investigation is AlSi10Mg, which is widely used in the aerospace and automotive industries. The sample characteristics, obtained by X-ray tomography, are reported. The design and production of additively manufactured parts can be improved when these defects are better understood.

Keywords

additive manufacturing, L-PBF, AlSi10Mg, porosity, surface roughness, density.

Introduction

Additive manufacturing (AM) is fast becoming an important production method in the fourth industrial revolution, due to the possibilities it presents in terms of complex as well as custom geometries (DebRoy *et al.*, 2018; Dilberoglu *et al.*, 2017; Korpela *et al.*, 2020; Tofail *et al.*, 2018). This allows shorter lead times through reduction of parts required for assembly by merging parts (DebRoy *et al.*, 2018; Korpela *et al.*, 2020; Tofail *et al.*, 2018).

AlSi10Mg is popular in conventional casting methods, and substantial research effort has been applied to manufacture it successfully by AM. The addition of magnesium (Mg) gives an advantage by improving heat-treated strength due to the formation of Mg₂Si precipitates (Sercombe and Li, 2016).

There are three main pore types associated with AM, namely spherical pores, lack-of-fusion defects, and keyhole pores. Spherical pores are usually a result of gas that becomes trapped in the melt pool during the rapid solidification which is characteristic of laser powder bed fusion (L-PBF). They are generally very small in size. Lack-of-fusion pores are created when there is insufficient overlap in layers during the melting process. Insufficient overlap can mean that an area of poor bonding is created or, for extreme cases, unmelted powder is trapped in the remaining cavities. As overlaps are difficult to fully re-melt, lack-of-fusion pores are formed (Zhang, Li, and Bai, 2017). Keyhole pores occur in a vapour-filled depression well which collapses and forms large, rounded pores.

Porosity in AM, and especially L-PBF, is influenced by laser power, scanning speed, hatch spacing, layer thickness, and energy density (Tang, Pistorius, and Beuth, 2017). When scanning speed, layer thickness, and hatch spacing are kept constant, higher laser power (and higher temperature) is expected to create deeper melt pools, which cause keyhole pore formation (Bayat *et al.*, 2019; Khairallah *et al.*, 2016; Mohr *et al.*, 2020; Shrestha *et al.*, 2019; Stugelmayer, 2018; Zhao *et al.*, 2020). Lower laser powers are expected to lead to lack-of-fusion pore formation (Bayat *et al.*, 2019; Majumdar *et al.*, 2019; Mohr *et al.*, 2020; Stugelmayer, 2018). Similar to lower laser power, faster scan speed at fixed other

Characterization of additively manufactured AlSi10Mg cubes with different porosities

parameters also leads to lack of fusion and similarly, slower scan speed leads to more keyhole pore formation. This is shown schematically in Figure 1. It has also been shown that parts never truly reach full density, *i.e.* 0% porosity, even at optimal process parameters.

An optimal combination of processing parameters can minimize porosity to below 0.01%. The transition of lack-of-fusion pores is seen to be much sharper than for keyhole pores, where the transition is more gradual, as laser power is increased (du Plessis, 2019). This is illustrated in Figure 2. The optimal power for minimal porosity is seen to be lower for the lower scan speed. The alloy used in this experiment was L-PBF Ti6Al4V.

Characterizing porosity is especially important, as various studies have shown it to have a detrimental effect on the mechanical properties of AM parts. This specifically includes fatigue strength, where research revealed that pores act as crack initiators and that near-surface pores are the most critical (Zerbst *et al.*, 2019a, 2019b, 2019c). Another study of AlSi10Mg formed by AM found that areas with significant unmelted powder will undergo local cracking (Read *et al.*, 2015). Investigations into defect formation and anisotropic properties indicated that the anisotropy of both tensile ductility and fatigue properties is intensified by defects, specifically irregularly shaped porosity such as lack-of-fusion defects (Zhang, Li, and Bai, 2017; Tang and Pistorius, 2017; du Plessis, Yadroitsava, and Yadroitsev, 2020).

Non-destructive testing (NDT) is advantageous for understanding sample integrity or density without destroying the sample. Common NDT methods are the Archimedes method, gas pycnometry, ultrasonic testing, and X-ray computed tomography (CT) scanning. The Archimedes method is relatively simple, cheap, and fast. It calculates density based on the part's mass measured in air and in liquid (such as water or acetone). The density of the part is calculated according to Equation [1]:

$$\rho = \frac{m_a}{(m_a - m_L)} \times \rho_L \quad [1]$$

where ρ is the part density, ρ_L is the temperature-dependent density of the liquid, m_a is the part mass in air, and m_L is the part mass in the liquid. Acetone is recommended only in its pure form, as it is hygroscopic, otherwise de-ionized or distilled water is preferred to minimize air bubbles (Spierings, Schneider, and Eggenberger, 2011). The disadvantage of this method is that it can only determine bulk density relative to the fluid used for measurement, as well as assuming 100% material density. Porosity present in the part is then determined by comparing the Archimedes density to the reference density for the material. This also means localized pores cannot be individually evaluated (Wits *et al.*, 2016).

Gas pycnometry is a process that measures part volume by displacement of an inert gas such as helium (He). Part density is calculated by measuring the mass and volume of the parts separately. As with the Archimedes method, pycnometry is relatively easy, but the disadvantages of this method are higher equipment costs and volume detection is limited only to parts that are relatively small. This method measures skeletal density, which means that the gas penetrates all open (surface connected) pores and hence excludes them from the measurement. This means that porosity is then again determined by comparing the calculated density to the reference density (Wits *et al.*, 2016).

X-ray CT scanning can be used for both dimensional and porosity analysis, among other applications (du Plessis and le Roux, 2018; du Plessis *et al.*, 2018a). X-rays are used to form a 'shadow' image of the sample, as the rays are projected around and through the sample. The sample is rotated in front of a stationary X-ray source and the scan records these images from the various angles presented. This is followed by a software algorithm that calculates X-ray density at each point using back-projection, creating the 3D volume data (du Plessis, Yadroitsava

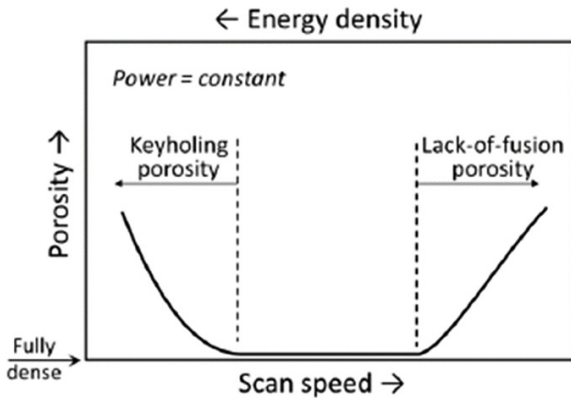


Figure 1—A typical trend of part porosity with changes in scan speed and energy density (at constant power) (Tang, Pistorius, and Beuth, 2017)

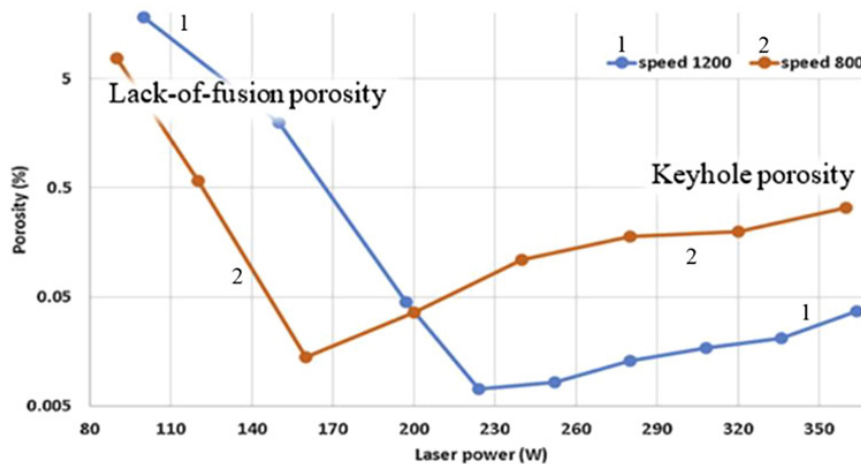


Figure 2—Porosity values as a function of laser power for two scan speeds (in mm/s) (du Plessis, 2019)

Characterization of additively manufactured AlSi10Mg cubes with different porosities

and Yadroitsev, 2020). The final result is a high-quality 3D image with a clear view of where pores are located, as well as the size range of the pores (du Plessis *et al.*, 2018a).

A comparison of NDT methods by Wits *et al.* (2016) indicated that CT scanning can measure pore areas that are smaller than the detectable size for microscopic methods, as well as predict densities more accurately than the Archimedes method. It also allows further analysis of the porosity present in the parts, such as sphericity, pore distribution, and defect volume both on the surface and inside the sample (du Plessis, Yadroitsava and Yadroitsev, 2020; Wits *et al.*, 2016).

Materials and methods

This study used AlSi10Mg samples that were printed at RMIT University in Melbourne, Australia. A total of 25 solid cubes were printed using an SLM500 Quad laser system from SLM Solutions, with dimensions $10 \times 10 \times 10 \text{ mm}^3$, and material composition as described in Maconachie *et al.* (2020). Differences in porosity content were induced by varying the printing process parameters, specifically the laser power. Five different power settings were used, namely 210, 280, 350, 420, and 490 W, with five samples printed for each power setting. The other parameters used in the printing are listed in Table I.

Different characterization methods were used as described below. X-ray CT scanning was used in two ways: once to measure the volume of the cube for a density analysis method based on volume and scale mass, and once to do a conventional CT-based porosity analysis. The system used was a GE Nanotom S and the software used for image analysis was Volume Graphics VGSTUDIO MAX 3.3.

Initial testing

Initial testing done at the University of Pretoria included measuring dimensional accuracy and mass, using a New Classic ML Mettler Toledo scale, which has a draft shield to improve accuracy. The mass in air was taken as an average of three to four individual measurements. These values were used in the subsequent density calculations.

Density measurements

Three methods were used to determine the bulk density of the samples (average density), namely Archimedes, gas pycnometry, and a CT-based density method described previously in du Plessis *et al.* (2018b).

Archimedes density measurements were done using a New Classic ML Mettler Toledo scale, accurate to four decimals, and distilled water. Four individual measurements of the samples in water were taken. The water temperature was measured to ensure accurate water density was used. Density was then calculated according to Equation [1].

Gas pycnometry was carried out using a Micromeritics AccuPyc II 1340 gas pycnometer with helium gas at a calibrated pressure of approximately 19.5 psig (134.45 kPa). Five volume measurements were obtained per sample, and the average used to calculate density.

The CT-based density calculations were based on the mass scale of the samples in air and the CT-determined volume of the cube, segmented carefully to include all pore spaces.

NanoCT scan porosity measurement

The analysis method used a procedure identical to that outlined in du Plessis *et al.* (2018c), which minimized bias in the

segmentation process. Porosity percentage values are used here, despite much more information being available. This additional data will be used in future work for further detailed analysis of pore morphologies.

Surface roughness

Surface roughnesses of the samples were obtained using optical microscopy with an Olympus DSX 510 at Wirsam Scientific. The microscope uses Olympus Stream software to plot a surface map of the sample and return surface roughness values, such as arithmetical mean height (S_a) along with a colour-scale map of the surface. Surface roughness was measured in a minimum of three separate areas ($1960 \mu\text{m} \times 1960 \mu\text{m}$ each) on both the top surface and the side surfaces, to obtain an overall representative average. The distance between each layer scanned by the microscope was $12.1 \mu\text{m}$, whereas the height range scanned differed between samples due to different surface conditions.

Results and discussion

Three density methods were used to calculate the difference in density of the samples from the different laser power sets. This is shown in Table II. An increase in laser power is shown to lower the measured bulk density of the samples, and all three methods are consistent in this trend.

In the table *A* refers to Archimedes density, *GP* is gas pycnometry density, and *CT* is the CT scan density. AlSi10Mg has a theoretical density of approximately 2.68 g/cm^3 .

From Figure 3 it can be seen that the pycnometer and CT-based densities correlate well, whereas the Archimedes density is lower. This lower value might be attributed to air bubbles attached to the surface of the sample when submerged in water, which affects the measured mass of the sample in water. The rough surface is conducive to air bubbles attaching and this was physically observed.

CT scan images of one representative sample from each laser power set are shown in Figure 4. From left to right the power settings were 210, 280, 350, 420, and 490 W. It can be seen that the first two cross-sections on the left have very small amounts of porosity, which corresponds to the lower power settings. The

Table I
Printing parameters used

Parameter	Value
Layer thickness (μm)	50
Laser velocity (mm/s)	921
Hatch spacing (μm)	190
Scan strategy	One contour scan followed by hatch tracks in zigzag pattern with 90 degree change per layer

Table II
Density of samples of each laser power set, according to three measurement methods

Laser Power (W)	Density (g/cm^3)		
	A	GP	CT
210	2.550	2.610	2.613
280	2.549	2.608	2.609
350	2.512	2.574	2.576
420	2.431	2.495	2.516
490	2.365	2.419	2.444

Characterization of additively manufactured AlSi10Mg cubes with different porosities

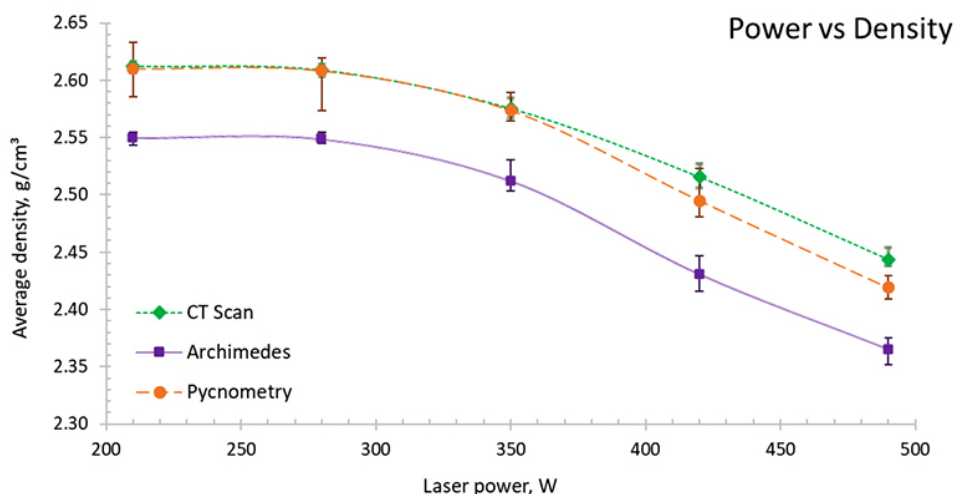


Figure 3—Density calculated with three different methods, as a function of laser power, with error bars

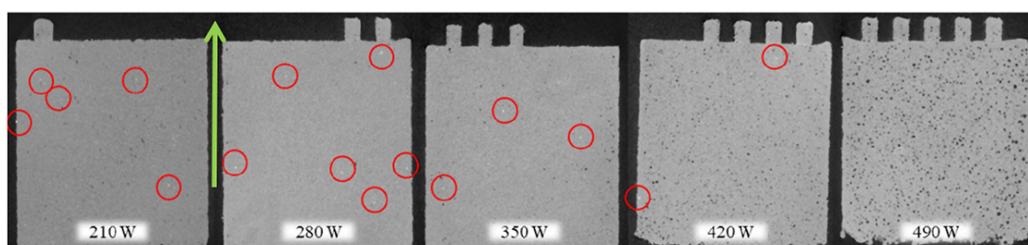


Figure 4—Representative CT cross-sectional images for each of the five different laser power settings, showing porosity (black dots) and also indicating the presence of some dense inclusions (white dots encircled in red). Arrow indicates build direction

last two cross-sections on the right are seen to contain a greater number of pores, which are larger and are rounded, which corresponds to the higher laser power and subsequently higher energy density. This large, rounded porosity at high power is attributed to keyhole mode porosity formation.

The encircled areas in Figure 4 show the presence of high-density inclusions, which could potentially be due to contamination from the powder itself, as Al alloys usually contain iron (Fe) impurities. The system used by RMIT University does not print other metal alloys, so the contamination is not from a previous build. Higher density particles from the powder itself could include iron (approx. 7.9 g/cm³), chrome (approx. 7.2 g/cm³), manganese (approx. 7.3 g/cm³), nickel (approx. 8.9 g/cm³), titanium (approx. 4.5 g/cm³), or copper (approx. 8.9 g/cm³). It is also quite possible that some of the inclusions are Al₂O₃ (3.99 g/cm³) if oxidation occurred during spattering, even in the inert gas atmosphere used for printing. The density of the inclusions is higher than that of the alloy, thus they appear brighter in the scans. It is clear that as laser power increases, the number of high-density inclusions decreases. This can be attributed to higher temperatures or larger or deeper melt pools creating more melting/remelting and homogenization of the material. The samples have pins on the upper surface to help identify them and to keep samples from the different laser power sets separated. The number of pins indicates which laser power was used, with one pin referring to 210 W, up to five pins referring to 490 W. The green vertical arrow indicates an upwards building direction.

Table III shows the total percentage of porosity, obtained from the CT results, corresponding to each laser power set, as well as

the relationship between power and porosity in a graph insert. As seen in Figure 4 and in Table III, the lowest power (E1) sample has slightly greater porosity than E2. This can be explained as due to lack of fusion porosity at 210 W and the ideal melting with lowest porosity content at 280 W compared to 210 W. The difference is statistically significant, as the 210 W laser power resulted in an average of 0.16% porosity with a variance of 0.0024 and standard deviation of 0.0495, whereas the 280 W laser power resulted in an average of 0.08% porosity with a variance of 0.0001 and standard deviation of 0.0103. As laser power increases further, the total porosity increases, due to more keyhole porosity, which is consistent with previous work (du Plessis, 2019). The error bars are calculated using the difference between the average porosity and the maximum and minimum porosity values for each laser power set.

The CT porosity analyses are shown in 3D representations in Figure 5. The porosity percentages of those specific region-of-interest (ROI) cubes are added as inserts, with the overall average of the porosity from all 10 × 10 × 10 mm³ cubes in each laser power set in parentheses.

Here it is clearly seen that the lower laser power samples have relatively little porosity, especially compared to the samples manufactured at the higher laser powers. The higher laser power samples are seen to have much higher porosity and the pores are more spherical in shape, whereas the lower power samples have less spherical, lack-of-fusion type porosity.

The presence of lack-of-fusion porosity at high values in E1, compared to E2, is not consistent with the measured density values in Figure 3 and Table II and therefore requires explanation. Despite the small average values of 0.16 and 0.08%, all density

Characterization of additively manufactured AlSi10Mg cubes with different porosities

Table III
Porosity percentage of each power set and plotted as a function of laser power

Laser power (W)	Average porosity (%voids)
210	0.16
280	0.08
350	0.56
420	2.40
490	5.59

methods showed the E1 sample to be slightly denser. The most likely explanation for this observation is that the bulk density measurements inaccurately measure the bulk when irregularly shaped pores are present on the surface. Such pores create open cavities, allowing water or gas to enter the object in surface-connected pores, and are thus excluded from the measurements. The CT-based segmentation also might select more of this type of porosity or may be inaccurate – the CT volume measurement for bulk density requires accurate calibration of the voxel size, unlike the porosity percentage value in Table III and Figure 5. The shapes of the pores are clearly more irregular at the lowest laser power and more spherical at higher power. The long, irregular pores are seen clearly in E1 *versus* the more spherical pores at higher laser powers. A scale representation is inserted to show the lengths of each side for all five cubes.

Figure 6 shows close-ups of the top surfaces of the representative samples for each laser power. These images were also obtained using VGSTUDIO MAX. As laser power is increased it can be seen that the surface roughness decreases. The first two top surfaces are seen to have a much higher surface roughness than the last two, corresponding to lower and higher laser power, respectively. The surface roughness values, S_a , are included as inserts in the figure for visual comparison. The values themselves were obtained using optical microscopy with an Olympus DSX 510, which is not dependent on track orientation relative to scanning as it is a surface area scan, which takes the R_a line profile parameter and expands it into three dimensions. The top surface was analysed as it is the final layer in the printing process, which means it is likely to be the most affected by process parameters. The bottom surface was excluded as the samples were printed on supports, leading to an irregular surface that is not representative of the parameters.

The solitary pin on the samples indicates that the samples were the first in each laser power set. The pins that range from one to five indicate the laser power setting that was used, as indicated by the powers in the inserts.

Figure 7 shows how the surface roughness in general decreases with an increase in laser power. The decrease is most likely due to wider and more overlapping melt pools, which creates a relatively smoother top surface. The error bars show that the surface roughness varied greatly in each laser power set.

The error bars are calculated using the difference between the average surface roughness, S_a , and the maximum and minimum S_a values for each laser power set.

The side surfaces were measured to obtain a general idea of the surface roughness on the sides, to see how they differ from the top surfaces. The sides of the samples showed a much smaller variation between laser power settings, averaging between 9 and 11 μm S_a across all laser powers.

This effect is shown in Figure 8. The errors bars also show how, at the highest and lowest laser powers, the surface roughness varies much more than for the middle laser powers.

Conclusions

From the results it can clearly be seen that higher laser power induces a larger volume of porosity. The higher power leads to more keyhole-type porosity, whereas the lower power samples have more lack-of-fusion type pores. The results show that high-density inclusions decrease in volume with higher laser power, due to remelting, or deeper melt pool penetration.

While higher laser power seems to decrease the surface roughness, it comes at the cost of larger volumes of porosity. If only the variation of porosity with laser power is considered, the optimal power for the given scan speed is in the range 210–280 W, with the lowest porosity at 280 W. However, when considering the measured surface roughness, the lowest porosity values for the top surface are obtained at higher powers. Therefore, depending on the requirements, a suitable combination of roughness and porosity minimization can be obtained. These results indicate some of the challenges associated with L-PBF. Typically, values for porosity $< 0.5\%$ are considered reasonable and a roughness, S_a , in the range 20–24 μm might be acceptable for some applications.

Understanding porosity formation and pore morphology associated with laser-powder bed fusion manufactured parts aids in improving parts to decrease the limiting effect these defects can have on parts in industry.

Future work will include investigation of the effect of porosity and surface conditions on corrosion and mechanical properties. Work is also ongoing on detailed 3D pore morphology evaluation using the CT data obtained in this work.

Characterization of additively manufactured AlSi10Mg cubes with different porosities

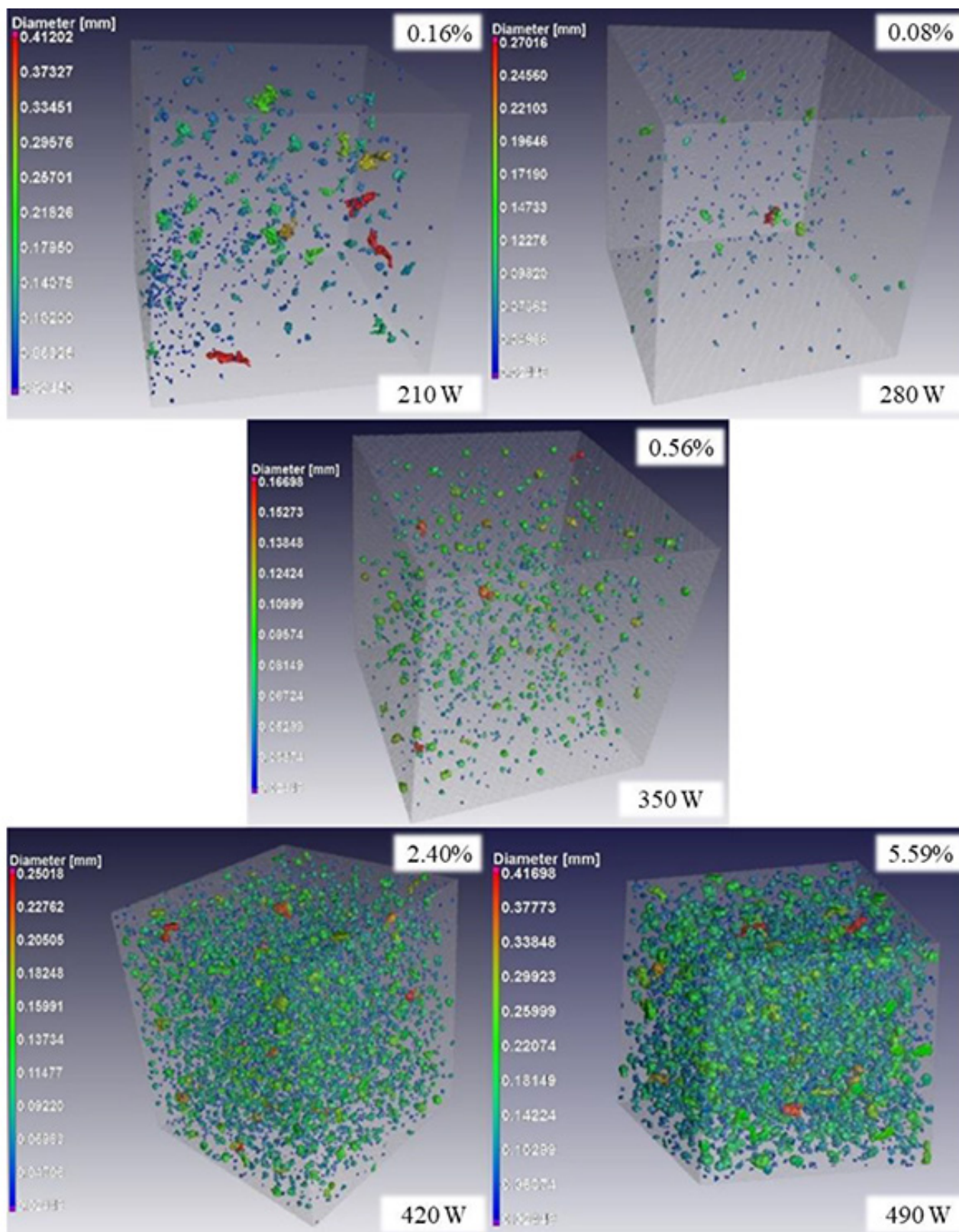


Figure 5—Porosity analyses, for a 4 × 4 × 4 mm³ region of interest, of representative samples for each of the five laser power settings, from (top) low power to (bottom) high power, with actual porosity value of ROI as inserts and overall averages in parentheses

Acknowledgments

The Light Metals Development Network (LMDN) is acknowledged for their financial support. The Collaborative Programme for Additive Manufacturing (CPAM), funded by the South African

Department of Science and Innovation, is acknowledged for additional funding.

The authors would like to thank the Stellenbosch University Research group 3DInnovation staff (Ms Carlyn Wells) for their contribution to the success of this project.

Characterization of additively manufactured AlSi10Mg cubes with different porosities

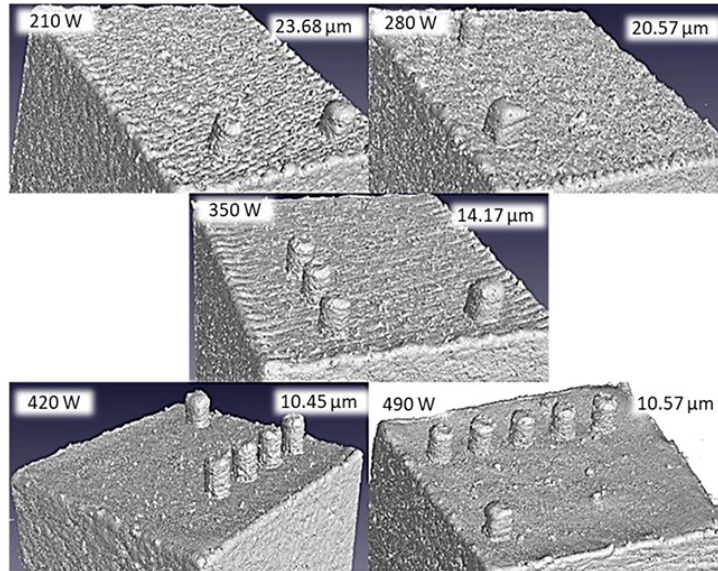


Figure 6—Close-up sections of the top surface of each representative sample for each of the five laser power settings, with S_a values as inserts

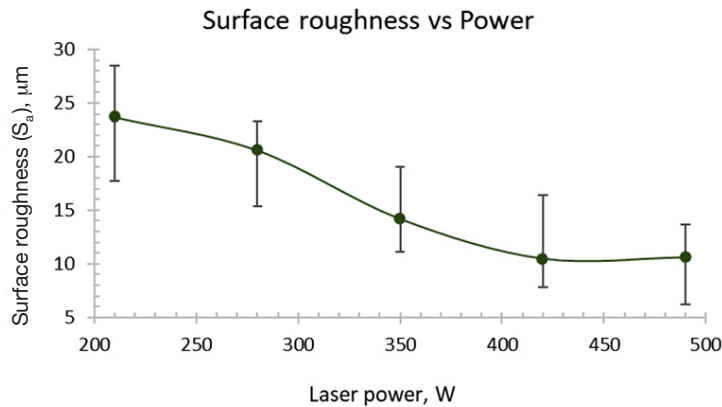


Figure 7—Plot of top surface roughness, S_a , as a function of laser power, with error bars

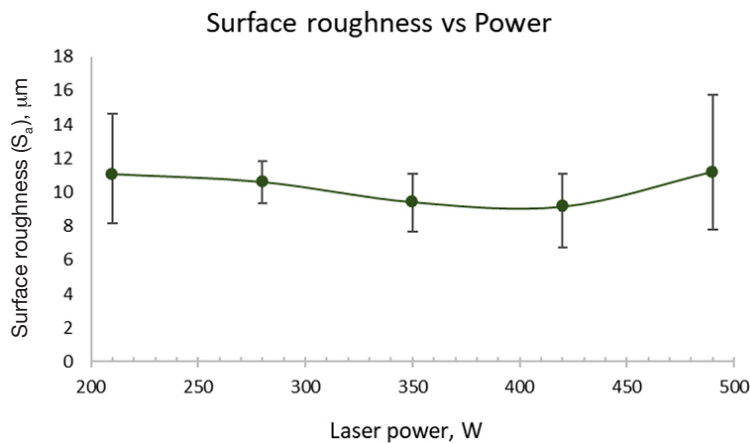


Figure 8—Plot of side surface roughness, S_a , as a function of laser power, with error bar

The authors acknowledge use of facilities in the RMIT Advanced Manufacturing Precinct

Special thanks to Mr Dewald Noeth and Ms Colleen Syrett at Wirsam Scientific for the use of their Olympus DSX 510 microscope.

Special thanks also to the staff at the University of Pretoria (Dr Robert Cromarty, Mr Sibusiso Mahlalela, Mr Dirk Odendaal, Mr Mfesane Tshazi) for all their assistance during this project.

Authors' contributions

Heinrich Möller: supervision. Anton du Plessis: supervision. Muofhe Tshibalanganda: nano-CT scanning. Martin Leary: printing and provision of samples. Carlien Taute: sample preparation, density and surface roughness measurements. The article was written by Carlien Taute and reviewed by all the authors.

Characterization of additively manufactured AlSi10Mg cubes with different porosities

References

- BAYAT, M., THANKI, A., MOHANTY, S., WITVROUW, A., YANG, S., THORBORG, J., TIEDJE, N.S., and HATTEL, J.H. 2019. Keyhole-induced porosities in Laser-based Powder Bed Fusion (L-PBF) of Ti6Al4V: High-fidelity modelling and experimental validation. *Additive Manufacturing*, vol. 30. p. 100835. <https://doi.org/10.1016/j.addma.2019.100835>
- DEBROY, T., WEI, H.L., ZUBACK, J.S., MUKHERJEE, T., ELMER, J.W., MILEWSKI, J.O., BEESE, A.M., WILSON-HEID, A., DE, A., and ZHANG, W. 2018. Additive manufacturing of metallic components – Process, structure and properties. *Progress in Materials Science*, vol. 92. pp. 112–224. <https://doi.org/10.1016/j.pmatsci.2017.10.001>
- DILBEROGLU, U., GHAREHPAPAGH, B., YAMAN, U., and DOLEN, M. 2017. The role of additive manufacturing in the era of Industry 4.0. *Procedia Manufacturing*, vol. 11. pp. 545–554. <http://dx.doi.org/10.1016/j.promfg.2017.07.148>
- DU PLESSIS, A. 2019 Effects of process parameters on porosity in laser powder bed fusion revealed by X-ray tomography. *Additive Manufacturing*, vol. 30. p. 100871. <https://doi.org/10.1016/j.addma.2019.100871>
- DU PLESSIS, A. and LE ROUX, S.G. 2018. Standardized X-ray tomography testing of additively manufactured parts: A round robin test. *Additive Manufacturing*, vol. 24. pp. 125–136. <https://doi.org/10.1016/j.addma.2018.09.014>
- DU PLESSIS, A., YADROITSEV, I., YADROITSAVA, I. and LE ROUX, S.G. 2018a. X-Ray microcomputed tomography in additive manufacturing: A review of the current technology and applications. *3D Printing and Additive Manufacturing*, vol. 5, no. 3. pp. 227–247. <https://doi.org/10.1089/3dp.2018.0060>
- DU PLESSIS, A., SPERLING, P., BEERLINK, A., TSHABALALA, L., HOOSAIN, S., MATHE, N., and LE ROUX, S.G. 2018b. Standard method for microCT-based additive manufacturing quality control 2: Density measurement. *MethodsX*, vol. 5. pp. 1117–1123. <https://doi.org/10.1016/j.mex.2018.09.006>
- DU PLESSIS, A., SPERLING, P., BEERLINK, A., TSHABALALA, L., HOOSAIN, S., MATHE, N., and LE ROUX, S.G. 2018c. Standard method for microCT-based additive manufacturing quality control 1: Porosity analysis. *MethodsX*, vol. 5. pp. 1102–1110. <https://doi.org/10.1016/j.mex.2018.09.005>
- DU PLESSIS, A., YADROITSAVA, I., and YADROITSEV, I. 2020. Effects of defects on mechanical properties in metal additive manufacturing: A review focusing on X-ray tomography insights. *Materials & Design*, vol. 187. p. 108385. <https://doi.org/10.1016/j.matdes.2019.108385>
- KHAIRALLAH, S.A., ANDERSON, A.T., RUBENCHIK, A., and KING, W.E. 2016. Laser powder-bed fusion additive manufacturing: physics of complex melt flow and formation mechanisms of pores, spatter, and denudation zones. *Acta Materialia*, vol. 108. pp. 36–45. <https://doi.org/10.1016/j.actamat.2016.02.014>
- KORPELA, M., RIIKONEN, N., PIILI, H., SALMINEN, A., and NYRHILA, O. 2020. Additive manufacturing—Past, present, and the future. *Technical, Economic and Societal Effects of Manufacturing 4.0*. Collan, M. and Michelsen, K.E. (eds.) Palgrave Macmillan, Cham, Finland. https://doi.org/10.1007/978-3-030-46103-4_2
- MACONACHIE, T., LEARY, M., ZHANG, J., MEDVEDEV, A., SARKER, A., RUAN, D., LU, G., FARUQUE, O., and BRANDT, M. 2020. Effect of build orientation on the quasi-static and dynamic response of SLM AlSi10Mg. *Materials Science and Engineering A*, vol. 788. p. 139445. <https://doi.org/10.1016/j.msea.2020.139445>
- MAJUMDAR, T., BAZIN, T., MASSAHUD CARVALHO RIBEIRO, E., FRITH, J.E., and BIRBILIS, N. 2019. Understanding the effects of PBF process parameter interplay on Ti-6Al-4V surface properties. *PLoS ONE*, vol. 14, no. 8. p. 24. <https://doi.org/10.1371/journal.pone.0221198>
- MOHR, G., ALTENBURG, S.J., ULBRICHT, A., HEINRICH, P., BAUM, D., MAIERHOFER, C., and HILGENBERG, K. 2020. In-situ defect detection in laser powder bed fusion by using thermography and optical tomography—comparison to computed tomography. *Metals*, vol. 10, no. 1. p. 19. <https://doi.org/10.3390/met10010103>
- READ, N., WANG, W., ESSA, K. and ATTALLAH, M.M. 2015. Selective laser melting of AlSi10Mg alloy: Process optimisation and mechanical properties development. *Materials & Design*, vol. 65. pp. 417–424. <http://dx.doi.org/10.1016/j.matdes.2014.09.044>
- SERCOMBE, T.B. and LI, X. 2016. Selective laser melting of aluminium and aluminium metal matrix composites: Review. *Materials Technology*, vol. 31. pp. 77–85. <https://doi.org/10.1179/1753555715Y.0000000078>
- SHRESTHA, S., STARR, T., and CHOU, K. 2019. A study of keyhole porosity in selective laser melting: Single-track scanning with micro-CT analysis. *Journal of Manufacturing Science and Engineering*, vol. 141, no. 7. p. 11. <https://doi.org/10.1115/1.4043622>
- SPIERINGS, A.B., SCHNEIDER, M., and EGGENBERGER, R. 2011. Comparison of density measurement techniques for additive manufactured metallic parts. *Rapid Prototyping Journal*, vol. 17, no. 5. pp. 380–386. <https://doi.org/10.1108/13552541111156504>
- STUGELMAYER, E. 2018. Characterization of process induced defects in laser powder bed fusion processed AlSi10Mg alloy. Master's thesis, Montana Technological University. https://digitalcommons.mtech.edu/grad_rschn/157
- TANG, M. and PISTORIUS, P.C. 2017. Anisotropic mechanical behavior of AlSi10Mg Parts produced by selective laser melting. *JOM*, vol. 69. pp. 516–522. <https://doi.org/10.1007/s11837-016-2230-5>
- TANG, M., PISTORIUS, P.C., and BEUTH, J.L. 2017. Prediction of lack-of-fusion porosity for powder bed fusion. *Additive Manufacturing*, vol. 14. pp. 39–48. <https://doi.org/10.1016/j.addma.2016.12.001>
- TOFAIL, S.A.M., KOUMOULOS, E.P., BANDYOPADHYAY, A., BOSE, S., O'DONOGHUE, L., and CHARITIDIS, C. 2018. Additive manufacturing: Scientific and technological challenges, market uptake and opportunities. *Materials Today*, vol. 21, no. 1. pp. 22–37. <https://doi.org/10.1016/j.mattod.2017.07.001>
- WITS, W.W., CARMIGNATO, S., ZANINI, F., and VANEKER, T.H.J. 2016. Porosity testing methods for the quality assessment of selective laser melted parts. *Manufacturing Technologies*, vol. 65. pp. 201–204. <http://dx.doi.org/10.1016/j.cirp.2016.04.054>
- ZERBST, U., MADIA, M., KLINGER, C., BETTGE, D., and MURAKAMI, Y. 2019a. Defects as a root cause of fatigue failure of metallic components. I: Basic aspects. *Engineering Failure Analysis*, vol. 97. pp. 777–792. <https://doi.org/10.1016/j.engfailanal.2019.01.055>
- ZERBST, U., MADIA, M., KLINGER, C., BETTGE, D., and MURAKAMI, Y. 2019b Defects as a root cause of fatigue failure of metallic components. II: Non-metallic inclusions. *Engineering Failure Analysis*, vol. 98. pp. 1–12. <https://doi.org/10.1016/j.engfailanal.2019.01.054>
- ZERBST, U., MADIA, M., KLINGER, C., BETTGE, D., and MURAKAMI, Y. 2019c. Defects as a root cause of fatigue failure of metallic components. III: Cavities, dents, corrosion pits, scratches. *Engineering Failure Analysis*, vol. 97. pp. 759–776. <https://doi.org/10.1016/j.engfailanal.2019.01.034>
- ZHANG, B., LI, Y., and BAI, Q. 2017. Defect formation mechanisms in selective laser melting: A review. *Chinese Journal of Mechanical Engineering*, vol. 30. pp. 515–527. <https://doi.org/10.1007/s10033-017-0121-5>
- ZHAO, C., PARAB, N. D., LI, X., FEZZAA, K., TAN, W., ROLLETT, A. D. and SUN, T. 2020. Critical instability at moving keyhole tip generates porosity in laser melting. *Science*, vol. 370, no. 6520, pp. 1080–1086. <https://doi.org/10.1126/science.abd1587> ◆